SURFACE CHEMISTRY AND WORK FUNCTION OF IRRADIATED AND NANOSCALE THIN FILMS COVERED INDIUM TIN OXIDES

Hui Che

Dissertation Prepared for the Degree of

DOCTOR OF PHILOSOPHY

UNIVERSITY OF NORTH TEXAS

May 2018

APPROVED:

Mohamed El Bouanani, Committee Chair
Samir Aouadi, Committee Member
Jincheng Du, Committee Member
Sundeep Mukherjee, Committee Member
Bibhudutta Rout, Committee Member
Andrey Voevodin, Chair of the Department of Materials Science and Engineering
Costas Tsatsoulis, Dean of the College of Engineering
Victor Prybutok, Dean of the Toulouse Graduate School

Che, Hui. *Surface Chemistry and Work Function of Irradiated and Nanoscale Thin Films Covered Indium Tin Oxides*. Doctor of Philosophy (Materials Science and Engineering), May 2018, 136 pp., 41 figures, 117 numbered references.

In this study, we used UV-ozone Ar sputtering, X-ray photoelectron and ultra-violet photoelectron spectroscopies and sputtering based depositions of RuO_2 and Se nano-layers on indium tin oxides (ITOs). We elucidated the effect of Ar sputtering on the composition and chemistry of Sn rich ITO surface. We demonstrated that while a combination of UV-ozone radiation and Ar sputtering removes most of the hydrocarbons responsible for degrading the work function of ITO, it also removes significant amount of the segregated SN at the ITO surface that's responsible for its reasonable work function of 4.7eV. We also demonstrated for the first time that sputtering cleaning ITO surface leads to the reduction of the charge state of Sn from $Sn4^{+}$ to $Sn2^{+}$ that adds to the degradation of the work function. For the nano-layers coverage of ITO studies, we evaluated both RuO_2 and Se. For RuO_2 coated ITO, XPS showed the formation of a Ru-Sn-O ternary oxide. The RuO_2 nano-layer reduced the oxidation state of Sn in the Sn-rich surface of ITO from +4 to +2. The best work function obtained for this system is 4.98eV, raising the effective work function of ITO by more than 0.5 eV. For the Se coated ITO studies, a systematic study of the dependence of the effective work function on the thickness of Se overage and its chemistry at the Se/ITO interface was undertaken. XPS showed that Se reacts with Sn at the Sn-rich surface of ITO determined the presence of both negative and positive oxidation state of Se at the Se/ITO interface. The Se also reduced the oxidation state of Sn from $Sn4^{+}$ to $Sn2^{+}$ in the Sn-rich ITO surface. The highest effective work function obtained for this system is 5.06eV. A combination of RuO_2/Se nanoscale coating of optimally cleaned ITO would be a good alternative for device applications that would provide work function tuning in addition

to their potential ability to act as interface stabilizers and a barrier to reaction and inter-diffusion at ITO/active layers interfaces responsible for long term stability of devices and especially organic solar cells and organic light emitting diodes.

Copyright 2018

By

Hui Che

TABLE OF CONTENTS

Page

LIST OF FIGURES v

CHAPTER 1. INTRODUCTION 1

1.1 Motivation and Objective 1

1.2 Organization of the Dissertation 3

CHAPTER 2. LITERATURE REVIEW 5

2.1 Crystal Structure of ITO with Low Tin Concentration 6

2.2 Formation of Neutral Defect Cluster and Tin-Rich Surface in ITO with High Tin Concentration 8

2.3 Work Function Change with Different Surface Treatments 11

CHAPTER 3. EXPERIMENTAL TECHNIQUES 16

3.1 Surface Treatments 16

3.1.1 UV-Ozone Radiation 16

3.1.2 Sputtering 17

3.2 Deposition Methods 19

3.2.1 Ion-Beam Deposition 19

3.2.2 Magnetron Sputtering 19

3.3 Characterization Techniques 22

3.3.1 X-Ray Photoelectron Spectroscopy (XPS) 22

3.3.2 Ultraviolet Photoelectron Spectroscopy (UPS) 30

CHAPTER 4. EFFECTS OF ARGON SPUTTERING AND UV-OZONE RADIATION ON THE PHYSICO-CHEMICAL SURFACE PROPERTIES OF ITO 35

4.1 Introduction 35

4.2 Experimental 37

4.3 Results and Discussion 38

4.3.1 Removal of Surface Carbon-Based Contaminants 38

4.3.2 Sn-Rich Surface 42

4.3.3 Comparison of Core-Level XPS Spectra between As-Received and Ar^+ Sputter Cleaned ITO Surface 43

4.3.4 Reduction of Surface Sn^{4+} and Components of Sn3d Core-Level Peak 48

4.3.5 Composition of O1s Peak 55
4.3.6 UPS Measurement of Work Function 58
4.4 Conclusion 61

CHAPTER 5. SURFACE CHEMISTRY AND WORK FUNCTION CHANGES OF RUO_2/ITO STUDIED BY XPS AND UPS 62
5.1 Introduction 62
5.2 Experimental 64
5.3 Result and Discussion 66
5.3.1 Surface Carbon-Based Contaminant Removal by UV-Ozone Radiation and Ar^+ Sputtering 66
5.3.2 Energy Calibration 70
5.3.3 Core-Level Peak Shift Caused by RuO_2 Deposition 72
5.3.4 Peak Shift Caused by Ar^+ Sputtering 76
5.3.5 Effect of Ar^+ Sputtering on Surface Sn Ions 78
5.3.6 Reduction of Ru^{4+} by Ar^+ Sputtering 84
5.3.7 Evolution of Work Function 94
5.4 Conclusion 98

CHAPTER 6. TUNING WORK FUNCTION OF INDIUM TIN OXIDE BY SE DEPOSITION AND XPS STUDY ON SE/ITO INTERFACE 100
6.1 Introduction 100
6.2 Experimental 101
6.3 Result and Discussion 102
6.3.1 Work Function Tuning by Se Ultra-Thin Film 102
6.3.2 Reduction of Sn^{4+} at Se/ITO Interface 105
6.3.3 Chemical Bonding of Se at Se/ITO Interface 115
6.4 Conclusion 124

CHAPTER 7. CONCLUSION OF DISSERTATION 125

REFERENCES 127

LIST OF FIGURES

Page

Figure 2.1 First coordination of Indium sites in In_2O_3 crystal structure. 7

Figure 3.1 Schematic layout of basic DC sputtering apparatus. 21

Figure 3.2 Energy level diagram. 24

Figure 3.3 Schematic concentric hemispherical analyzer. 25

Figure 4.1 C1s core-level spectra of the ITO with different surface treatments........................... 40

Figure 4.2 C1s core-level spectra of ITO with heavy Ar^+ sputtering. 41

Figure 4.3 Normalized In3d, Sn3d, and O1s spectra collected with different TOAs. 42

Figure 4.4 $In3d_{5/2}$, $Sn3d_{5/2}$, O1s, and C1s spectra of UV-ozone treated ITO with and without Ar^+ sputtering... 44

Figure 4.5 Peak fitting on $In3d_{5/2}$ peaks. 47

Figure 4.6 Valence band XPS spectra of ITO with different surface treatments. 49

Figure 4.7 UPS spectra of ITO with different surface treatments. 50

Figure 4.8 Peak fitting on Sn3d spectra. 52

Figure 4.9 (a) intensity ratio of Sn^{2+}/Sn^{4+} versus TOAs. (b) intensity ratio of Sn^{2+}/Sn^{4+} versus sputter time... 54

Figure 4.10 Peak fitting on O1s peaks. 57

Figure 4.11 Work function of ITO with different surface treatments.. 58

Figure 5.1 Ru3d spectra of the 1-minute deposited RuO_2/ITO sample treated by UV-ozone radiation for different exposure time. 67

Figure 5.2 The comparison of Ru3d of 1-minute deposited RuO_2/ITO before and after Ar^+ sputtering... 69

Figure 5.3 Valence band XPS spectra of RuO_2/ITO samples treated by various sputter time. Samples are pre-treated by 30 minutes UV-ozone radiation. 71

Figure 5.4 Core-level XPS spectra of ITO, 1-minute deposited RuO_2/ITO, and 2-minute deposited RuO_2/ITO, three samples received 30 minutes UV-ozone radiation........................... 73

Figure 5.5 Peak fitting on $In3d_{5/2}$ and $Sn3d_{5/2}$ peaks 74

Figure 5.6 Core-level spectra of 1-minute deposited RuO_2/ITO received various sputter time... 77

Figure 5.7 Core-level spectra of 2-minute deposited RuO_2/ITO received various sputter time... 77

Figure 5.8 Ratio of $Sn3d_{3/2}$ to $In3d_{5/2}$ changes as a function of increased sputter time. 80

Figure 5.9 Intensity ratio of Sn^{2+}/Sn^{4+} changes as a function of sputter time............................. 82

Figure 5.10 Ru3d and O1s core-level spectra of the RuO_2/SiO_2 sample with various surface treatments. 85

Figure 5.11 Peak fitting on Ru3d of RuO_2/SiO_2. 90

Figure 5.12 Peak fitting results of Ru3d of the RuO_2/ITO samples with various sputter time. ... 92

Figure 5.13 UPS spectra of the 1-minute deposited and 2-minute deposited RuO2/ITO samples, the two samples are pre-treated by 30 minutes UV-ozone radiation. 95

Figure 5.14 Work function of ITO, 1-min deposited and 2-min deposited RuO_2/ITO. All samples are pre-treated by 30 minutes UV-ozone radiation. 95

Figure 6.1 UPS spectra of the ITO and the Se/ITO samples 103

Figure 6.2 Work function versus intensity ratio of Se/In... 105

Figure 6.3 Comparison of core-level spectra of the ITO and the sample 1. 108

Figure 6.4 Peak fitting on $In3d_{5/2}$ peaks. 109

Figure 6.5 Peak fitting on $Sn3d_{5/2}$ peaks. 110

Figure 6.6 Peak fitting on O1s peaks. 111

Figure 6.7 Comparison of core-level peaks of the Se/ITO samples. 113

Figure 6.8 (a) Binding energy of screened $In3d_{5/2}$ peaks versus intensity ratio of Se/In. (b) intensity ratio of Sn^{2+}/Sn^{4+} versus intensity ratio of Se/In. (c) intensity ratio of the Sn-rich surface plus carbonate contaminant to the stoichiometric ITO lattice versus the peak area ratio of Se/In. 114

Figure 6.9 Se3d spectra of the Se/ITO samples. 116

Figure 6.10 Comparison of Se3d spectra: (a) comparison between elemental Se and the sample 8; (b) comparison between the spectra collected at different TOAs. 117

Figure 6.11 Se3d spectra of the Se/Si and Se/SiOx samples. 120

Figure 6.12 Peak fitting results of Se3d spectra of the Se/ITO samples................................... 121

CHAPTER 1

INTRODUCTION

1.1 Motivation and Objective

Indium tin oxide (ITO), among a long list of transparent conductive oxides (TCOs), is the most widely used in solar cells, organic and inorganic light emitting diodes and other electronic and optoelectronic devices. ITO dominates the above applications due to its high electrical conductivity, high optical transmittance, and acceptable work function. Although ITO has a work function of about 4.7 eV, it is significantly affected by surface contaminants, resulting in a much reduced effective work function that is not optimal for the fabricated devices. These contaminants are dominated by adsorbed hydrocarbons and hydroxyl compounds. Prior to the fabrication processes of ITO based devices, the surface contaminants are usually removed by one of the many surface cleaning treatments such as UV-ozone radiation, plasmas, and sputtering. Depending on the selected surface treatment, the resulting work function is not always enhanced when the surface contaminants are removed due to the induced modification of surface chemistry of ITO. The resultant surface composition and chemistry of ITO is complex and treatment specific and leads to either an increase or decrease in its work function.

In addition to the above, even a super surface clean ITO with a work function of about 4.7 eV is not high enough for optimal operation of many device applications. Any of the current surface cleaning treatments used to remove surface contaminants only partially eliminate the influence of surface contaminant on the work function of ITO. They cannot enhance the work function beyond the work function of contaminant free ITO. Additional work function tuning steps such as depositing a monolayer to few monolayers of high work function elements or compounds is a damage-free way to increase and optimize the work function of ITO. A lot of

research and devices optimization work has been performed in the above areas of surface cleaning treatments and work function tuning. For example, in the case of surface cleaning via argon (or other ions) radiation, there is still a lack of definitive and complete understanding of the induced surface composition and chemistry of the treated ITO. The interplay between those induced surface changes and its effects on the work function is also missing. Most of the published work is dedicated to final products and devices in terms of better devices efficiencies.

For the cases of optimizing the work function of ITO via nanoscale surface coating, extensive work has been done in this area with good success. Few monolayers of molybdenum oxide on ITO is currently used with excellent results. One needs to emphasize that for device applications, the requirements for TCOs (such as ITO) to be used as electrodes are not simply high work function, high conductivity, and high transparency. The interface between ITO and the other organic/inorganic materials used in devices fabrication must exhibit long term chemical stability with abrupt interface. It's well known that, at least, some organic semiconductors either diffuse into or react with oxygen in ITO, which leads to device degradation while in operation. Although molybdenum oxide nano coating of ITO allows optimal work function, it's not confirmed yet that it's chemically stable interface with all potential semiconductor materials. It's well established that ITO has a Sn-rich surface due to the segregation of Sn. The removal of contaminants via radiation, plasmas and etching treatments also leads to significant changes in the surface chemistry of ITO. Nonetheless, the influence of the Sn-rich surface and specifically its composition and surface chemistry effects on the work function of ITO has not been investigated or reported in the literature. Thorough understanding of the reactivity of work function enhancing nanoscale coatings and their ability to maintain sharp ITO/semiconductor interfaces (diffusion barrier) is also lacking. For optimal properties and long term stability of

ITO based devices, it's of paramount importance to fully understand the interaction between the Sn-rich surface of ITO, the radiation induced surface chemistry changes and subsequent optimal nanoscale deposited films.

The objective of this research in this dissertation is to:

1. Thoroughly study and contribute to a definitive understanding of the interplay between argon sputtering as a surface cleaning method for contaminants removal from ITO surface and the induced surface composition and chemistry of the treated ITO, and correlation between its induced surface composition and chemistry and work function of ITO.

2. Study ruthenium oxide as a nanoscale thin film coating of ITO with the objective of simultaneously enhancing the work function of ITO and acting as a chemically stabilizer and diffusion barrier between ITO and other potential semiconductors used for device applications.

3. Study selenium as a nanoscale film coating of ITO for enhanced work function of ITO and potentially an interface stabilizer between ITO and other semiconductors. Se nanoscale film coating would be a good solution due to its high stability and high work function.

1.2 Organization of the Dissertation

This dissertation consists of seven chapters.

Chapter 1 depicts the motivation, objective and organization of this dissertation.

In Chapter 2, a brief description and literature review of ITO is given. It includes crystal structure, doping level, conductivity, and work function of ITO.

Chapter 3 describes thin films preparation and characterization methods.

In Chapter 4, the surface chemistry of the native Sn-rich surface of ITO is studied. The correlation between low energy Ar^+ sputter cleaning and induced changes in the chemical

properties of the Sn-rich surface of ITO is elucidated. This study shows a direct correlation between the relative surface Sn content and its chemical charge states of the Sn-rich surface and the work function of ITO.

In Chapter 5, the study of nanoscale RuO_2 ultra-thin film coating of ITO is presented. In Chapter 6, the study of the dependence of the thickness of Se coating on the work function of ITO is presented. Both RuO_2 and Se have higher work function than ITO and are demonstrated to raise the work function of ITO. The chemical bond at the RuO_2/ITO and Se/ITO interfaces are investigated. The reactivities between the Sn-rich surface of ITO and the deposited films, which are nanoscale deposited RuO_2 and Se ultra-thin films, are elucidated. Their effects on the modified/enhanced work function are demonstrated.

Chapter 7 gives the conclusion of this dissertation.

CHAPTER 2

LITERATURE REVIEW

Indium tin oxide, also named tin doped indium oxide, is one of the most important transparent conductive oxide (TCO). ITO thin films can be easily prepared by various techniques, such as sputtering deposition, thermal evaporation, sol-gel deposition, pulsed laser deposition (PLD), chemical vapor deposition (CVD), and spray pyrolysis [1]. The ITO thin films exhibit high electrical conductivity and high optical transparency in the visible range [2][3][4][5]. They are widely utilized in such optical and electronic applications as, for example, flat-panel displays, organic photovoltaics, and solar cells [6][7]. In multilayer-structured thin film solar cells, ITO is one of the most applied front contact materials. Besides the high optical transmittance, the ITO thin film also has high electrical conductivity.

Indium oxide, the host material of ITO, is an n-type semiconductor with finite conductivity. The charge carrier concentration can reach 1×10^{19} cm^{-3} [1]. When the indium oxide is doped by tin to form ITO, the charge carrier concentration can increase up to 1×10^{21} cm^{-3} [1]. The increased carrier concentration can lift the Fermi level and lead to reduced work function. As a result, the work function of ITO will be lower than the work function of In_2O_3 [8]. The high electrical conductivity and work function are two essential factors of ITO which make ITO popular in optoelectronic devices. Thus, there is a dilemma when ITO is prepared: either keeping high electrical conductivity or keeping high work function. As mentioned before, ITO thin films can be prepared via different deposition methods. ITOs prepared at different conditions perform different electrical conductivities and work functions. This is attributed to the complex crystal structure and surface properties of ITO. The formation of neutral defect clusters at different tin

doping concentrations is described in section 2.1 and 2.2. The work function change of ITO as a function of surface treatments is introduced in section 2.3.

2.1 Crystal Structure of ITO with Low Tin Concentration

ITO is one of ternary compound semiconductors. The host material is indium oxide (In_2O_3) and is an n-type semiconductor. The major carrier provider in in In_2O_3 is oxygen vacancies [9]. When tin ions replace indium ions to form ITO, Sn^{4+} becomes the major carrier provider. ITO is designed to exhibit as high as possible electrical conductivity that can be easily achieved by increasing Sn doping concentration. The atomic concentration of Sn in ITO is usually in the 5-10% range, which is beyond the doping levels in conventional doped semiconductors [10]. However, the electrical conductivity of ITO does not always increase with increased Sn concentration. The mechanism of the conductivity in ITO is complex due to its complex crystal structure.

The host material In_2O_3 is cubic bixbyite structure, which belongs to $Ia\overline{3}$ space group [11]. The lattice parameter of the unit cell of ITO is 10.117Å [10]. There are total 80 atoms in one unit cell. This structure is similar to the fluorite structure, but one quart of anions are absent. Indium ions are 6-coordinated and occupy distorted octahedral interstitial sites. The octahedral interstitial sites are not equivalent. They are classified into two groups: b-sites and d-sites [11][12][13]. Figure 2.1 displays the first coordination of indium sites schematically. Oxygen ions (red balls) form cubes. The distortion, caused by absent anions (blue balls), is not reflected in the sketch. In b-site, oxygen vacancies are located along the body diagonal of the cube. Indium ion bonds with 6 oxygen ions with equivalent bond-length. The value of the bond-length is 2.18 Å. In d-site, two oxygen vacancies are located along the face diagonal of the cube. The

six In-O bonds have nonequivalent bond-length, which are 2 of 2.13, 2.19, and 2.23Å, respectively.

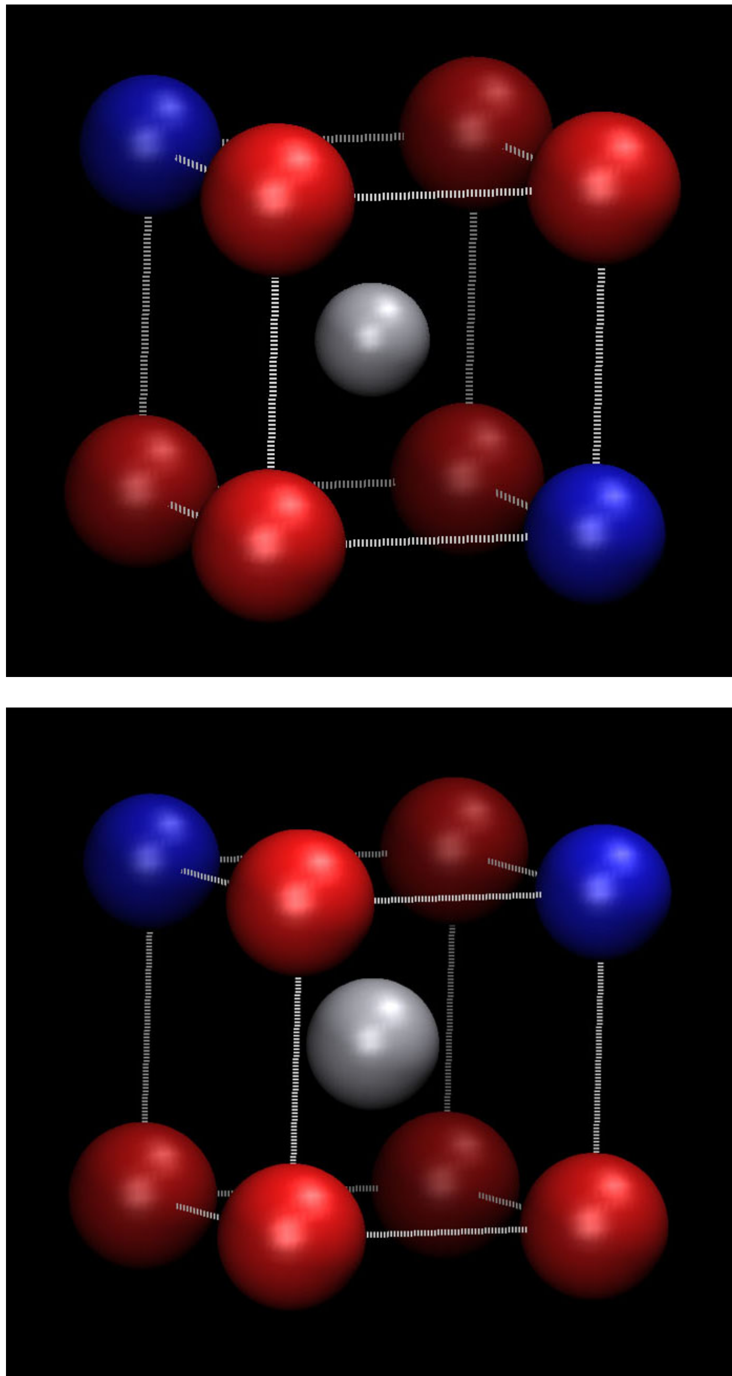

Figure 2.1. First coordination of indium sites in In_2O_3 crystal structure.

A defect model for depicting the structure of ITO was first developed by G. Frank and H. Köstlin [2]. Tin ions exist in ITO as Sn^{4+} ions, which was established by Mössbauer

experiments [14][15][16]. Sn^{4+} ions provide donor electrons to make ITO an n-type semiconductor. To compensate the charge of $Sn_{In}^{\cdot}$, interstitial oxygen (O_i) ions are introduced into the structure. The interstitial oxygen ions fill the original oxygen vacancies in the host material In_2O_3. One interstitial oxygen ion bonds with two Sn^{4+} to form a neutral cluster $(2Sn_{In} \cdot O_i)^x$. At a low level of Sn^{4+} concentration, the bonds between interstitial oxygen and Sn^{4+} ions are weak [2][12][13][17]. At a high level of Sn^{4+} concentration, the situation becomes complicated.

When ITO with a low Sn^{4+} concentration is placed in the reduction condition, the Sn-O_i bonds are easy to break. This disassociation can be described by the following equation [17]:

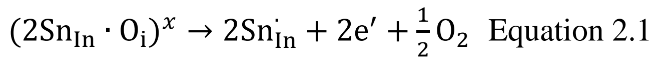

$$(2Sn_{In} \cdot O_i)^x \rightarrow 2Sn_{In}^{\cdot} + 2e' + \frac{1}{2}O_2 \quad \text{Equation 2.1}$$

Under the reduction condition, the balance shifts to the right-hand side of the Equation 2.1. The donor electrons are freed. It gives rise to increased carrier density. In G. Frank and H. Köstlin's report, the carrier density of ITO at a reduction condition can reach 1.5×10^{21} cm^{-3} when the Sn concentration is in a range of 6~9% [2]. However, the carrier mobility decreases with increased carrier densities. The magnitude of the decrease is $\mu \sim N^{-1/3}$. The electrical conductivity of ITO still increases with increased tin doping level because the increased carrier density can compensate the effect from the reduced carrier mobility. As a result, the low tin-doped ITO at reduction conditions obtains high electrical conductivity. This is the reason why commercial ITOs are usually fabricated at reduction conditions.

2.2 Formation of Neutral Defect Cluster and Tin-Rich Surface in ITO with High Tin Concentration

A phase equilibrium of In_2O_3-SnO_2 pseudo-binary system is given by H. Enoki et al. [18]. They showed that the temperature-independent solubility of SnO_2 in In_2O_3 is about 12.4 to

15.0 mol%. In literature, the reported tin doping concentration of ITO samples can far exceed the 15.0 mol% [10][12]. In these reports, the carrier densities of highly tin-doped indium oxides decreased with increased tin doping concentration. The authors correlated this phenomenon with the formation of neutral cluster $(2Sn_{In} \cdot O_i)^x$ in ITOs. When the tin doping concentration is high and above the solubility limit of SnO_2 in In_2O_3, the neutral clusters will form to decrease the carrier density of ITO. The reported solubility limits of SnO_2 for ITOs are not a constant. The solubility limit is from 6 to 9 at.% [2][10][12].

In literature, ITOs are usually described by low and high tin concentrations. Generally speaking, the "low" indicates that the concentration of tin is under the solubility limit, and the "high" means that above the limit. For ITO with high Sn^{4+} concentration, G. Frank and H. Köstlin built a model to explain the change of carrier density with tin doping concentration [2]. There are two types of neutral defect clusters. One is the reducible cluster and the other is the nonreducible cluster. The reducible cluster is the cluster in the Equation 2.1. At reduction conditions, the reducible clusters can be reduced to release the donor electrons. These reducible clusters are in the dominant place in the ITO with low tin concentration. When the tin doping concentration is high, the increased tin concentration give rise to the formation of nonreducible cluster. The bonds between Sn^{4+} and interstitial oxygen ions become so intense that the non-reducible cluster cannot be reduced at reduction conditions. In the ITO crystal lattice, the first coordination of In^{3+} is 6. Sn^{4+} ions replace In^{3+} and occupy indium sites. In the nonreducible cluster, interstitial oxygen ions occupy the original oxygen vacancies. The first coordination of Sn^{4+} turns to 8. The structure of the non-reducible cluster is fluorite-type like Sn_2O_4. However, this structure is questioned by some authors[10][12][13]. More models are developed based on G. Frank and H. Köstlin's model. O. Warschkow etc. developed a model [17]. They concluded

that the basic type of the neutral defect cluster is $(2\mathrm{Sn_{In}} \cdot \mathrm{O_i})^{\mathrm{x}}$. One interstitial oxygen ion bonds with two Sn^{4+} ions. The ratio of Sn^{4+}/O^{2-} is 2:1. When two or more these 2:1 defect clusters are located close enough, the interstitial oxygen may bond with one more Sn^{4+} ion to form an aggregate cluster. The ratio of Sn^{4+}/O^{2-} is 3:1. The 2:1 defect cluster is reducible, and the 3:1 defect cluster is non-reducible. In the ITO with low tin concentration, the basic neutral defect clusters randomly disperse. The probability for two closely located clusters is low. With increase of tin concentration, the number of the clusters increases. The probability of aggregation also increases. Reducible clusters will aggregate and form the nonreducible cluster.

A different model of the ITO with high tin doping concentration is given by N. Nadaud's group [12]. They pointed out that the non-reducible neutral cluster is the $In_4Sn_3O_{12}$ phase. The solubility limit of tin in the host material In_2O_3 in their experiment is 6%. Tin-rich phase can be found either along grain boundaries or on the surface of ITO if the tin concentration is above 6%. They combined the data of EXAFS and Mössbauer experiments to suggest that the tin-rich content is the $In_4Sn_3O_{12}$ phase. In the $In_4Sn_3O_{12}$ phase, Sn^{4+} ions are surrounded by oxygen ions so that tin ions are electrically inactive. Due to the formation of the low conductive $In_4Sn_3O_{12}$ phase, the conductivity of ITO decreases when tin concertation exceeds the solubility in ITO. The existence of $In_4Sn_3O_{12}$ is argued [19]. So far, no solid evidence to prove that the tin-rich phase along the grain boundaries and on the surface of ITO is $In_4Sn_3O_{12}$. In G. Frank's experiment, crystallized SnO_2 was found in the ITO sample with high tin concentration after 2 weeks annealing at 950˚C [20]. The tin-rich phase is possible SnO_2-like.

Although the composition of the tin-rich phase is not confirmed, there is one thing can be sure: the oxidation state of tin in the Sn-rich phase is mainly +4 [2][12][17][21]. The Sn-rich

phase on the surface is a common nature of ITO and frequently mentioned in literature [21][22][23][24].

2.3 Work Function Change with Different Surface Treatments

The work function of ITO was first time measured via UPS by Y. Park and his co-workers in 1996 [25]. The work function equals the difference of the photo energy of the ultraviolet source and the width of the UPS spectrum. The calculated work function is reliable and accurate due to the well-defined and accurate photo energy of the UV source. The He-I irradiation is used as the UV source for the work function measurement. The photo energy of the He-I irradiation is only 21.22 eV. Thus, the UPS measurement is highly surface sensitive and only can probe the surface of ITO. The measured work function is the surface work function of ITO. In the applications of ITO, the surface of ITO is the only part in contact with other materials. The surface work function of ITO determines the performances of the devices. In this case, the UPS is an ideal tool to investigate the surface work function of ITO and any modifications to its surface. The work function of ITO with the contaminant-free surface is 4.8 eV [25][26].

The work function correlates with the Fermi level and vacuum level. The work function of ITO can be tuned via two ways [27]. The first one is changing concentration of carriers. High level of carriers raises the Fermi level. If the vacuum level is fixed, the work function will decrease. The second way is modifying the surface dipole. The surface dipole causes the change of vacuum level. If the Fermi level is unchanged, the work function will change with the modification of the surface dipole.

The different work function from the ITO thin film samples with different tin doping

level was reported [27]. The difference results from the different Fermi level duo to the different concentration of carriers. Since the concentration of carriers affects work function of ITO thin films, the factors which affect the concentration of carriers also have influence on work function of ITO. The defect type in ITO is already discussed. The major carrier in ITO is donors from tin ions. In the deposition processes, the tin ions trend towards formation of neutral clusters under high oxygen pressure. The deposited ITO films have low electrical conductivity and high work function. The ITO films deposited under reducing conditions have high electrical conductivity and low work function.

The work function of ITO also depends on surface conditions. The surface contaminant is one of the factors affecting the work function of ITO significantly. The UPS measurement takes place in the ultrahigh vacuum. This is another reason for UPS to become a good method to measure work function. However, most of ITO samples are prepared ex-situ. The contaminant removal before the work function measurement has to be adequately addressed. Numerous surface treatments are developed to remove the surface contaminant from ITOs. The efficiencies of contaminant removal are different for these treatments. Moreover, some of these treatments may change surface properties, such as chemical composition, morphology, and chemical activity. Enough attention must be paid to these treatments because the post-deposition treatments affect work function of ITO [27].

The conventional treatment to remove the surface contaminant is using organic solvents, for example acetone and methanol. This method is damage-free for ITO samples. However, it has two drawbacks. It cannot remove surface carbon contaminant completely, and it will introduce hydrocarbon contaminant on the surface [28]. Hydrocarbon contaminant can reduce the work function of ITO significantly [29][30]. A. Chaney et al. used vibrational analysis with

HREELS to revealed that the base-cleaning with alcoholic-KOH could remove graphitic carbon but leave olefinic hydrocarbon [28]. This cleaning method decreased work function of ITO [28].

UV-ozone irradiation is a widely used approach to remove surface contaminant of ITO. It can remove the surface carbon contaminant efficiently. However, it cannot remove it completely. The residual carbon contaminant is detectable for XPS. According to the change of line-shapes of C1s peaks, Song et al. concluded that the UV-ozone treatment changed the chemical states of the residual carbon [22]. If UV-ozone irradiation is performed as an ex-situ treatment, the UV-ozone treated ITO surface will be exposed in air. M. Bermudez et al. pointed out that there was 0.5-0.8 monolayers of adsorbed carbon content on the surface of ITO when the freshly UV-ozone treated ITO sample is exposed in air [31].

UV-ozone treatment is one of oxidation treatment. Some of literatures reported that the UV-ozone treatment can introduce oxygen ions in ITOs to enhance the work function [8][30]. R. F. Minibaev et al. investigated the relationship between the work function and the surface oxidation level via first-principle calculation [8]. They set a different number of oxygen ions in the surface region in the computation. The calculation result revealed that the work function decreased with the reduced number of oxygen ions on the surface. In these literatures, the work function change is attributed to the change of Fermi level. When oxygen ions are introduced into ITO, the oxygen vacancies decrease, and the neutral defect clusters $(2\mathrm{Sn_{In}} \cdot \mathrm{O_i})^{\mathrm{x}}$ increase. The both changes will cause the decrease of carriers. As a result, the Fermi level shifts downward. Finally, the work function of ITO increases.

Plasma and sputtering were also reported to be employed for removing surface contaminant from ITOs. The most reported plasma and sputtering are oxygen plasma and Ar^+ sputtering. Oxygen plasma has the similar efficiency as UV-ozone treatment for surface carbon

removal [28][30]. The plasma cannot remove the surface carbon contaminant completely. However, the work function can be enhanced by oxygen plasma [22][28][30]. C. C. Wu reported that the oxygen plasma treated ITO enhanced the efficiency, brightness, and reliability of ITO-based organic light emitting devices [23]. The experimental result displayed the improved hole injection ability at the ITO/organic interface. It indicated the increased work function of plasma treated ITO. Besides surface carbon contaminant removal, oxygen plasma oxidizes the ITO samples and introduce oxygen ions in ITO structure. It causes shift downward of Fermi level. This is the reason for enhanced work function of ITO with oxygen plasma treatment.

H_2 plasma treatment on ITO was also reported in literature. The H_2 plasma treatment decreased work function of ITO because oxygen ions were removed from ITO [23][30]. Ar^+ sputtering has the best efficiency for carbon removal. It can remove surface carbon contaminant from ITO completely [28][32]. The contaminant-free surface doesn't mean the highest work function of ITO. Ar^+ sputtering results in oxygen preferential sputtering nature. Since the sputtering removes more oxygen ions than cations from the surface of ITO, the work function of sputtered ITO decreases [23][30].

The plasma and sputtering not only change the oxygen concentration but also modify the ratio of In/Sn on the surface of ITO [23][30][33]. K. Sugiyam et al. summarized that the work function of ITO is affected by three factors: carbon contaminant, O/In ratio, and Sn/In ratio in the surface region [30]. The O/In ratio has the strongest influence, and Sn/In ratio has the weakest influence. The Sn/In ratio represented the tin doping concentration. Lower doping concentration would lower the Fermi level to enhance work function of ITO [30].

It seems that the oxidation surface treatments such as UV-ozone irradiation and oxygen plasma are the best approaches to enhance work function of ITO because they can remove

surface contaminant and introduce oxygen ions simultaneously. Any reducing treatments such as H_2 plasma and Ar^+ sputtering are not capable to enhance work function of ITO. The only mechanism of work function change reported in literatures is shifting the Fermi level by changing carrier concentration. Actually, the surface conditions of ITO are complex. There is more than one factors for the work function change. In this dissertation, more factors affecting work function is discussed, and different explanations for the relationships among O/In, Sn/In, and work function are given.

CHAPTER 3

EXPERIMENTAL TECHNIQUES

3.1 Surface Treatments

3.1.1 UV-Ozone Radiation

UV-ozone irradiation is one of the dry surface treatments. It is widely used in electronics industries for surface cleaning or modifying physic-chemical properties of surfaces of films.

UV-ozone treatment possesses several significant advantages. First, the degree of damage on the sample surface is lower than other techniques such as plasma or sputtering. Since no high-speed particles bombard the sample surface in the UV-ozone radiation, UV-ozone radiation is a mild technique for removing surface contaminants. The cleaning efficiency could be as similar as that of plasma treatments [30]. Second, the cost of UV-ozone treatment is low. The treatment can take place at any pressure and, therefore, does not need a high vacuum which costs much. Third, the efficiency can be adjusted conveniently. The efficiency is ruled by the process parameters which are easy to control. The parameters include lamp power, lamp-subject distance, exposure time, pressure of feed gases, and operating temperature [34]. For instance, just increasing the exposure time from 10 to 20 minutes can decrease the percentage of carbon contaminant on the surface of ITO from 14.38% to 12.38% [35].

The layout of UV-ozone device is simple. UV source and oxygen flow are introduced into a chamber. Samples are placed in the chamber facing the UV source for surface cleaning or modification. The UV-ozone radiation also can take place in air. In this case, the oxygen flow is not necessary.

UV light can be generated by many sources. Mercury vapor lamps and fluorescent lamps are commonly used to produce UV light. The wavelength of UV light is from 100 to 400 nm.

The reaction in the UV-ozone radiation is per the following [36]: When oxygen gas is exposed under the UV light with the 184.9 nm wavelength, the oxygen molecules are excited. Then the molecules are dissociated into oxygen atoms. The dissociated oxygen atoms could react with other oxygen molecule to form ozone. Under the radiation of UV light with 253.7nm wavelength, one O_3 molecular is dissociated again into one oxygen atom and one oxygen molecular. The dissociated oxygen atoms own high reactivity. They could react with many atoms and molecule to form oxides.

If the types of these formed oxides are gaseous or liquid, the product will vapor from surfaces. If the product is solid, other cleaning methods can be combined with UV-ozone treatment. The oxidation only happens on the surfaces. It could not affect the bulk of samples. The bulk could not be harmed accordingly.

UV-ozone treatment is not only a cleaning method but also a surface modification method. It can effectively improve adhesions between polymers and ceramics. For example, UV ozone treatment is employed on ITO substrates to decrease surface roughness and increase surface energies so that the deposited films have better qualities [37].

3.1.2 Sputtering

Sputtering is a process that atomic energetic particles bombard target to eject target material particles. The sputtering was first recorded by Willam Robert Grove in 1852 [38]. After developing for a century, it becomes a main method of film deposition, surface modification, and surface analysis.

The mechanism of sputtering can be simply described by an analytical theory [38]. The theory consists of three steps: (1) the incident ions bombard a target to generate recoiling target

atoms. Some of recoiling target atoms can be ejected from the surface of target; (2) The recoiling target atoms trigger cascade of collisions to produce more recoiling target atoms; (3) the recoil target atoms are ejected from the target.

Sputtering yield is an important quantity for sputtering. It is defined as number of target atoms ejected per incident ion. The sputtering yield is affected by many factors, for example species of ion-beam, angle between ion-beam and target surface, energy of ion-beam [38]. The ion beam species can be H, D, He, Ne, Ar, and Xe. When ion-beam bombards a target and sputtering occurs, the target atoms will be ejected and leave a crater in the surface of the target. The most part of ejected target atoms are from the top surface layer. A small part of the atoms are from the second layer or even deeper layers. With increased sputtering time, the crater become deeper and the bottom of the crater become rougher.

Sputtering is commonly applied in surface contaminant removal for science study. The efficiency of contaminant removal is high. However, there are some drawbacks of sputtering cleaning [38][39]: (1) sputtering damages topographical features of the sample. The damage can be recovered by annealing if annealing can be applied on the sample. (2) The incident ions may be implanted into the sample. The implanted ions also can be removed by annealing. (3) recoiling atoms also can be produced in the contaminant layer by ion bombardment. The recoiling atoms of the contaminant can be implanted into the bulk of the sample. (4) Preferential sputtering changes compositions of polymers and compounds.

When preferential sputtering happens, the different component atoms in the target are removed by different rates. Preferential sputtering is caused by many factors. I. Zaporozchenko et al. studied preferential sputtering in binary targets and concluded that preferential sputtering is

affected by sputtering yield of each component in the target, the angle of ion incidence, ion energy and mass, and surface binding energy of each component in the target [39].

3.2 Deposition Methods

3.2.1 Ion-Beam Deposition

When a target is sputtered by an ion-beam, the target atoms are ejected from the target with wide angular and energy distributions. These ejected atoms can be collected by placing a substrate near the target. The atoms reach the surface of the substrate and deposit on it. This process is the ion-beam sputter deposition (IBS).

The sputter deposited film usually exhibit good adhesion because the ejected target atoms have hyperthermal energies [38]. Meanwhile, the film has some drawbacks. Due to the wide angular distribution of the ejected atoms, a part of them are reflected by the surface of the substrate. If the target material is a compound, the composition of the deposited film will not mirror the composition of the target material because of the preferential sputtering. This issue can be solved by sputtering other targets simultaneously or creating a specific atmosphere. For example, when an oxide film is expected, the deposition will be done in the controlled oxygen atmosphere to guarantee that the percentage of oxygen in the film meets the request. It is difficult but still possible for IBS to deposit stoichiometric compound films.

3.2.2 Magnetron Sputtering

The basic sputtering process has limitations such as low deposition rate and high substrate heating effect in film deposition applications. In early 1970s, the balanced magnetron sputtering was invented to overcomes the limitations of the basic sputtering [40]. After

developing for decades, the magnetron sputtering technique already have many branches for example DC magnetron sputtering, rf magnetron sputtering, pulsed magnetron sputtering, and close-field unbalanced magnetron sputtering.

DC magnetron sputtering has relatively simply layout in the magnetron sputtering techniques. To begin with, the basic DC sputtering apparatus is introduced. The basic DC sputtering apparatus consists of three parts: a target, a low- pressure glow discharge, and a substrate. The schematic layout is shown in Figure 3.1. The electric potential is applied on the target and the substrate. The target must be made of conductive materials. The target is usually negatively charged as a cathode, and the substrate is positively charged as an anode. Noble gases, such as argon, are introduced into the sputtering chamber to generate glow discharge plasma. To maintain the high vacuum in the chamber, the pressure of argon must be low. A voltage, which exceeds the striking voltage of the gas, is applied on the gas. Then, the glow discharge is ignited. The produced Ar^+ ions between the target and the substrate are accelerated in the electronic field to bombard target materials. The bombardment will kick target atoms and electrons out from the target. The kicked out electrons, named secondary electrons, will strike argon atoms. In this process, argon atoms, are stroke by secondary electrons, will emit electrons to form Ar^+ ions. The generated Ar^+ ions continue to bombard the target. The secondary electrons keep the plasma continuing. Ejected target atoms moving toward the substrate will land on the substrate and form a film. Since the target atoms have high kinetic energies, the substrate will be heated by the striking. The high temperature greatly affects the structures and properties of deposited films [41]. Besides the high temperature, this rough sputtering apparatus has another fallback, low ionization, which blocks the utilization of sputtering [42]. The low ionization causes low deposition rate.

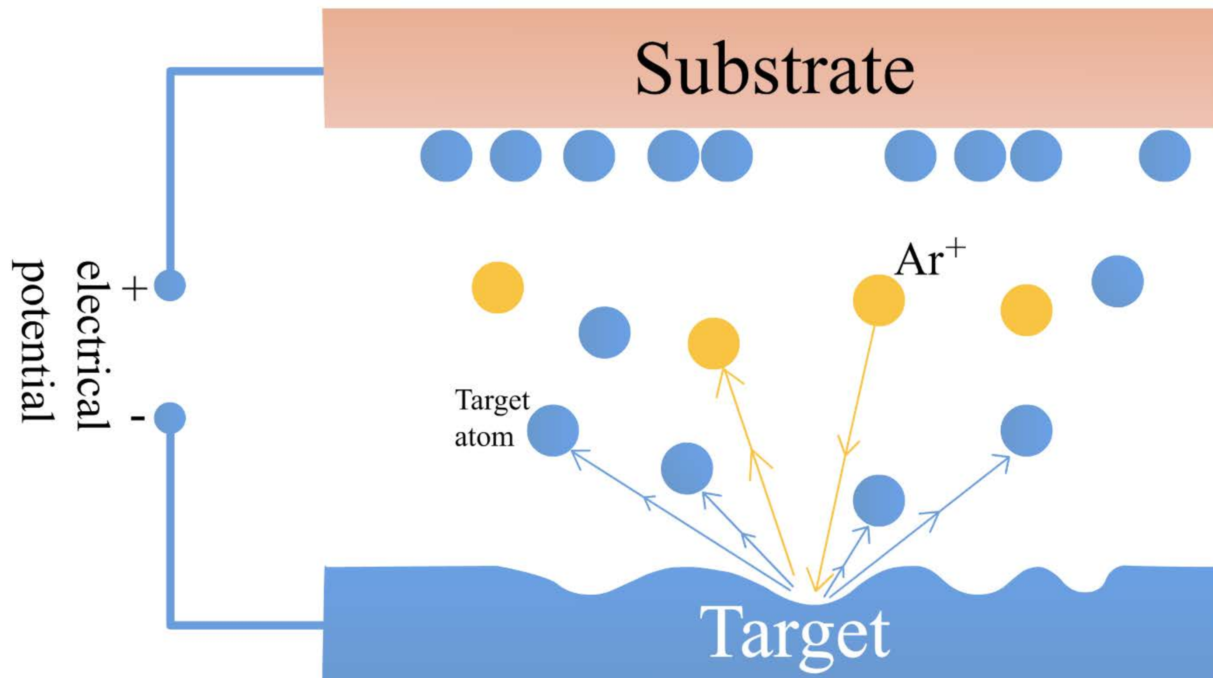

Figure 3.1 Schematic layout of basic DC sputtering apparatus.

To overcome the fallbacks of the basic DC sputtering apparatus, many improvements have been made. The significant improvement is the adoption of magnetron. Two magnets are installed around the target. One is at the backside center point of the target, and the other is ring-shaped, circling the center point. The magnetic fields could control the trajectories of the secondary electrons. That the Lorentz force will constrain electrons at the vicinity of the target will increase probability of ionization of argon atoms. Experiments proved that the ionization efficiency increased tremendously [42]. Besides that, the target utilization also raised from less than 30% to 60% [42]. In some sputtering apparatus, the magnets are rotatable. The utilization of the rotatable target can reach 90% [42]. Some sputtering apparatus adopt unbalanced magnetrons, which is achieved by strengthening the outer magnetic rings. The unbalanced magnetron can supply open magnetic fields. Some of the magnetic field lines are perpendicular

to the target surface. Secondary electrons can move along these lines. The activity region of secondary electrons is no longer constrained in the vicinity of the target. Consequently, the region of dense plasma is extended. The unbalanced magnetron sputtering provides high ion flux with low kinetic energies [40]. The deposited films possess fewer defects than ones deposited by balanced magnetron sputtering.

DC sputtering is only capable of sputtering conductive materials. Some metal oxides are insulators. The nonconductive targets could not be used in DC sputtering systems. The metal targets are still used to deposit metal oxide films. In this case, oxygen gas is introduced accompanying noble gases. Oxygen atoms react with metal atoms in the sputtering chamber to form metal oxides. The metal nitrides also can be obtained in the same way. This method is not the best method because target poisoning cannot be avoided. Radio frequency (RF) sputtering is usually adopted to deposit insulator films.

3.3 Characterization Techniques

3.3.1 X-Ray Photoelectron Spectroscopy (XPS)

X-ray photoelectron spectroscopy is a powerful surface chemical analysis technique. The operation is in the ultra-high vacuum system. The light source is the soft X-ray. Due to the poor penetration of the X-ray, XPS can only probe the several top atomic layers of samples. It is widely used to analyze atomic compositions and chemical states in the surface regions of samples.

3.3.1.1 Principle

Energy levels of an atom can be classified into core levels and valence levels. Electrons

in core levels tightly bond with nuclei, and the electrons in valence levels weakly bond with nuclei. The energy levels can be described by nl_j, where n is the principal quantum number, and l is the orbital quantum number [43]. The total angular momentum quantum number is j= (l+s) [43]. The spin angular momentum quantum number s is ±1/2. According to the value of j, it is known that only s orbital has one value of j, and the other orbitals, p, d, and f, have two different values of j. As a result, signal electrons from s orbitals give rise to singlet peaks, and signal electrons from p, d, and f orbitals give rise to doublet peaks. The theoretic ratio of the intensities of the doublet peaks is [2(l+1/2)+1]:[2(l-1/2)+1] [43].

The soft X-ray will be absorbed by electrons in core levels when the X-ray strikes a sample. The excited electrons near the surface of the sample have a chance to escape from the sample. In all excited electrons, the elastic scattered electrons and inelastic scattered electrons are mixed together. The elastic scattered signal electrons give rise to the core-level XPS spectra, which can reflect the density of state of the atoms. A core-level XPS spectrum usually contains both characteristic peaks and background. The characteristic peaks with relative high intensities are attributed to the elastic scattered electrons. The background is attributed to the inelastic electrons. In some case, the intensities of background could be higher than that of characteristic peaks. The characteristic peaks will be buried by the background.

If the kinetic energy of elastic scattered photoelectrons is KE(s), the frequency of the X-ray is υ, the work function of the sample is ϕ(s), and the binding energy of electrons is BE, an equation can be written as

$$\mathrm{BE} = \mathrm{h}\upsilon - \mathrm{KE(s)} - \phi(\mathrm{s}) \quad \text{Equation 3.1}$$

In XPS measurement, the sample must be electrically connected with the spectrometer. The Fermi level of the sample and the spectrometer are aligned to the same level. The energy

level diagram of the sample and the spectrometer is depicted in Figure 3.2. According to Figure 3.2, the kinetic energy detected by the spectrometer is

$$\mathrm{KE(sp)} = \mathrm{KE(S)} - [\phi(\mathrm{sp}) - \phi(\mathrm{s})] = h\upsilon - \mathrm{BE} - \phi(\mathrm{sp}) \qquad \text{Equation 3.2}$$

where $\phi(\mathrm{sp})$ is the work function of the spectrometer, and KE(sp) is the detected kinetic energy of elastic scattered electrons. The final equation of the binding energy is

$$\mathrm{BE} = h\upsilon - \mathrm{KE(sp)} - \phi(\mathrm{sp}) \qquad \text{Equation 3.3}$$

The energy of the X-ray source is a constant for a specific anode. The value of kinetic energy of excited electrons is measured by the spectrometers. The work function of the spectrometer is one of parameters of the XPS system. It must be measured in the system calibration. The binding energy could be calculated by the Equation 3.3.

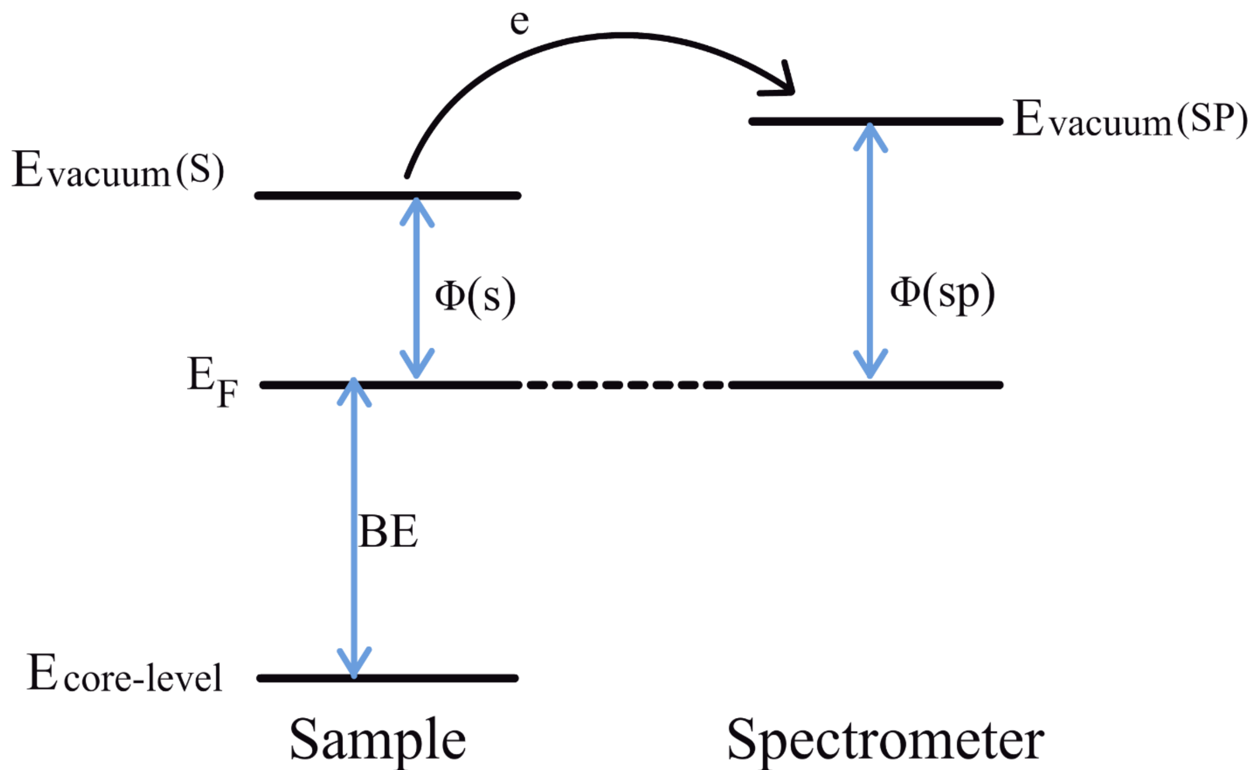

Figure 3.2 Energy level diagram.

3.3.1.2 Instrumentation

The XPS system is consisted of two parts: a light source and a spectrometer. The X-ray is generated when the electron beam strikes an anode. The kinetic energy of the electron beams is as high as several keV [44]. The anodes are made of aluminum and magnesium. When the electron beam with high energy strikes the metal (Al or Mg) anodes, the characteristic X-rays are emitted. The characteristic energies of Al Kα and Mg Kα are 1486.6 eV and 1253.6 eV, respectively. The anode is chilled by a water cooling system when the electron beam is striking. The energy resolution primarily depends on the light source. The light from the metal with a smaller atomic number will give higher energy resolution [44]. Thus, the Mg Kα source can provide better energy resolution than the Al Kα source. Since the X-ray is hard to focus on a small spot, XPS has poor lateral resolutions [44].

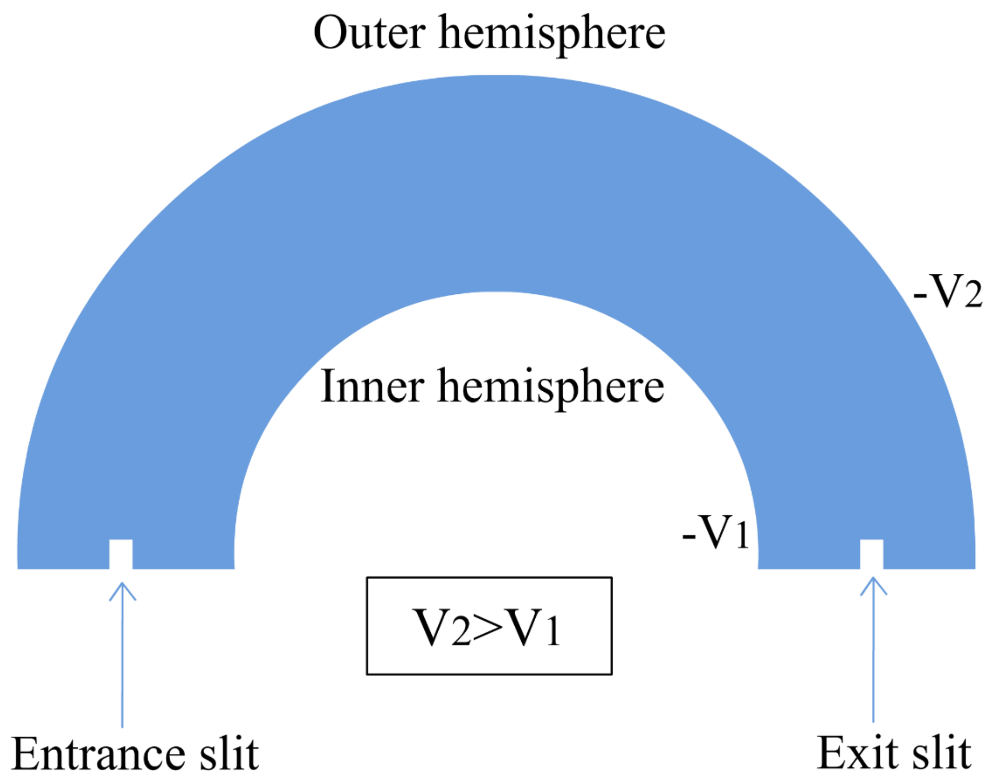

Figure 3.3 Schematic concentric hemispherical analyzer.

The currently widely used spectrometer is the concentric hemispheric analyzer [44], as shown in Figure 3.3. The different negative potentials are applied on both the outer hemisphere and the inner hemisphere. The potential on the outer hemisphere is smaller than that on the inner hemisphere. Signal electrons which have higher kinetic energies will be absorbed by the outer hemisphere, and the electrons with lower kinetic energies will be absorbed by the inner hemisphere. Only selective electrons which have their kinetic energy coinciding with the pass-energy can pass through the tub to reach the channeltrons. The resolution of XPS spectra is also controlled by the pass-energy. Using low pass-energy can collect data with high resolution.

3.3.1.3 Data Analysis

The XPS spectra can be classified into two types. One is wide scan, and the other is narrow scan. The wide scan records binding energies of all components in the sample from zero to thousands eV. The wide scan is usually called survey. The resolution of the survey is very low and is used to identify the elements of the sample. The narrow scan can provide chemical bonding information of the components of the sample. The quantification analysis also employs the narrow scan. The narrow scan only records a specific energy span and provides a spectrum with high statistics. Usually it focuses on the specific characteristic peaks and is also named core-level peak. Each peak represents a group of excited electrons with the same binding energy. These electrons are emitted from the same energy levels of the same atoms which have the same chemical environment. The centroid of peaks represents the binding energy of electrons at the energy levels before excited if the line-shape of the peak is symmetric. The peak intensity is an important parameter for quantitative analysis of atomic compositions. A sample, assumed to have homogenous elemental distribution, is scanned by XPS. The atomic compositions of the

elements can be calculated by the equation

$$C_A = \frac{I_A/S_A}{\sum_n \frac{I_n}{S_n}} \quad \text{Equation 3.4}$$

where I is the intensity and S is the relative sensitivity factor. The intensity is greatly influenced by the atomic photoemission cross-section σ [43]. The value of σ varies with the atomic number of elements. The cross-section also affects the sensitivity of XPS. For some elements with a small value of σ, the sensitivity can reach 0.1% atomic percentage [43]. Hydrogen and helium could not be detectable [44].

The line-shape of a core-level peak is not limited to one type. The simplest type is Gaussian form, the most common type observed in X-ray photoelectron spectra. This is symmetric structure. Intensities of these peaks are easily calculated. The height of peaks is usually used to calculate atomic compositions, instead of using the peak area. In X-ray photoelectron spectra, not all line-shapes are pure Gaussian forms. Due to the final-state effect and other complex reasons, the peaks in XP spectra display complex structures. If a complex peak is symmetrical, a mixed function called Gaussian-Lorentzian is employed to fit the peaks. The Lorentzian function adds lifetime broadening in the peak function [43]. If the peak is asymmetrical, the exponential tail function is added into the Gaussian-Lorentzian function to fit the asymmetric peak [43].

The width of a peak is another characteristic parameter that must be paid attention to. It is characterized by the peak width at half height (FWHM). The FWHM can be calculated by the equation [43]

$$\Delta E = \sqrt{\Delta E_n^2 + \Delta E_p^2 + \Delta E_a^2} \quad \text{Equation 3.5}$$

where ΔE_a is analyzer resolution. For the same analyzer, this value is a constant. ΔE_p is the width of photon source, and ΔE_n is the natural line width. The natural line width has a

relationship with the lifetime (τ) of core-hole states. The equation is

$$\Delta E_n = \frac{h}{\tau} \qquad \text{Equation 3.6}$$

where h is Plank's constant.

The elastic scattered electrons give rise to the discrete peaks with high intensities. The inelastic scattered electrons give rise to the satellite peaks with low intensities. The satellite peaks are usually continuous and considered as backgrounds. The source of the backgrounds is complex. Inelastic scattered electron is only one source contributing to the backgrounds.

Before calculating intensity of a peak, the backgrounds must be removed. The simplest function of background removal is the linear function. In the spectra of polymers, the difference between the heights of two sides of a peak is small. The linear function is usually adopted to remove background. A more complicated function to separate backgrounds is Shirley function, which is mostly used for the spectra which have steeply rising backgrounds [43]. Shirley function is not the most accurate function for removing backgrounds. It may cause huge errors if the edges of backgrounds are carelessly set [43]. The most accurate function is Tougaard function. When using Tougaard function, some parameters in this function are from experiments. Although this function is accurate, the parameters are hard to obtain. Due to this reason, Tougaard function is less popular than the Shirley function.

Peak fitting is a technique to separate overlapping peaks. In some cases, electrons from different elements have the same kinetic energies so that their characteristic peaks overlap together in the X-ray photoelectron spectra. These overlapping peaks must be separated in analysis. The criterion of assessing the quality of peak fitting is the physical meaning. Chi-square is usually used to judge the quality of peak fitting, but it is less important than the physical meaning. Plots can be fitted with multiple peaks with random binding energies and intensities. In

this way, the value of chi-square can be small. However, if these peaks have meaningless physical meanings, the fitting is considered totally wrong. In general, the peak fittings with good physical meanings have a relatively large value of chi-square.

Peak fitting is a complex technique. Many factors influence the result of peak fitting. These factors usually cannot be fully understood. As a result, although the researchers have acquired data, because peak fitting still lacks an assessing rule, such data cannot be evaluated for its accuracy but only for how many errors it can exclude [43].

The peak fitting must obey the physical natures of samples. First, the binding energies of fitting peaks must be fixed at the real energy of the relative elements. For example, since the binding energy of carbon at 1s orbital is 284.8 eV when scanned in a specific XPS system, the binding energy of carbon must be fixed at 284.8 eV in the peak fitting for the plots acquired from the same XPS system. Second, FWHM is a constant for atoms in the same chemical environment and scanned by the same system. The value of FWHM must be fixed in the peak fitting process. Third, the ratio of doublets must coincide with the theoretical ratio. The theoretical ratio can be calculated by the equation $[2(l+1/2)+1]:[2(l-1/2)+1]$. For example, for d electrons, $l=2$. Thus the theoretical ratio of $3d_{5/2}$ peak and $3d_{3/2}$ peak is 3:2. In the peak fitting process, the ratio of the relative peaks must be 3:2. To exclude more errors, experimental data could be referenced. The X-ray photoelectron spectra of metals are often referenced to analyze the spectra of metal oxides [43]. For instance, the ratio of $Ru3d_{5/2}$ peak and $Ru3d_{3/2}$ peak from Ruthenium metal is referenced in the peak fitting for Ruthenium oxides. This ratio is a constant for both the metal and the metal oxide.

For a compound, the core-level XPS spectra are not as simple as the spectra of elemental materials. These spectra usually display the complex line-shapes. Peak fitting requires

understanding of the mechanisms which the complex line-shapes derive from. The quality of peak fitting depends on what degree the natures of samples are understood. Moreover. in the peak fitting practice, some of parameters, such as FWHM and binding energy of a specific peak, cannot be obtained from measurement of different samples. It increases difficulty to do accurate peak fitting. Nowadays, peak fitting is still a challenge in XPS analysis.

3.3.2 Ultraviolet Photoelectron Spectroscopy (UPS)

Ultraviolet photoelectron spectroscopy (UPS) is another powerful surface analysis tool. In the beginning, it is used to analyze electronic structure of samples. After high energy ultraviolet light source is employed, UPS is also capable of surface chemical analysis. UPS has the same instrumentation as XPS. It consists of two parts: light source and spectrometer. In lab work, XPS and UPS are usually installed in one chamber, and these two instruments share the same spectrometer.

3.3.2.1 Principle

UPS and XPS have a similar principle. The difference between XPS and UPS in instrumentation is the light source. The energy of ultraviolet is from 10 eV to 100 eV. Ultraviolet with low energy, for example 10 eV, will excite electrons from valence levels. Since the electrons in valence levels are more sensitive to the chemical environment changes than the electrons in core levels, UPS can be used to monitor chemical reactions. According to the uncertainty principle, because of the low energy of ultraviolet, the natural linewidth is small. The small natural linewidth provides a high resolution of spectra. The energy separation due to opposite spins of electrons in the same orbitals can be observed in ultraviolet photoelectron

spectra. If the light source with high energy, for example 100 eV, is employed, the electrons in core levels can be excited. In this case, UPS acts as XPS.

Ultraviolet photoelectron spectrum is a counts vs binding energy plot. The principle UP spectra, the angle integrated photoemission spectra, reflect the density of states of samples. The angle resolved photoemission spectra can draw electronic structure of k-space. The samples detected by UPS could be gases, liquids, and solids. Since no surfaces exist for gaseous samples, the photoemission process that happens in gas is simple. The electrons are excited by the incoming Ultraviolet and escape to the vacuum. Photoemission in solids is more complex than it is in gas. A three steps model is adopted to describe the photoemission process from solids in UPS by Berglund and Spicer [44]. In the first step, electrons are excited by incoming photons. In the second step, the excited electrons transport to the surface of samples. In the last step, electrons escape to the vacuum.

3.3.2.2 Instrumentation

In UPS measurement, the light source is ultraviolet, which is the only difference between UPS and XPS. There are two types of ultraviolet light sources: resonance and continuous sources.

In a resonance lamp, noble gas is discharged to generate resonance radiation. The radiation process could be described by the following equations [44]:

$$2He \rightarrow He^{*}, He^{+}$$

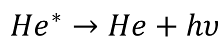

$$He^{*} \rightarrow He + h\upsilon \quad \text{Equation 3.7}$$

where He* is the He atoms with an electron in exciting states.

The emission spectra depend on the pressure of noble gases and applied current. At

relatively higher pressures and lower currents, emission happens on electrons in 2p states of He atoms. After emission, excited electrons fall back to 1s states, namely the ground states. The characteristic energy of emitted ultraviolet is 21.21 eV [44]. If emission happens on He^+ ions, the characteristic energy is 40.8 eV [44].

Because of the low characteristic energies from He gas, no materials can be made of the hermetic windows for the resonance lamps. As a result, a separate pumping system is employed for the resonance lamp. However, noble gas still has a large chance to drift to the sample/spectrometer section. If the XPS and UPS are installed in one chamber, the chamber must be pumped for a long time after UPS is done.

Another type of light source is the continuous source. Electrons are accelerated in a synchrotron to emit radiations with continuous energy spectra. The energies of the radiations can be high, which is up to 100 eV. If the ultraviolet with high energy is employed, the electrons in core-levels could be excited from samples. In this case, UPS could do the same work as XPS do.

There are two types of spectrometers. One is the hemispherical analyzer, the other is the cylindrical mirror analyzer. The hemispherical analyzers can be installed in a small size system. The acceptance area is large so that there is no strict request for the sample position. It gives space for other instruments such as ion guns and the X-ray sources.

For different types of samples, the requirement for samples is different. For gaseous samples, the gas is introduced as molecular beams into the analysis chambers. For liquids and solids, the potentials between samples and analyzers must be known in order to define energy scales. For metals and semiconductors, samples are electrically contacted with analyzers.

3.3.2.3 Data Analysis

In this dissertation, the data analysis of UPS focuses on solids. The energy level diagram of photoemission in UPS is the same as the diagram of photoemission in XPS. The kinetic energy is calculated by the following equations:

$$KE(s) = h\upsilon - BE - \phi(s) \qquad \text{Equation 3.8}$$

where KE(s) is the kinetic energy of electrons escaping from the sample.

The measured kinetic energy of signal electrons by spectrometer is

$$KE(sp) = h\upsilon - BE - \phi(sp) \qquad \text{Equation 3.9}$$

The binding energy of electrons at the Fermi level equals zero. The signal electrons from the Fermi surface depict a steep edge at the lower binding energy side. This edge is called the Fermi edge in UPS spectra.

Since the sample is electrically connected with the detector, the measured binding energy of signal electrons at the Fermi surface also equals zero. According to Equation 3.9, the following equation can be obtained:

$$KE(sp) = h\upsilon - \phi(sp) \qquad \text{Equation 3.10}$$

From Equation 3.10, it is obvious that the measured kinetic energy is a constant for a specific detector. Based on this conclusion, metallic samples are usually introduced in UPS to calibrate the Fermi level. When semiconductors are electrically connected with the spectrometer of UPS, the Fermi levels of the sample and the spectrometer will be at a same energy level. The Fermi level of semiconductors is in the band gap. There are not any electrons in the band gap. Therefore, no electrons will be excited from Fermi level to form a Fermi edge in the UPS spectrum. In this case, a metallic sample will be measured to provide a Fermi edge.

In the second step, in which electrons transport to surfaces, not all electrons are

elastically scattered. Part of electrons experience inelastic scattering and lose part of their kinetic energies. These inelastic scattered electrons show higher binding energies in UPS spectra than real binding energies. Elastic scattered electrons show discrete peaks which reflect density of states of samples. Inelastic scattered electrons show continuous peaks. The continuous peaks are considered as backgrounds. The background and discrete peaks overlap together. The intensity of background can be high enough to screen part of discrete peaks. The UPS spectra begin from the Fermi edges. The end edge is called the secondary edge which is formed by part of inelastic scattered electrons. Inelastic scattering happens under the Fermi surface. From the Fermi surface to the surface of the sample, kinetic energy is consumed to overcome attraction from nuclei, namely, the rest of the kinetic energy equals that charge of electron times work function of the sample. When electrons escape from surfaces, the kinetic energies of some of inelastic scattered electrons drop to zero. According to Equation 3.8, the following equation can be obtained:

$$\phi(s) = h\upsilon - BE \quad \text{Equation 3.11}$$

These electrons form a secondary edge. Finally, the electrons are detected by spectrometers. The final measured kinetic energy shown in the UPS spectra is

$$KE(sp) = h\upsilon - BE - \phi(sp) = \phi(s) - \phi(sp) \quad \text{Equation 3.12}$$

The width of the UPS spectrum is obtained by (Equation 3.10)-(Equation 3.12):

$$\Delta E = [h\upsilon - \phi(sp)] - [\phi(s) - \phi(sp)] = h\upsilon - \phi(s) \quad \text{Equation 3.13}$$

The work function of the specific sample could be calculated by the Equation 3.13. The precision of this method can be as high as 0.05 eV [44].

CHAPTER 4

EFFECTS OF ARGON SPUTTERING AND UV-OZONE RADIATION ON THE PHYSICO-CHEMICAL SURFACE PROPERTIES OF ITO

4.1 Introduction

Indium tin oxide (ITO) is one of the most important transparent conductive oxides (TCOs). It is widely utilized in many device applications such as organic light emitting diodes (OLEDs), organic photovoltaics (OPVs), and thin-film solar cells. The higher work function of ITO leads to better performances of the devices, for example, enhanced efficiency of the solar cell [45] and increased external electroluminescence quantum efficiency of OLED [23].

The work function is so important for the applications of ITO that extensive studies have been conducted to maintain and improve the high work function of ITO. Because the surface contaminant is well known to decrease the work function of ITO, many studies focused on the techniques of surface contaminant removal. The efficiencies of the contaminant removal and the influence of the surface treatments on the work function of ITO were reported [30][32][46]. According to the effect of the surface treatments on the work function of ITOs, these techniques can be classified into three groups: wet chemical etching, oxidation-based surface treatments, and reduction-based surface treatments. The wet chemical etching has very limited influence on the work function. The oxidation-based surface treatments enhance the work function and the reduction-based surface treatments decrease the work function. The work function is reported to be mainly affected by three factors at the surface of ITO: carbon-based contaminants, the O/In ratio, and Sn/In ratio [30]. However, beyond carbon based contaminants removal, there is a still confusion and lack of definitive determination as to the relationship between the evolution of surface chemistry and the increase/decrease of the work function of ITO after surface treatments.

The wet chemical etching is not an efficient technique for surface contaminant removal. While it can remove part of carbon-based contaminant, it introduces hydroxyls adsorbents which is an undesirable new contaminant for ITO [47]. The advantage of this technique is that it does not change surface O/In ratio and Sn/In ratio. However, the ITO treated by wet chemical etching, results in minor change in the work function [28][30].

The oxidation-based and reduction-based processes leads to modifications of surface composition in ITO. The oxidation-based processes such as UV-ozone radiation and Oxygen plasma introduce additional oxygen into the surface of ITO. The reduction-based processes such as H_2 plasm and Ar^+ sputtering remove oxygen from the surface of ITO. The Sn-rich surface is commonly reported on the degenerately doped ITO [22][48]. In the plasma and sputtering processes, ions with high kinetic energies bombard the surface of ITO leading to surface removal of Sn, hydrocarbon contaminants as well as oxygen. The oxidation-based and reduction-based surface processes remove more carbon-based contaminants from the surface of ITO than the wet chemical etching [30]. These surface treatments leads to changes in the surface O/In and Sn/In ratios, and consequently a change in carrier concentration which results in the Fermi level shift as authors report in literatures [23][30].

ITO is well known to have Sn-rich surface. The previous studies did not pay enough attention to the chemistry and bonding environment of the Sn-rich surface of ITO, which are important factors affecting the work function of ITO. It is essential to understand the chemical bonding change in the Sn-rich surface after surface treatments. It is the key to answer the question mentioned in reference [30] that why decreased Sn/In ratio either leads to increased or decreased work function of ITO.

In this study, XPS and UPS are employed to characterize ITO samples which are treated

by combination of UV-ozone radiation and Ar^+ sputtering. The ITO samples are exposed to the UV-zone radiation to minimize/remove surface hydrocarbon contaminants before introduction into the ultra-high vacuum (UHV) chamber. The Ar^+ sputtering process and in-situ XPS and UPS measurements are undertaken in the UHV chamber. The XPS measurements is used to determine the effect of Ar^+ sputtering on the surface composition and chemical bonds. The work function, as a function of Ar sputtering time (dose) change is determined by UPS measurements. The correlation between the Sn-rich surface, the induced modifications of bonding environment and the work function of ITO is demonstrated.

4.2 Experimental

The ITO/glass samples, used in this study, were purchased from Luminescence Technology Corp. The nominal sheet resistivity of the ITO films is 15 Ω/Cm^2. The thickness of the film is 0.7 mm. No detergent cleaning is performed on these samples to avoid introducing hydroxyls. Instead, the UV-ozone radiation is adopted to remove most of the native carbon-based contaminants from the surface of ITO samples. 30 minutes UV-ozone radiation is done before the samples are introduced into the UHV chamber for Ar^+ sputter and in-situ XPS and UPS characterization. The ultraviolet source is generated by a mercury lamp. The distance between the UV source and the sample surface is 10 centimeters. The UV-ozone treated samples are loaded into the XPS analysis chamber immediately to minimize the re-contamination from exposure to air.

The XPS and UPS measurements and Ar^+ sputtering are performed using a PHI 5000 XPS and UPS system. The Ar^+ sputtering system, XPS, and UPS are in the same UHV chamber for in-situ measurements. The kinetic energy of Ar^+ has an energy range 1-4 keV. The angle

between the Ar^+ beam and the sample surface is 45˚. The background pressure in the chamber is 10^{-6} pa during the Ar^+ sputtering process.

The X-ray source in this XPS system is a monochromatic Al K alpha radiation with energy 1486.6 eV. The angle between the X-ray beam and the sample surface is fixed at 45˚. The sample stage can be adjusted for angle resolved XPS (ARXPS) measurements. The Take Off Angle (TOA) is from 12˚ to 90˚. Two groups of pass energies and energy steps are used to record the XPS spectra: 11.75 eV pass energy and 0.1 eV energy step, and 23.5 eV pass energy and 0.2 eV energy step. The XPS system is calibrated by sputtering cleaned Au and Ag foils. In the UPS measurement, the ultraviolet source is a He-I source with the energy 21.22 eV. The UPS spectra were recorded with 2.85 eV pass energy and 0.005 eV energy step with a fixed TOA at 90˚. A -9 Volts bias voltage is applied to the sample stage to increase the intensity of the secondary edge and separate the secondary edges of ITO/glass sample from that of the analyzer. The Fermi edge is calibrated by Ar^+ sputter cleaned gold foil.

4.3 Results and Discussion

4.3.1 Removal of Surface Carbon-Based Contaminants

The carbon-based contaminant on the surfaces of ITOs are examined by C1s core-level XPS spectra. The intensity of the C1s peak represents the level of the carbon-based contaminant on the sample. The C1s spectra of the samples which are treated with different sputtering time are displayed in Figure 4.1. The spectra in Figure 4.1 are collected at TOA 30˚ to increase the surface sensitivity. The pass energy and the energy step are 11.75 eV and 0.1 eV, respectively. The kinetic enengy of the Ar^+ sputter is 1 keV. The background of the spectra is defined by using the Shirley function. The C1s peak of as-received ITO sample has high intensity which indicates

high level of surface carbon-based contaminant. After 30 minutes UV-ozone radiation, the intensity of the C1s peak decreases significantly. The peak area of the C1s peak of the UV-ozone radiation treated ITO is reduced by about 70% when compared to the as-recievd ITO sample. The intensities of the C1s peaks decrease further with increased time of Ar^+ sputtering. After 0.3 minutes Ar^+ sputtering, the C1s peak is buried in the background with a detection limit of about 0.1%. To examine the realiability of the small C1s peak for the ITO sample with 0.3 minutes sputtering, the peak area and the standard deviation are calculated. When the energy interval of C1s is defined in the region from 283.4 to 291.0 eV in Figure 4.1, the peak area of the C1s peak with substraction of the background is 1960 in counts, and the standard deviation is 586 in counts. The value of the poisson statistics factor equals the fourth cross-section parameter which is 3. If the calculated peak area is less than three times of standard deviation, the peak can be considered undetectable. Since the peak area of C1s is larger than three times of the standard deviation, the C1s peak, which represents carbon-based contaminant, is still detectable after 0.3 minutes Ar^+ sputtering.

In literature, ITO was reported to be capable to absorb adventitious carbon and hyroxyl even in UHV environment [32]. It is possible that 0.3 minutes Ar^+ sputtering already removes all the surface carbon-based contaminant or lowers the level of the contaminant under the detection limit of XPS. The small C1s peaks appear because the re-contaminantion happened on the Ar^+ sputter cleaned surface of ITO in the UHV chamber. To examine the re-contaminantion, a ITO/glass sample is loaded in the UHV chamber and exposed to the Ar^+ sputtering with longer sputter time and higher kinitic energy. The C1s peak is collected twice after each time of sputtering. The first spectrum is collected immediately after Ar^+ sputtering. The second collection is done after leaving the sample in the UHV for 1 hour. The ITO sample are sputtered

for 4 minutes (1 keV), and 4 minutes (1 keV) + 5 minutes (2 keV). In each time of sputtering, the two C1s spectra are most the same in position, line-shape, and intensity. It demonstrates that the detected C1s peak of the 0.3 minutes sputtered ITO does not result from the re-contamination. The immediately collected C1s peaks of the ITO sample with two times of sputtering are displayed in Figure 4.2.

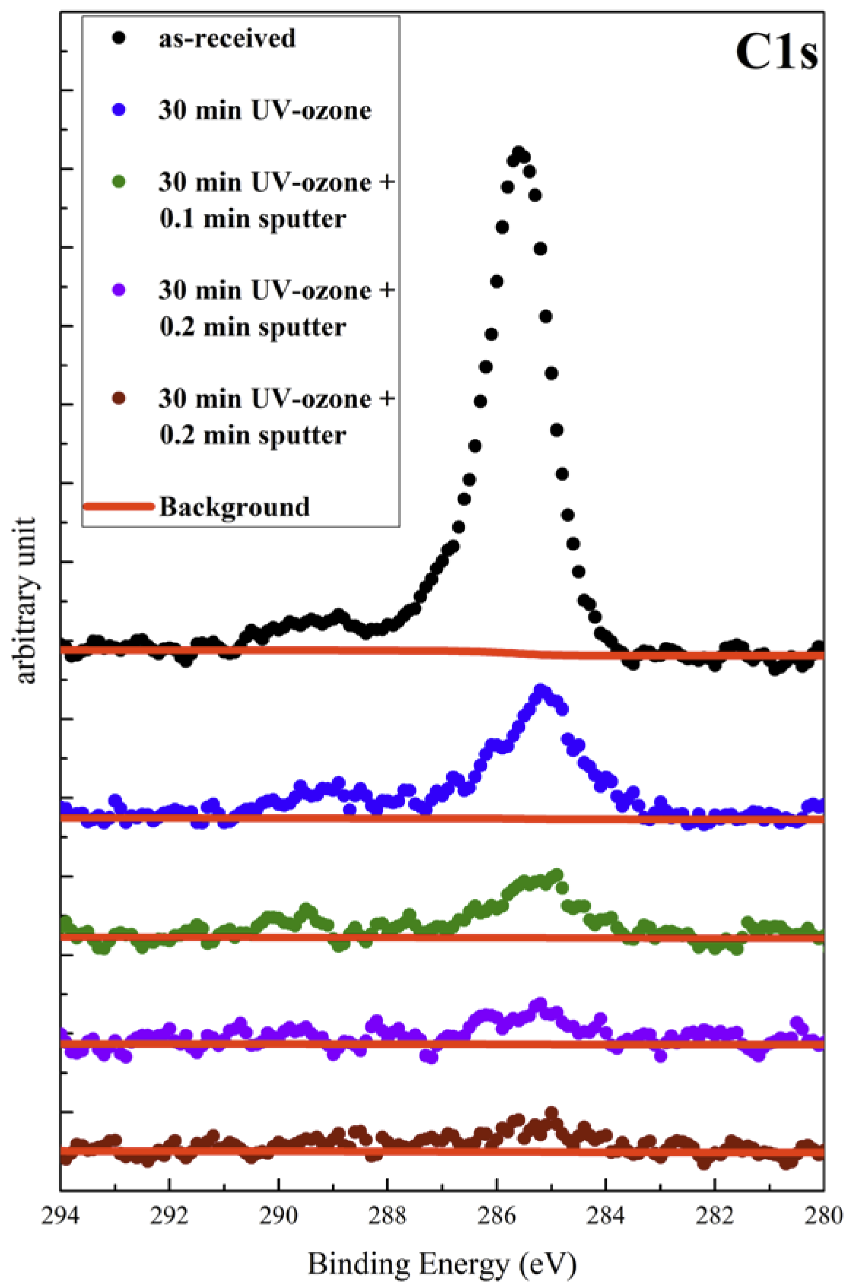

Figure 4.1 C1s core-level spectra of the ITO with different surface treatments.

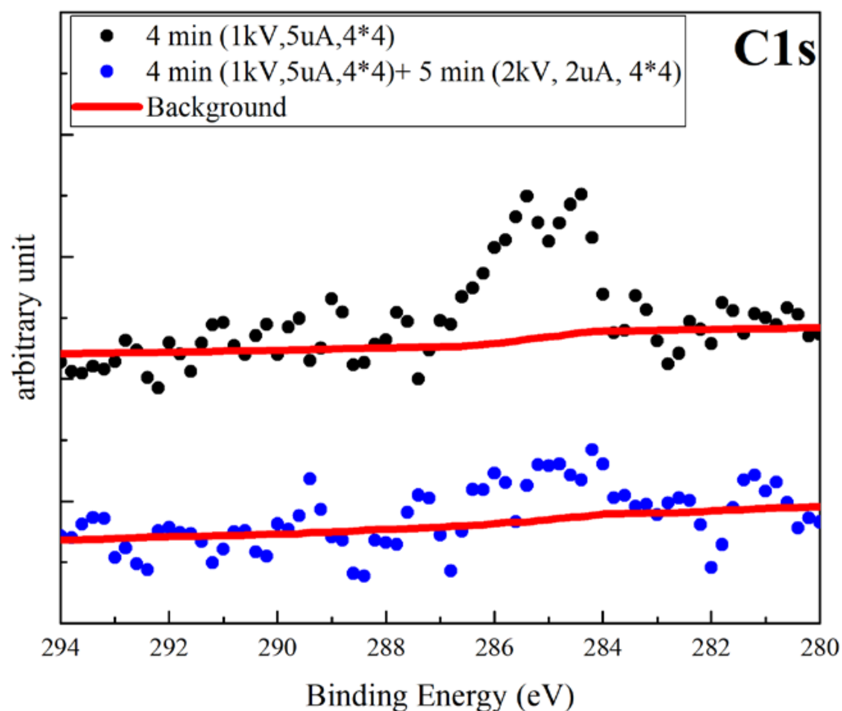

Figure 4.2 C1s core-level spectra of ITO with heavy Ar^+ sputtering.

To improve the statistics of the C1s spectra, the pass enernrgy and the energy step are 23.5 eV and 0.2 eV for the spectra in Figure 4.2. The background is also built by using Shirley function. After 4 minutes sputtering with 1 keV energy, the C1s peak is clear to see. The peak area is larger than 3 times of the standard deviation. After additional 5 minutes sputtering with 2 keV enerngy, the C1s peak cannot be seen. The calculated possible peak area is smaller than 3 times of the standard deivation. Thus, the level of the surface carbon-based contaminant is under the detection limit of XPS. From Figure 4.2 we can conclude that surface carbon-based contaminants are detectable after 0.3 minutes 1.0 KeV Ar^+ sputtering, and no detectable carbon re-contamination was observed on ITO kept in UHV for 1 hour. The C1s spectra in Figure 4.1 are collected immediately after Ar^+ sputtering, and the acquisition time is less than 1 hour. As a result, the small C1s peaks in Figure 4.1 represent the remaining carbon-based contaminant.

Figure 4.1 and Figure 4.2 indicate the difficulty to remove carbon-based contaminant from the surface of ITO by UV-ozone radiation and Ar^+ sputtering.

4.3.2 Sn-Rich Surface

The reported Sn-rich surface of the ITO/glass sample used in this experiment is demonstrated by ARXPS. The ITO sample is treated by 30 minutes UV-ozone radiation and 0.3 minutes Ar^+ sputtering with energy 1keV to miniminze the interference from the surface carbon-based contaminant. The In3d, Sn3d, and O1s core-level spectra are collected at TOA of 15˚, 30˚, 45˚, and 90˚. The spectra are displayed in Figure 4.3.

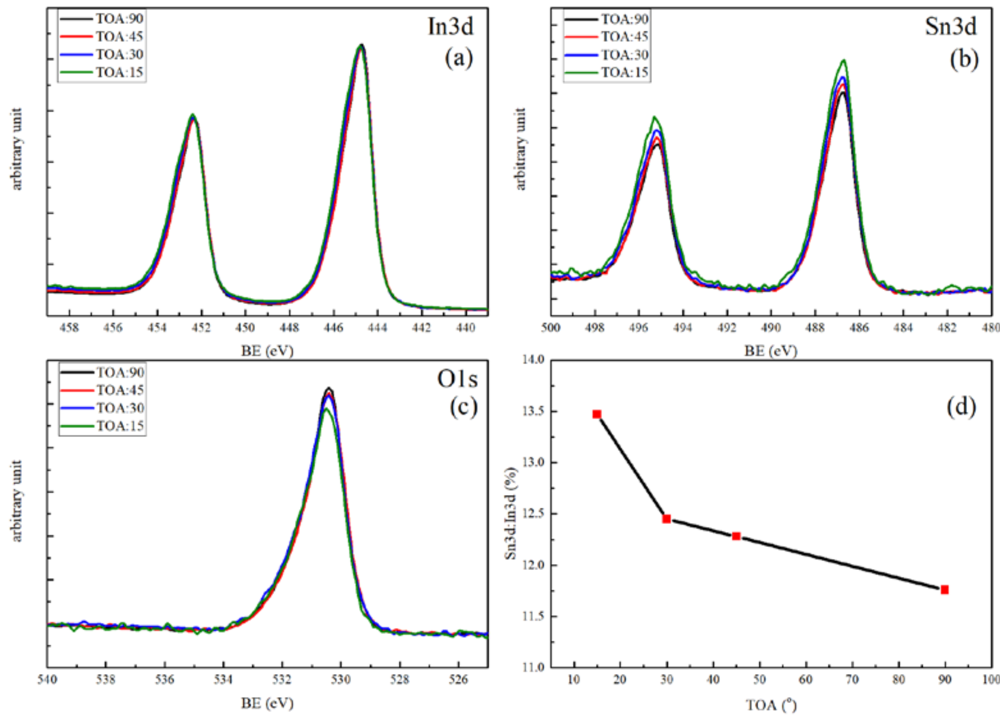

Figure 4.3 Normalized In3d, Sn3d, and O1s spectra collected with different TOAs.

Since spectra collected at low TOA have much lower intensities, the heights of the spectra collected at TOA of 15˚, 30˚, and 45˚ are enlarged to facilitate comparision. The In3d peaks are used as the references and normalized to the same height. The heights of the In3d

spectra collected at 15˚, 30˚, and 45˚ are multiplied 4.85, 2.35, and 1.60, respectively. The normalized In3d spectra are displayed in Figure 4.3(a). The line-shapes of these peaks have little difference. Thus, the In3d peak can be used as the energy/intensity references for the AR-XPS analysis. The heigh of the Sn3d and O1s spectra collected at 15˚, 30˚, and 45˚ are also enlarged 4.85, 2.35, and 1.60 times, respectively. The enlarged Sn3d spectra are shown in Figure 4.3(b). The intensities of Sn3d peaks decrease with increased TOAs. The peak areas of $In3d_{5/2}$ and $Sn3d_{5/2}$ are calculated by integrating the peaks after removal of backgrounds. The $Sn3d_{5/2}$ to $In3d_{5/2}$ ratio versus TOA is plotted in Figure 4.3(d). The Sn/In ratio decreases with increased TOA. This demonstrates that the surface of ITO is Sn-rich, most likely in the form of segregation between grain boundaries.

The zoomed O1s spectra is shown in Figure 4.3 (c). The O1s spectrum at TOA 15˚ has lower intensity. The XPS oxygen signal is comprised of both surface and bulk. The fitting of the O1s peak is presented in the section 4.3.5.

4.3.3 Comparison of Core-Level XPS Spectra between As-Received and Ar^+ Sputter Cleaned ITO Surface

The Sn-rich surface is demonstrated by using ARXPS. When the ITO sample is exposed to the Ar^+ sputtering, significant effects are expected in terms of composition and bonding environments. he sputtering firstly will have effect on the Sn-rich surface. The impact of the sputtering on the chemical and electronic properties of the Sn-rich surface of ITO is expected. The chemical bonds on the Sn-rich surface and their evolution under Ar irradiation are investigated using XPS measurements. Figure 4.4 shows the comparison between the XPS spectra of the same ITO/glass sample before and after Ar^+ sputtering treatment. The ITO sample was exposed for 30 minutes UV-ozone radiation as a pre-treatment. Then the ITO sample was

exposed for 0.1 minutes to Ar^+ sputtering with a kinetic energy of 1.0 keV.

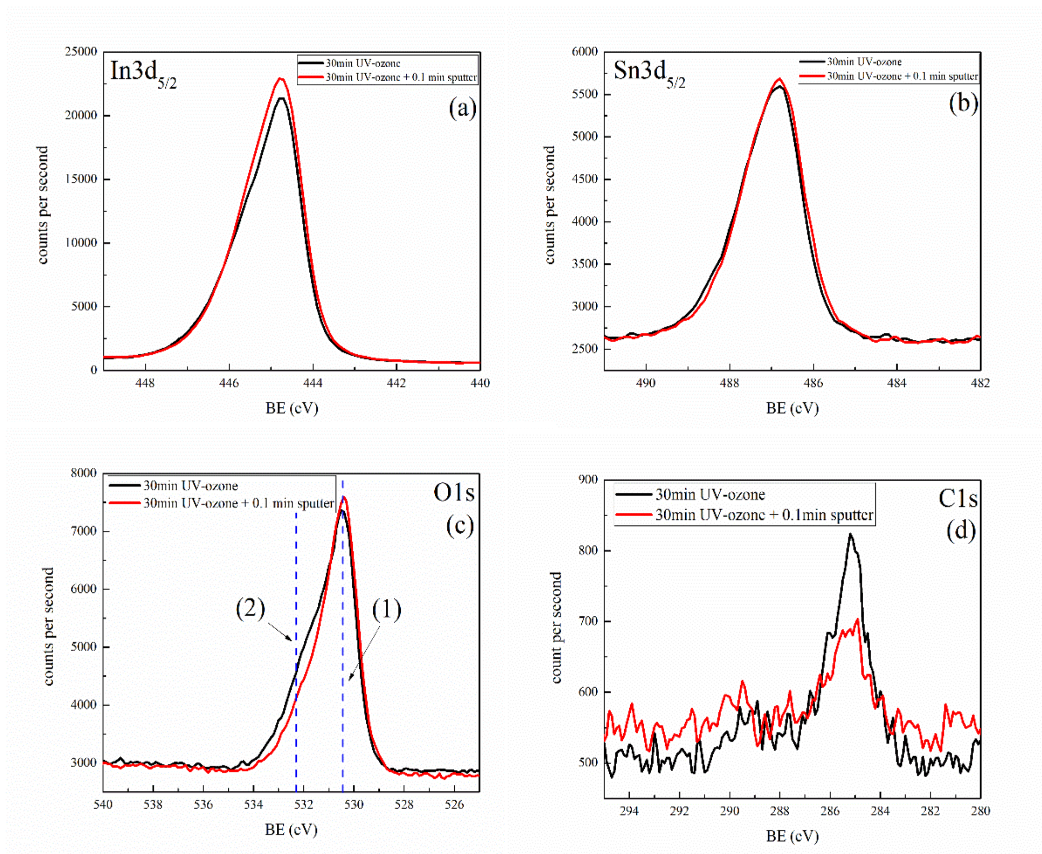

Figure 4.4 $In3d_{5/2}$, $Sn3d_{5/2}$, O1s, and C1s spectra of UV-ozone treated ITO with and without Ar^+ sputtering.

The $In3d_{5/2}$, $Sn3d_{5/2}$, O1s, and C1s core-level spectra of the two ITO samples are displayed in Figure 4.4 (a), (b), (c), and (d). The intensity changes of these spectra can be explained by the removal of Sn-rich surface. For $In3d5_{/2}$ peaks, the intensity increases after 0.1 minutes Ar^+ sputtering. The increase results from the removal of surface carbon-based contaminant and Sn-rich surface. The C1s spectra in Figure 4.4 (d) demonstrate that part of surface carbon-based contaminant is removed by Ar^+ sputtering. This is one reason caused increased intensity of $In3d_{5/2}$ peak. The Ar^+ sputtering also possibly removes part of Sn-rich surface simultaneously to result in the increased intensity of In3d peak. The removal of Sn-rich surface is confirmed by $Sn3d_{5/2}$ spectra in Figure 4.4 (b). If only carbon-based contaminant is

removed by Ar^+ sputtering, the intensity of $Sn3d_{5/2}$ should increases. There is no increase observed on the Sn3d peaks in Figure 4.4 (b) because part of Sn is removed from the surface to decrease the intensity. The removal of the Sn-rich surface is the other reason caused increased intensity of In3d peak. The O1s spectra in Figure 4.4 (c) show the different line-shapes. While the intensity increases after sputtering at position 1 (labeled in Figure 4.4 (c)), the intensity decreases at position 2 (labeled in Figure 4.4 (c)). In the sputtering process, the surface contaminant and the Sn-rich surface are partially removed. The O1s spectrum contains several components. In the O1s XPS spectrum, the components from the hydroxyl based contaminants and the Sn-rich surface decrease and the O1s components from the bulk of ITO increase.

If looking at the line-shapes of $In3d_{5/2}$ and $Sn3d_{5/2}$, one will find that all line-shapes are asymmetric. C. Körber and his co-workers gave two explanations to the asymmetry of the 3d core-level XPS peaks [50]. The first explanation is the final-state screening effect, and the second one is the Plasmon excitation.

In the photoemission process, core electrons absorb the incident photons and then are emitted from the original electron states. The photo emitted electrons leave core holes in the electron states. The core holes produce potentials to polarize the valence electron states and make the electron states unstable. The relaxation takes place to stabilize the electron states again. The "initials-state" is the electron state without relaxation, and the "final-state" is that after relaxation. The final-state effect can be recorded in XPS spectra and expressed in the form of binding energy shift, asymmetric line-shape, and multiplet splitting [51].

A. Kotani and Y. Toyozawa introduced a physical model to describe the final-state screening process [52], and this model is developed by G.K.Wertheim et al. [53][54][55]. This model is widely accepted to describe the asymmetry of 3d core-level spectra from degenerately

doped transition metal oxides [50][56]. According to the final-state screening effect, the raw $In3d_{5/2}$ spectrum consists of two overlapping peaks which are screened and unscreened peak. The energy separation between two peaks is less than 1 eV [50]. The two separated peaks give rise to the asymmetric line-shape. In the photoemission process, the potential generated by the core holes pulls down the orbitals in the conduction band. If electrons in the conduction band transfer to the core states and fill the core holes, it will result in a screened final-state. If the core holes are not filled by the electrons from the conduction band, it will give an unscreened final-state. The two peaks in the $In3d_{5/2}$ peak derive from the screened and unscreened final-states. The screened peak is always at lower binding energy side. The relative intensity of the screened peak decreases with reduced carrier concentration.

The final-state screening model is not the only model to explain the asymmetry of 3d core-level XPS peaks. The plasmon model gives an alternative explanation [50][56]. In a $In3d_{5/2}$ spectrum, the peak at lower binding energy side is the main peak, and the peak at higher binding energy side is a "unusually strong plasmon loss satellite" [50]. The energy separation between the main peak and the satellite peak "mirrors the plasmon energy" and the value is about 0.7 eV for 2% doped ITO and about 0.9 eV for 10% doped ITO [50]. This explanation is derived from the weak coupling model which is developed by Langreth [57]. Langreth stated that the intensity I of the intrinsic plasmon satellite increased with decreased conduction electron density N. The correlation can be expressed as $I \propto N^{-1/3}$. The conduction electron density N is low in ITO. It results in the plasmon satellite with unusually high intensity. However, the plasmon excitation should produce a serial of satellite peaks. Although the first satellite peak has unusually high intensity, the second satellite peak is expected to be observed from the spectrum at least.

In this study, the final-state screening mechanism is adopted to describe the peak components of the In3d peaks. Peak fitting is performed to separate the screened and unscreened peaks from the convoluted $In3d_{5/2}$ peaks. The peak fitting results of the $In3d_{5/2}$ peaks are displayed in Figure 4.5. Due to the almost the same line-shapes and the unchanged binding energy of In3d peaks, the In3d peak can be used as energy references to calibrate Sn3d and O1s peaks.

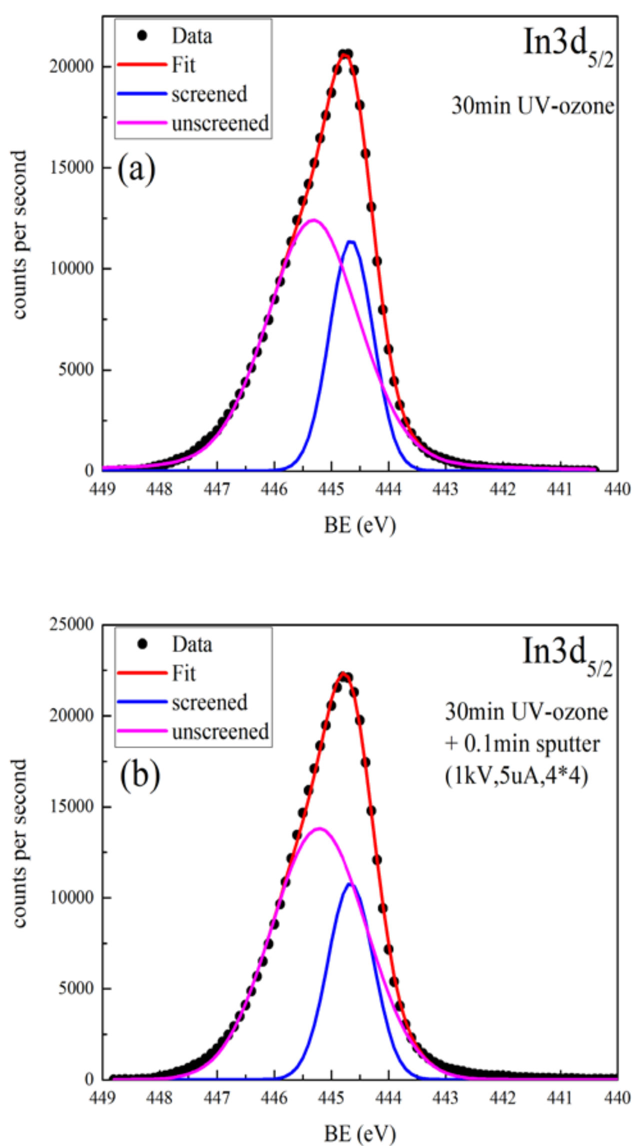

Figure 4.5 Peak fitting on $In3d_{5/2}$ peaks.

The final-state screening effect also happens on Sn3d spectra. Unlike the asymmetric $In3d_{5/2}$ peak, the asymmetric line-shapes of $Sn3d_{5/2}$ peaks in Figure 4.4 (b) cannot only attributed to the final-state screening effect. The signal electron of $In3d_{5/2}$ only come from the bulk of ITO. However, the signal electrons of $Sn3d_{5/2}$ come from the Sn-rich surface and the bulk of ITO. More caution must be paid on the Sn3d spectra. The $Sn3d_{5/2}$ peak of Ar^+ sputtered ITO shift 0.1 eV to the lower binding energy side in Figure 4.4 (b). It may indicate the change of the chemical bonding of Sn ions caused by Ar^+ sputtering. More measurements have been done to figure out the change of Sn3d peaks before and after Ar^+ sputtering.

4.3.4 Reduction of Surface Sn^{4+} and Components of Sn3d Core-Level Peak

The oxidation state of Sn ions in bulk of ITO is +4 [14][15][16]. The tin ions on the surface of ITO can be either Sn^{4+} or Sn^{2+} because of surface oxygen vacancies [58][59]. According to D. F. Cox and et al, it is possible that metallic Sn^0 exists on the (110) surface of SnO_2 [60]. The threefold-coordinated tin cation behaves like Sn^{2+}. If an additional in-plane oxygen vacancy is created on the threefold-coordinated tin cation, the tin cation will behave like metallic tin on the (110) surface of SnO_2 [60]. The ITO sample has Sn-rich surface. It is possible to find peaks of Sn^0, Sn^{2+}, and Sn^{4+} in the Sn3d spectrum of ITO. In the Sn3d spectrum, the core-level peaks of Sn^{4+} and Sn^{2+} are overlapped. The oxidation state of tin cannot be identified directly from a raw Sn3d spectrum. The peak fitting is a necessary process for the Sn3d spectrum analysis. The oxidation states of Sn are usually justified by using valance band spectrum instead of Sn3d spectrum.

Ar^+ sputtering also results in oxygen preferential sputtering effect [56]. During the sputtering process, more oxygen ions are removed than cations by Ar^+ sputtering. This effect

also happens on ITO [22][60][61]. The effect can be demonstrated by monitoring the change of Sn^{2+}/Sn^{4+} ratio. Although Sn3d peaks of Sn^{2+} and Sn^{4+} overlap together, the different oxidation states can be characterized by the valence band easily. In Figure 4.6, two valence band spectra of ITO samples are compared. One ITO sample is only treated by 30 minutes UV-ozone radiation. The other one is treated by 30 minutes UV-ozone radiation plus 0.3 minutes Ar^+ sputtering with kinetic energy 1 keV. When Ar^+ sputtering is applied, a tail between 2 to 4 eV appears at lower binding energy side of the valence band maximum.

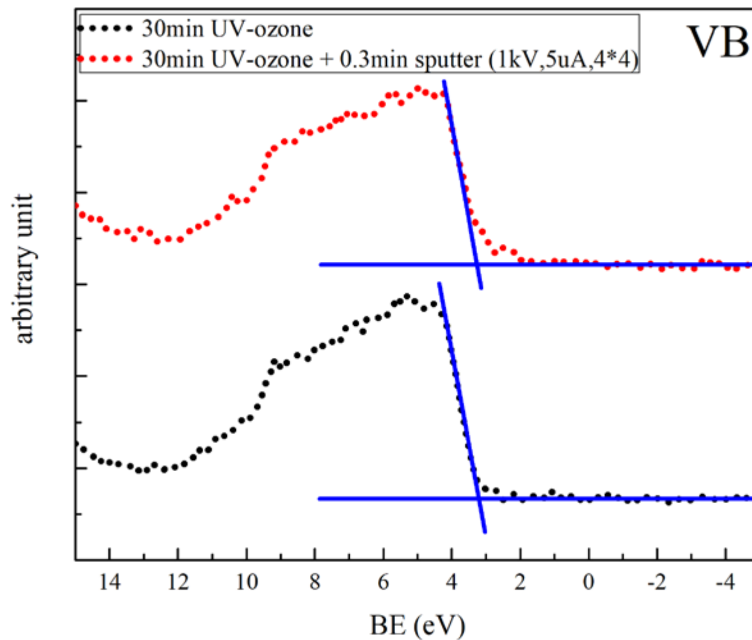

Figure 4.6 Valence band XPS spectra of ITO with different surface treatments.

Since the UPS spectrum has much higher resolution than the XPS spectra, the valence band spectra of ITO samples are also collected and displayed in Figure 4.7. According to C. Körber and et al, the valence band of ITO consists of four parts [50]. The peak, which is located at 3.9 eV below the Fermi level, derives from the hybridization state of O2p-In4d. The peak, which is the farthest from the Fermi level, is from the states of Sn5s. The position is at 10.5 eV below the Fermi level. There are two more peaks between 3.9 to 10.5 eV.

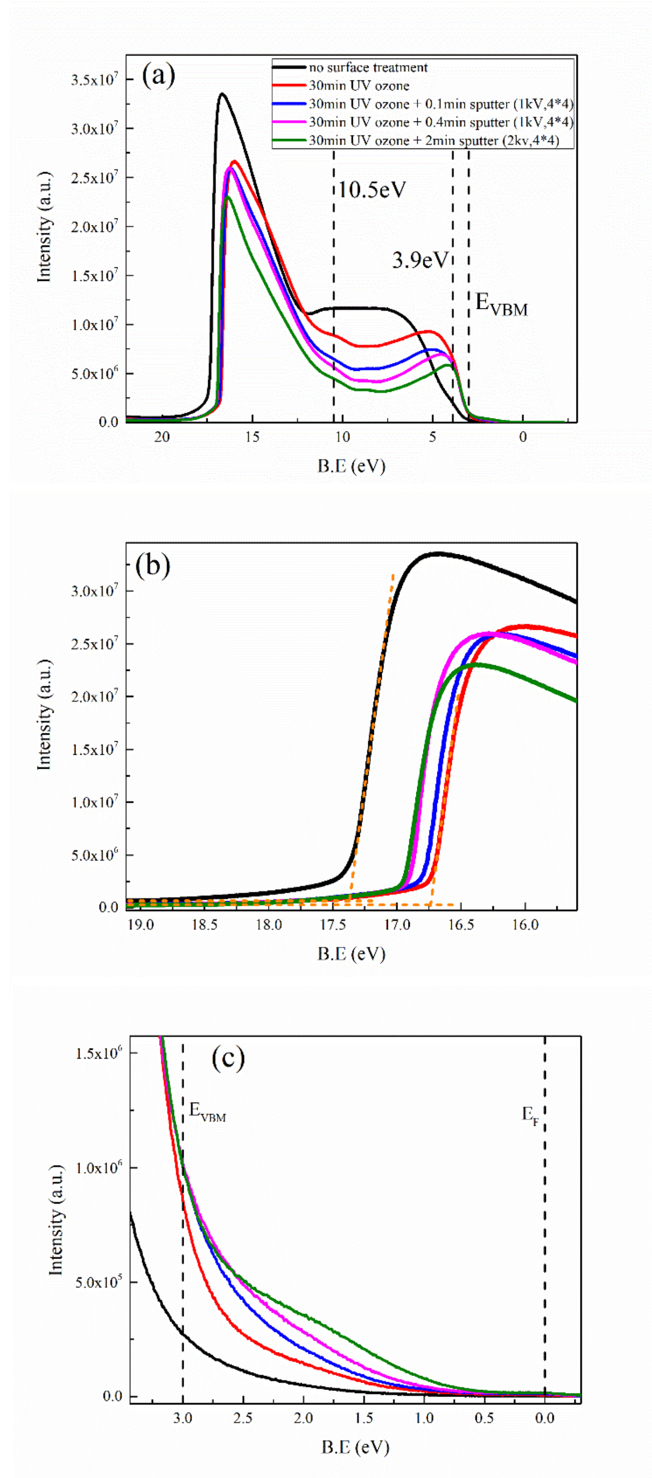

Figure 4.7 UPS spectra of ITO with different surface treatments.

The two peaks derive from the hybridization orbitals of the O2p-In5p and In5s-O2p. The band gap of the ITO is 2.8 eV [27]. The donor electrons in the ITO rise the Fermi level from the band

gap, where the Fermi level for semiconductors usually is, to the conduction band [62]. In Figure 4.6 and Figure 4.7 (c), the XPS and UPS spectra of the ITOs with Ar^+ sputtering display the tails rising from the valence band and approaching to the Fermi edge. Similar tails were reported in the studies on SnO_2 samples, and the studies concluded that the tail derives from the electron state of Sn^{2+} [60][61] [63][64]. The oxygen vacancies also produce a surface field. The field can induce the strong hybridization of 5s-5p of Sn^{2+} [59][60][61]. The hybrid states are expressed in the spectra as the tail between the valence band and the Fermi edge. When the level of the oxygen vacancies increase in the SnO_2 sample, the hybrid states will finally cross the band gap and reach the Fermi edge [60]. If the oxygen vacancies are filled by oxygen ions in the SnO_2 sample, the hybrid states will disappear in the spectra [60][62][63]. In Figure 4.6, the tails are examined by drawing two lines. The horizontal line is the background of the spectra. The leading valence band emission is fitted by linear extrapolation. The tail in the spectrum of the ITO sample, which is only treated by UV-ozone radiation, is barely seen. After 0.3 minutes Ar^+ sputtering, the tail becomes distinct. The tail indicates that partial Sn^{4+} ions are reduced to form Sn^{2+}. In Figure 4.7 (c), the intensities of the tails increase with increased Ar^+ sputter time. The appearance of the tails in the valence band demonstrates the existence of Sn^{2+} produced by Ar^+ sputtering.

The existence of Sn^{2+} is proved by the valence band spectra. Theoretically, the Sn^{2+} component in the Sn3d spectrum can be distinguished by de-convolution of the Sn3d peaks. The $Sn3d_{5/2}$ peaks in Figure 4.4 (b) show the similar line-shapes. The only difference between the two peaks is the shift. The shift is small but can be considered as the hint of the composition change. The distance of the shift increases with increased time of sputtering. In Figure 4.4 (b), the shift approximates 0.1 eV. The Sn3d spectra (not show in this article) are also collected from another

ITO sample which receives 30 minutes UV-ozone radiation and up to 2.0 minutes Ar^+ sputtering with the kinetic energy 2 keV. After 2.0 minutes sputtering, the Sn3d peak shifts to the lower binding energy side for 0.2 eV. The similar line-shape, the small separation between binding energies of Sn^{4+} and Sn^{2+}, and the small shift between Sn3d peaks make the peak fitting of $Sn3d_{5/2}$ peak difficult.

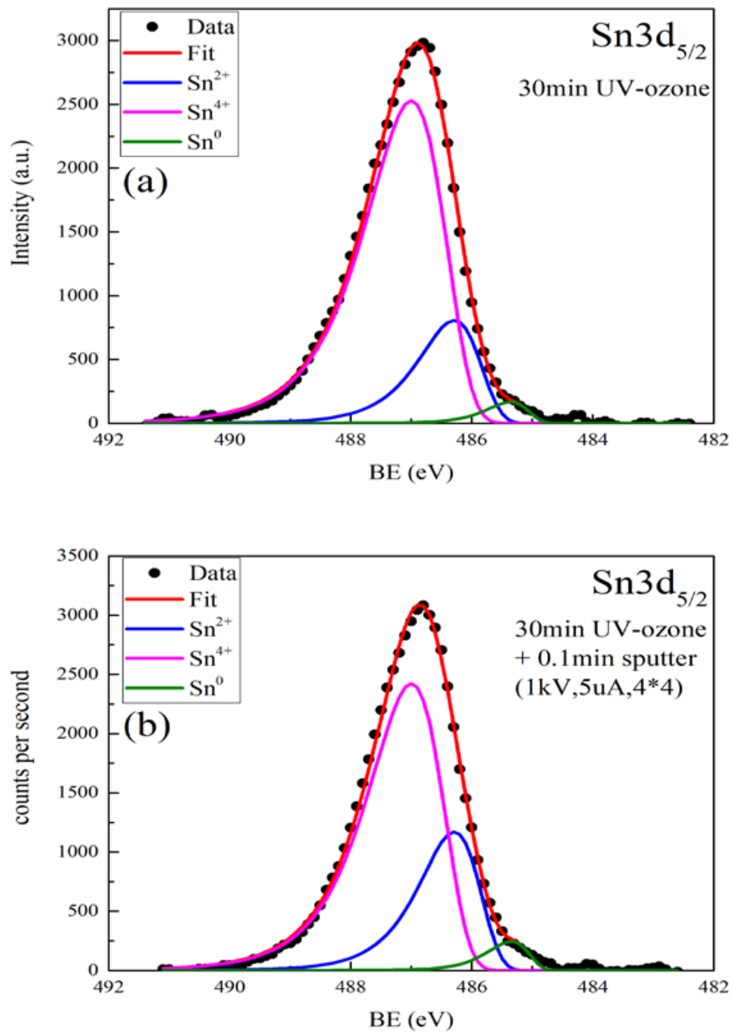

Figure 4.8 Peak fitting on Sn3d spectra.

The peak fitting is done on the $Sn3d_{5/2}$ spectra. Figure 4.8 shows the peak fitting result of the $Sn3d_{5/2}$ spectra displayed in Figure 4.4 (b). According to the final-state screening effect, the

peaks of Sn^{4+} and Sn^{2+} should contain the screened and unscreened peaks. In the peak fitting process, a pair of screened and unscreened peaks is convoluted into one asymmetric peak. The Sn^{2+} and Sn^{4+} peaks are represented by two asymmetric peaks. A third peak is created for Sn^0. The binding energy of the third peak is at 485.35 ± 0.01eV, which agrees with the binding energy of $Sn3d_{5/2}$ for Sn metal [65]. The Sn3d peak of Sn metal also exhibits asymmetric line-shape [66]. Thus, the peak of Sn0 is also represented by an asymmetric peak. The three peaks are built by Voigt function with 20% asymmetry. The peak fitting result reveals the existence of Sn^{4+}, Sn^{2+}, and Sn^0.

Figure 4.9 (a) shows the Sn^{2+}/Sn^{4+} intensity ratio changes with TOAs. The raw $Sn3d_{5/2}$ peaks are displayed in Figure 4.3 (b). The intensity of each component is from the peak fitting results. The Sn^{2+}/Sn^{4+} ratio at TOA=15˚ reaches the highest value 46.14%. The ratio decreases with increased TOA. The trend of the ratio change indicates that the Sn^{2+} is in the top surface.

The Sn^{2+}/Sn^{4+} intensity ratio versus Ar^+ sputter time is plotted in Figure 4.9 (b). The $Sn3d_{5/2}$ peaks are core-level spectra collected from the ITO sample which receives 0, 0.1, 0.2, and 0.3 minutes sputtering. The sample is pre-treated by 30 minutes UV-ozone radiation. The TOA is fixed at 30˚. The background is removed by using Shirley function. The peak fitting is done on the spectra with the same parameters which are used in Figure 4.8. The peak fitting result reveals the component change of Sn^{4+}, Sn^{2+}, and Sn^0 on the surface of ITO.

For the non-sputtered ITO sample, the percentage of Sn metal ($Sn^0\% = \frac{Sn^0}{Sn^0+Sn^{2+}+Sn^{4+}}$) is 2.7%, and percentage of Sn^{2+} ($Sn^{2+}\% = \frac{Sn^{2+}}{Sn^0+Sn^{2+}+Sn^{4+}}$) is 19.2%. The existence of Sn^{2+} and Sn^0 indicates two things. One is the weak oxidation capability of the UV-ozone radiation adopted in this experiment. The original purpose of using UV-ozone treatment is contaminant removal rather than oxidizing the surface. The intensity change of C1s and the existence of Sn3d peaks of

Sn^{2+} and Sn^0 prove that the UV-ozone radiation matches the purpose. The other thing is the high level of surface oxygen deficiency of the ITO samples. The commercial ITOs are usually prepared in the reduction conditions or annealing in the reduction conditions after preparation to maintain the high electrical conductivity. The ITO samples used in this experiment may experience reduction processes so that Sn^{2+}, and Sn^0 are detected in the surface region.

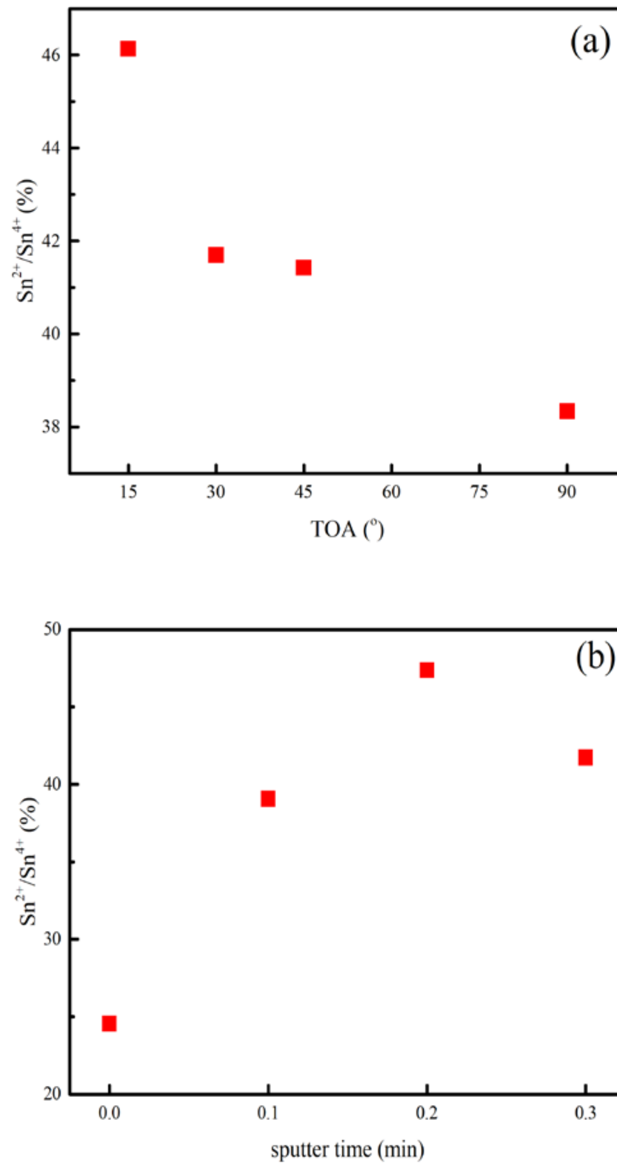

Figure 4.9 (a) intensity ratio of Sn^{2+}/Sn^{4+} versus TOAs. (b) intensity ratio of Sn^{2+}/Sn^{4+} versus sputter time.

Figure 4.9 (b) shows that the Ar^+ sputtering process increases the Sn^{2+}/Sn^{4+} ratio. Before sputtering, the Sn^{2+}/Sn^{4+} ratio is 25%. During the Ar^+ sputtering process, the ratio increases to 47% at 0.2 minutes sputtering. Then it drops to 42% at 0.3 minutes sputtering. Because the Sn3d peak continues changing shape and the overall position appears to shift to lower binding energy side with increased sputter time, the Sn^{2+}/Sn^{4+} ratio is expected to increase with shift.

4.3.5 Composition of O1s Peak

The components of O1s peak is complicated. The surface of ITO has high chemical activity. It is easy to absorb hydroxide and carbonaceous species, such as hydroxyl, CO and CO_2 [67]. The absorption even happens in UHV environment [32]. M. Brumbach et al. stated that water vapor could quickly react with freshly fabricated or cleaned surface of ITO to form hydroxide layer. CO and CO_2 would react then for the longer atmospheric exposure. The line-shape of O1s peak from the ITO always show asymmetric line-shape. The O1s core-level peak of ITO was interpreted in Brumbach et al's report [67]. The O1s peak consisted of three components. To facilitate the description, the three peaks are named peak A, peak B, and peak C. The binding energies of the three peaks increase from peak A to C. The peak A, which was located at the lowest binding energy side, was from the oxygen ion in the lattice sites. The peak B, which was at higher binding energy side of peak A, was related to the Sn doping and carbonate-like contaminants. The Sn doping correlated part was determined by comparing in-situ measured O1s peaks of ITO and In_2O_3. The authors also examined the O1s spectra of ITOs with different surface treatments. They demonstrated that the carbonate-like and hydroxyl-like contaminants were absobed on the surface of ITO samples. The carbonate-like contaminant

overlaped with the Sn doping related component in peak B. The peak C, which has the highest binding energy, belonged to the hydroxyl-like contaminant.

The change of O1s spectra in this study coincides with the descriptions in M. Brumbach et al's report [67]. In Figure 4.4 (c), the increased part at position 1 is from the oxygen ions in the lattice sites. The decreased part at position 2 is the peak of Sn doping correlated and carbonate-like contaminant. The Sn-rich surface is not considered by M. Brumbach et al. While they concluded that the peak correlated to Sn doping level decreased with decreased Sn/In ratio in XPS measurement, they also mentioned that the surface Sn/In ratio decreased with increased sputtering time [67]. If the Sn-rich surface is considered, the change of surface Sn/In ratio with increased sputtering time is evidently attributed to the Sn-rich surface. Thus, the Sn doping correlated peak should be assigned to the Sn-rich surface.

In this study, the O1s peak is fitted by three peaks: peak of oxygen in stoichiometric ITO lattice, peak of Sn-rich surface plus carbonate-like contaminant, and peak of hydroxyl-like contaminant. The peak fitting result of O1s spectra shown in Figure 4.4 (c) is displayed in Figure 4.10. The peak at the lowest binding energy is assigned to the oxygen in stoichiometric ITO lattice. The binding energies of Oxygen in In_2O_3 and SnO_2 are not distinguishable because the energy separation is only 0.1eV [68]. The oxygen in the ITO lattice is not expected to exhibit different binding energies. The peak at the middle position is assigned to Sn-rich surface plus carbonate-like contaminant. The peak at the highest binding energy is assigned to hydroxyl-like contaminant. The contaminant on the surface of ITO contains hydroxyl, C-O, C=O, hydrocarbon and water [29][32][67][69]. The hydroxyl-like contaminant has higher binding energy. It can be separated from other contaminants. The carbonate-like contaminant in O1s spectrum has the similar binding energy as Sn-rich surface has. It cannot be distinguished from the component of

the Sn-rich surface. Thus, the two components, Sn-rich surface and the carbonate-like contaminant, are represented by one peak.

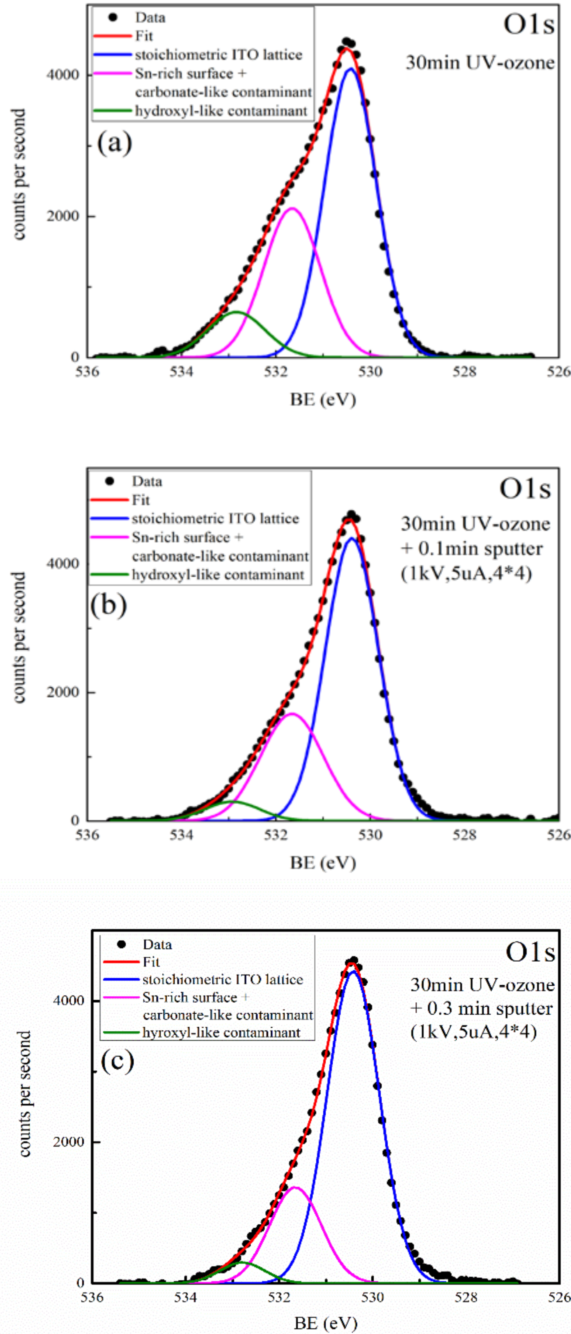

Figure 4.10 Peak fitting on O1s peaks.

4.3.6 UPS Measurement of Work Function

The work function is obtained from the UPS spectra. In Figure 4.7 (a), the full UPS spectra of the ITO samples with different surface treatments are displayed. The Fermi level is calibrated by the Ar^+ sputtering cleaned Au foil. The secondary edge is fitted by a linear extrapolation. The position of the secondary edge is defined as the intersection of the secondary edge and the base line which is shown in Figure 4.7 (b).

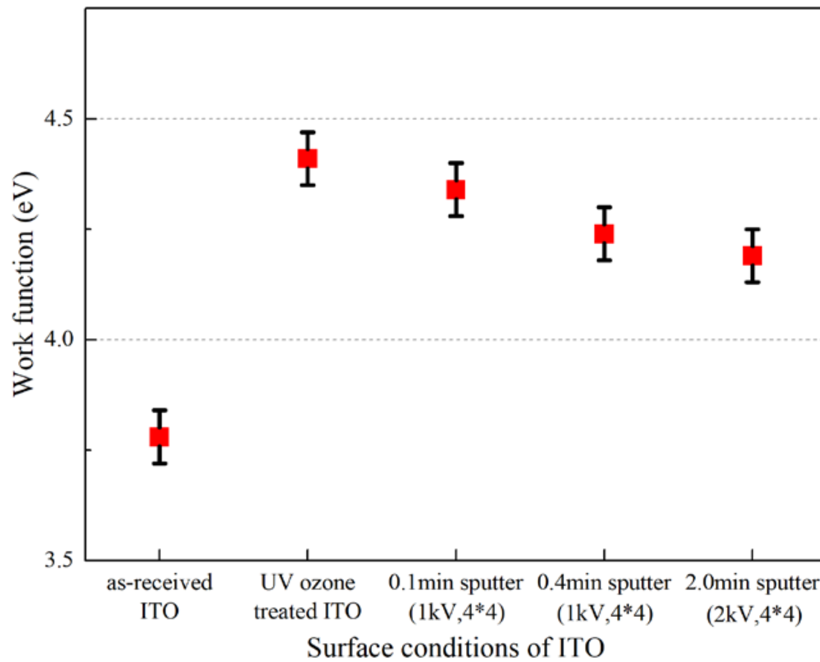

Figure 4.11 Work function of ITO with different surface treatments.

The measured work function is shown in Figure 4.11. The error bar is 0.06 eV which is determined by repeating measurements on a piece of Ar^+ sputter cleaned Au plate for many times. It can be considered as the total error including instrumental error and random error in the work function calculation. The lowest work function, which is 3.78 eV, is from the as-received ITO sample. The highest work function, which is 4.41 eV, is from the sample with 30 minutes

UV-ozone radiation. When Ar^+ sputtering is applied, the work function decreases with increased time of sputtering.

It is already known that surface carbon contaminant affects the work function of ITO significantly [30]. When UV-ozone radiation is applied on the ITO sample, the work function increases from 3.78 eV to 4.41 eV due to the removal of carbon-based contaminant. If the surface contaminant is the only factor affecting the work function, the work function of the ITO should be higher than 4.41eV when Ar^+ sputtering removes contaminant further. Figure 4.1 already demonstrates contaminant removal by Ar^+ sputtering. However, the work function of ITO starts decreasing after Ar^+ sputtering is applied. The work function decreases with increased sputter time. It indicates that surface carbon-based contaminant is not the only factor which affects work function of ITO.

In literature, the O/In and Sn/In ratios was concluded as two factors affecting work function of ITO [30][70]. In this study, the Sn3d and O1s spectra are analyzed in detail. Although the O/In and Sn/In ratios and the work function of ITO both decrease in the Ar^+ sputtering process, the work function change cannot be simply attributed to the O/In and Sn/In ratio change. From analysis of Sn3d and O1s spectra, one can conclude that Ar^+ sputtering reduces Sn^{4+} to Sn^{2+} in Sn-rich surface and removes Sn-rich surface gradually. The change of O/In and Sn/In ratios is attributed to the reduction of Sn^{4+} in the Sn-rich surface and the removal of Sn-rich surface. Thus, the factors affecting the work function of ITO is the change in the composition of Sn-rich surface, reduction of Sn charge state (Sn4+ to Sn2+) as well as oxygen loss.

For a SnO_2 sample, the surface oxygen vacancies induced the electronic states in the band gap. The conductivity of SnO_2 increased with the level of surface oxygen vacancies [60]. The

electronic states in the band gap rise the Fermi level. Thus, the work function of SnO_2 decreases with increased level of surface oxygen vacancies. For the ITO sample, the Sn-rich surface behaves like SnO_2 because similar electronic states can be found in Figure 4.6 and Figure 4.7. The Sn-rich surface was also reported as SnO_2-like [20]. The composition in the bulk of ITO is different from the Sn-rich surface. The work function of the bulk ITO and the Sn-rich surface is expected to be different. Since SnO_2 has high work function which is 4.7-5.7 eV depending on surface conditions [58], the Sn-rich surface is expected to have higher work function than ITO bulk. The surface work function of ITO should be controlled by the Sn-rich surface. The previous analysis demonstrates that the Ar^+ sputtering removes Sn-rich surface and reduces Sn^{4+} to Sn^{2+} simultaneously. The decreased amount of Sn-rich surface lowers the work function of ITO. Ar^+ sputtering produces oxygen vacancies on Sn-rich surface which lead to increase the surface conductivity and rise the surface Fermi level. As a result, the work function decreases after Ar^+ sputtering due to decreased Sn-rich surface and reduction of Sn^{4+} in the Sn-rich surface.

There are three factors affecting the work function of ITO: surface contaminant, the level of Sn^{2+} in Sn-rich surface, and the amount of Sn-rich surface. For the as-received ITO, carbon-based contaminant dominates the work function. After UV-ozone radiation, most carbon-based contaminants are removed, decreasing their influence. The Sn-rich surface is less prominent and the level of Sn^{2+} is lower. As a result, the processes ITO increases its work function. When Ar^+ sputtering is applied, the level of Sn^{2+} increases and the amount of Sn-rich surface decreases. Although the surface contaminant is further removed by Ar+ sputtering, the work function still exhibits decrease. The Sn-rich surface and the level of Sn^{2+} concentration in the Sn-rich surface dominate the work function of ITO when the level of surface contaminant is low.

4.4 Conclusion

This study demonstrates the impact of Ar^+ sputtering on the chemistry of Sn-rich surface of ITO and the correlation between the Sn-rich surface and the work function of ITO. The Ar^+ sputtering removes Sn-rich surface and reduces the oxidation state of Sn in the Sn-rich surface from Sn^{4+} to Sn^{2+} due to the oxygen preferential sputtering effect. This is the reason of reduced work function of ITO with Ar^+ sputter cleaning. The fully oxidized Sn-rich surface, in the form of SnO_2, is an essential factor that keeps the work function of clean ITO relatively high. When the level of surface contaminant of ITO is low, the amount of Sn-rich surface and the oxidations state of Sn in the surface region dominate the work function. The decreased amount of Sn-rich surface and the increased Sn^{2+} concentration in the Sn-rich surface will lower the work function of ITO.

CHAPTER 5

SURFACE CHEMISTRY AND WORK FUNCTION CHANGES OF RUO_2/ITO STUDIED BY XPS AND UPS

5.1 Introduction

Interfaces are critical and are a widely investigated topic due to their deterministic role they play in the performance of devices. Indium tin oxide thin (ITO), as a transparent conductive oxides (TCOs) materials widely used in thin film solar cells, photovoltaics, and LEDs. However, it still has drawbacks that affect the performances of ITO-based devices.

One of drawbacks is the poor surface chemical stability of ITO. When ITO is deposited on a non-oxide substrate or is used as a substrate, the oxygen ions from ITO can easily diffuse into an adjacent non-oxide material to form an ambiguous interface. For example, a Si oxide (SiO_x) layer forms at the Si/ITO interface when ITO is directly deposited on a Si substrate [1][71]. For Si-based thin film solar cell, one factor which makes ITO be used as the front contact is the high electrical conductivity of ITO, high optical transmittance and relatively high WF. However, the formed SiOx layer at the Si/ITO interface has low electrical conductivity which can lead to increased Ohmic losses at the front contact [72]. As a result, the efficiency of the Si-based solar cell decreases due to the oxygen diffusion at the interface. ITO is also widely used in organic-based solar cell and is known to exhibit some chemical instabilities. In the organic-based solar cells, the ITO films contact with the organic semiconductors. The oxygen ions from the ITO usually oxidize the organic semiconductor at the interface [73][74]. Furthermore, Li et al. reported that the cations, such as In^{3+} and Sn^{4+}, also diffused into the 2-amino-4,5-dicyanoimidazole (AIDCN) layer to form nanoparticles at the AIDCN/ITO interface

[75]. The formed nanoparticles lead to electrical switching behavior in the AIDCN/ITO structure [75].

Another drawback of ITO is the difficulty of maintaining high work function. If ITO is exposed in air, the carbon-based contaminant is easily absorbed on the surface of ITO. The surface carbon-based contaminant can reduce the work function of ITO greatly. As described in Chapter 4, the Sn-rich surface is another key factor which has significant influence on the work function of ITO. Reduced amount of the surface Sn content and reduction working on the Sn-rich surface will decrease the work function of ITO greatly. Although there are various techniques can be chosen to remove the surface contaminant, none of them can remove the contaminant completely without damaging the Sn-rich surface of ITO. As a result, it is difficult for ITO samples with surface contaminant to restore their high work functions.

Since the work function of ITO is controlled by surface conditions, the work function can be tuned by engineering the surface of ITO. The two issues of ITO, low chemical stability and reduced work function, can be solved by a simply solution: ultra-thin film coating. The coated film has two functions: acting as diffusion barrier, stabilizer and enhancing the work function of ITO. The film is required to possess high chemical stability, high electrical conductivity, and high work function. The film with high chemical stability can block the diffusion at ITO/semiconductor interface. The high electrical conductivity leads to the reduced contact resistivity which can decrease the Ohmic losses at the ITO/semiconductor heterojunction. High work function is an essential property for the coated film to enhance the work function of ITO.

Ruthenium di-oxide (RuO_2) is one of the proper materials which satisfy the three requirements mentioned above. RuO_2 exhibits metallic conductivity which is attributed to its partially filled Ru 4d states [76]. The bulk electrical resistivity of RuO_2 can be as low as to 40

μΩ·cm [77][78]. The work function of the RuO_2 is 5.0 eV, which is higher than that of the ITO [79][80][81]. The RuO_2 also exhibits good thermal and chemical stability. RuO_2 films have already been used as diffusion barriers in many studies and successfully blocked the diffusion at the interfaces of various materials [82][83][84]. For example, RuO_2 thin film was used as diffusion barrier for Si. Although a thin SiO_2 layer was formed at the RuO_2/Si interface when RuO_2 thin film was deposited on the surface of Si, the SiO_2 layer didn't grow up at high temperature (up to 700˚C) for long time (up to 6 hours) [85]. The RuO_2 thin film performed good thermal stability. The thickness of the formed SiO_2 layer at the interface was only 3 nm [85]. It was thin enough for electron tunneling. The low contact resistivity of RuO_2/Si was also reported in other literatures [86][87].

The diffusion barrier function of RuO_2 is already proved. In this study, RuO_2 ultra-thin films are deposited on the ITOs by DC magnetron sputtering. The work function of RuO_2/ITO samples are evaluated by the UPS. Additionally, the chemical bonding at the RuO_2/ITO interface is investigated by the XPS measurement. The surface contaminant is removed by UV-ozone radiation and Ar^+ sputtering. Moreover, the Ar^+ sputtering is also used to modify the deposited RuO_2 ultra-thin films during the XPS and UPS measurements. Since Ar^+ sputtering affects the surface chemical bonding of ITO and leads to the decreased work function, the chemical bonding and the work function of RuO_2/ITO are also expected to be changed by Ar+ sputtering and are investigated by XPS and UPS. The correlation between the chemical bonding and the work function is discussed.

5.2 Experimental

RuO_2 ultra-thin films are deposited on commercial ITO/glass substrates purchased from

Luminescence Technology Corp via DC magnetron sputtering. Before deposition, the ITO substrates are pre-treated by UV-ozone radiation for 5 minutes to remove surface carbon-based contaminant. The distance from the UV lamp to the surface of substrates is less than 1 centimeter. After UV-ozone treatment, the substrates are loaded into the DC magnetron sputtering deposition chamber immediately. In the DC magnetron sputtering process, the target material is pure Ru. The deposition takes place in the mixture flow of argon and oxygen gases at room temperature. The base pressure and the working pressure are 10^{-8} torr and 5 millitorr. The gun power is 50 W. Different deposition times, 1 and 2 minutes, are set to prepare RuO_2 ultra-thin films with different thicknesses.

PHI 5000 XPS system is employed to perform the XPS and UPS measurements. Because the prepared RuO_2/ITO samples are exposed in air, 30 minutes UV-ozone radiation is applied on the samples before introduced into XPS analysis chamber to remove part of surface contaminant. The distance from the UV lamp to the surfaces of the samples is 10 centimeters. The radiation takes place in air at room temperature. The treated samples are transferred into the XPS analysis chamber immediately to prevent re-contamination. The samples are loaded on the sample stage with good grounding. The background pressure in the analysis chamber is 10^{-6} Pa. The X-ray source is the Al K alpha radiation. The energy is 1486.6 eV. The XPS spectra are recorded with 11.75 eV pass energy and 0.1 eV energy step. The ultraviolet source is the He I source with the energy 21.22 eV. A -9 Volts bias voltage is applied on the sample stage during the UPS measurement to separate secondary edges of RuO_2/ITO samples from that of the analyzer and increase the intensity of the secondary edge. The pass energy and the energy step for the recording of the UPS spectra are 2.950 eV and 0.005 eV, respectively. The XPS and UPS system

is calibrated by sputtering cleaned Au and Ag foil. The Ar^+ sputtering is employed during the XPS and UPS measurements.

5.3 Result and Discussion

5.3.1 Surface Carbon-Based Contaminant Removal by UV-Ozone Radiation and Ar^+ Sputtering

The prepared RuO_2/ITO samples are exposed in air during transfer to XPS and UPS measurement. Contaminants such as hydrate and carbonate are likely absorbed on the surfaces. The level of surface carbon-based contaminant is usually expressed by the intensity of C1s core-level XPS peak. For the RuO_2/ITO sample, the C1s spectrum overlaps with the Ru3d spectrum. The Ru3d spectrum consists with two spin-orbital splitting peaks: $Ru3d_{5/2}$ and $Ru3d_{3/2}$. The two peaks have the energy distance 4.2 eV and are well separated in the Ru3d spectrum of Ru metal. The intensity ratio of $Ru3d_{5/2}$ to $Ru3d_{3/2}$ is a constant 1.5. Since the peak width of C1s is much smaller than the region of Ru3d spectrum, C1s peak only partially overlaps with the Ru3d spectrum. The C1s or Ru3d spectrum still provides information about the level of surface carbon-based contaminant. In this study, the Ru3d spectra are collected to roughly express the level of surface carbon-based contaminant.

To decrease the level of surface carbon-based contaminant, UV-ozone radiation is applied on the RuO_2/ITO samples. The efficiency of the UV-ozone radiation for contaminant removal is unknown. To check the efficiency, the RuO_2/ITO samples are exposed in the UV-ozone radiation for 0, 15, 30, and 45 minutes. The Ru3d spectra of the 1-minute deposited RuO_2/ITO sample before and after UV-ozone radiation are displayed in Figure 5.1.

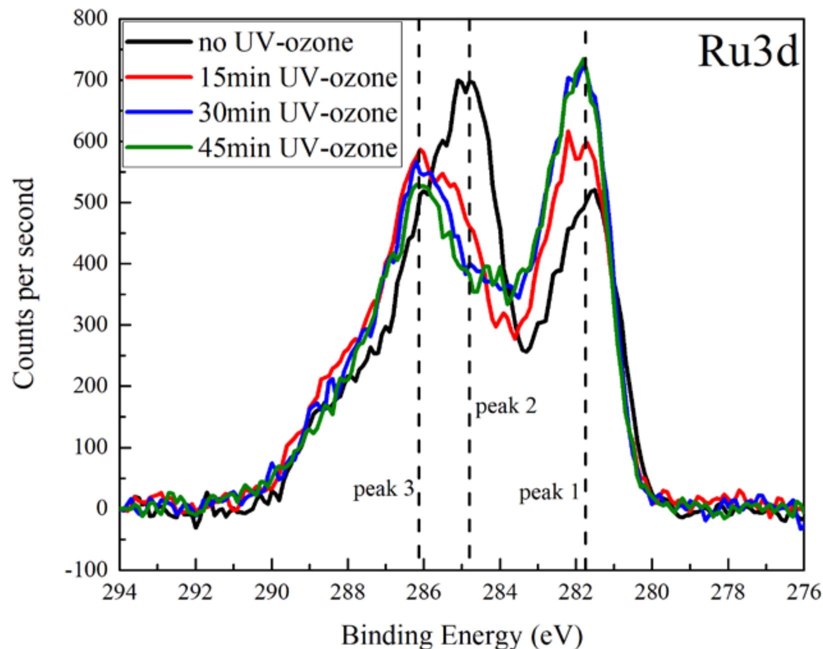

Figure 5.1 Ru3d spectra of the 1-minute deposited RuO_2/ITO sample treated by UV-ozone radiation for different exposure time.

The Ru3d spectrum of the RuO_2/ITO sample without UV-ozone radiation treatment shows two main peaks which are labeled as peak 1 and peak 2 in Figure 5.1. According to the energy region of $Ru3d_{5/2}$ peak in XPS handbook [65], the peak 1 is assigned to $Ru3d_{5/2}$ peak. The positions of the peaks are roughly determined by the maximum points of the peaks in Figure 5.1. The peak 2 has much higher intensity than the peak 1. The energy distance between the peak 1 and peak 2 is only 3.3 eV which is less than 4.2 eV. The peak 2 is at 284.8 eV which equals the binding energy of C1s peak of Carbon. The higher intensity and the shorter energy separation of the peak 2 indicates that the C1s peak dominates the peak 2. the $Ru3d_{3/2}$ peak is screened by C1s peak and cannot be seen directly from the Ru3d spectrum because of the high level of carbon contaminant on the surface of 1-minute deposited RuO_2/ITO sample.

After 15 minutes UV-ozone radiation, the peak at left side of the peak 1 shifts to higher

binding energy side. It is labeled as peak 3. The energy distance between the peak 1 and peak 3 equals 4.2 eV. Thus, the peak 3 can be assigned as $Ru3d_{3/2}$ peak. From 0 to 30 minutes UV-ozone radiation, the intensity of peak 3 decreases and the intensity of peak 1 increases as a function of increased exposure time of UV-ozone radiation. Although the peak areas of the peak 1 and peak 3 cannot be calculated directly, it is sure that the ratio of the two peaks is approaching the constant ratio 1.5. The change of the intensities must be result from the removal of surface carbon-based contaminant. When the level of surface carbon-based contaminant decreases, the intensity of C1s decreases. Meanwhile, the intensities of $Ru3d_{5/2}$ and $Ru3d_{3/2}$ increase. In the overlapped part of Ru3d spectrum, the weighted percentage of $Ru3d_{3/2}$ increases. The increased weighted percentage makes the overlapped part shift to higher binding energy side.

If comparing the Ru3d spectra of the sample with 30 and 45 minutes UV-ozone radiation, one can find that the two spectra have identical line-shape and intensity. The identical spectra can result from two possible reasons. The first reason is that the surface carbon-based contaminant is removed completely by 30-minute UV-ozone radiation. The second reason is that 30 minutes UV-ozone radiation treatment reaches the capability of the surface carbon-based contaminant removal of UV-ozone radiation. Although the contaminant remains on the surface, the UV-ozone radiation cannot remove it any more.

To prove if the surface carbon-based contaminant is removed completely by the UV-ozone radiation, the low energy Ar^+ sputtering is applied on the 45-minute treated 1-minute deposited RuO_2/ITO sample. The kinetic energy of Ar^+ sputtering is 1 keV. The sputter time is 0.2 minutes. The Ru3d spectra of 1-minute deposited RuO_2/ITO sample before and after Ar^+ sputtering are compared in Figure 5.2. The Ru3d spectrum of the sample after sputtering shows two main peaks. The whole spectrum shifts to lower binding energy side. The intensities of both

peaks increase after sputtering. The binding energy of the peak, if the peak is considered as the peak containing single component, is measured at the maximum point of the peak. The intensity is defined as the height of the peak. The energy distance between the two peaks is 4.2 eV, and the ratio of the intensities is 1.55 which is close to 1.5. As a result, the two main peaks are $Ru3d_{5/2}$ and $Ru3d_{3/2}$ with high possibility. The increased intensity of Ru3d peak proves that the surface carbon-based contaminant is further removed by Ar^+ sputtering. In another word, the UV-ozone radiation is not capable to remove the contaminant completely. The 30-minute exposure just reaches the capability of UV-ozone radiation for the surface carbon-based contaminant removal. The peak shift is already observed in Figure 5.2. More peak shift will be shown later. To determine the real binding energy of each peak, the energy calibration is necessary.

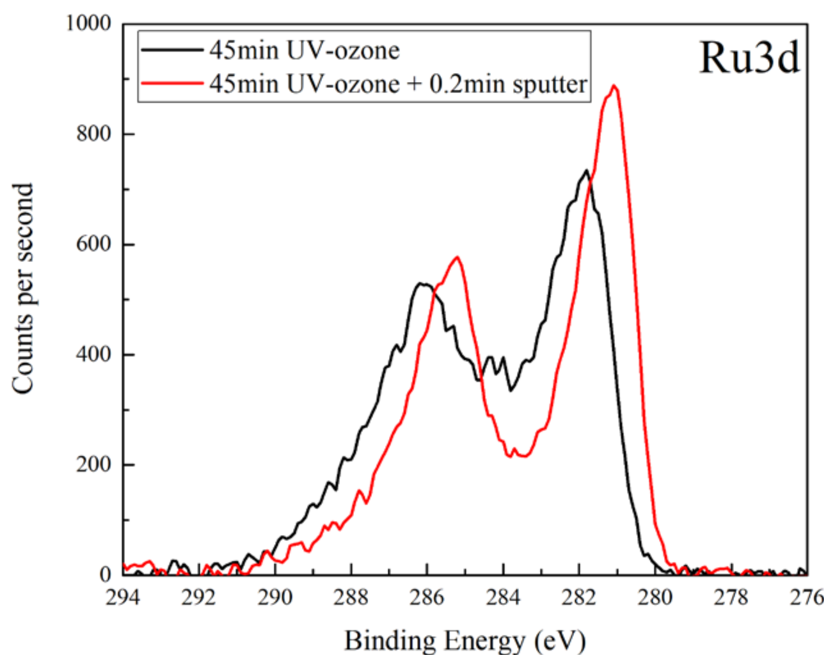

Figure 5.2 The comparison of Ru3d of 1-minute deposited RuO_2/ITO before and after Ar^+ sputtering.

5.3.2 Energy Calibration

In a XPS spectrum, the zero point is defined at the position of the Fermi level. The XPS system is usually calibrated by measuring the pure metals, such as sputter cleaned Au, Ag, and Cu because such metals have the Fermi edge shown in XPS spectra. The Fermi edge can be considered as the best energy reference for energy calibration. In Chapter 4, we known that ITO samples don't have the Fermi edge in the valence band spectra. The energy calibration cannot be done for ITO by using the Fermi edge. In this study, the RuO_2 ultra-thin film is deposited on ITO substrate. As a metallic-like conductor, RuO_2 shows the Fermi edge in XPS spectra [88]. It is possible to use the Fermi edge as the energy reference in this study. The valence band XPS spectra of 1-minute deposited and 2-minute deposited RuO_2/ITO are displayed in Figure 5.3. All of samples are pre-treated by 30 minutes UV-ozone radiation. Then the Ar^+ sputtering with kinetic energy 1 keV is applied on the samples. The number labeled in Figure 5.3 represent the sputter time.

The valence band XPS spectra of ITO are already shown in Chapter 4. If comparing the valence band of ITO with the valence band of RuO_2/ITO, we can find an extra peak in the region 0 to 3 eV. Riga et al. described the composition of the valence band of RuO_2 [88]: The valence band of the RuO_2 contains three components. The hybridization of the O2p and Ru4d states forms σ, π, π* and σ* four types of molecular orbitals. Three of them, σ, π, and π*, are filled by electrons. In the XPS spectrum, signal electrons from σ and π molecular orbitals depict a valence band between 2 to 10 eV. The peak between 0.0 and 2.0 eV derives from the electrons in the π* molecular orbitals. The valence band maximum is at 0.0 eV [88].

In Figure 5.3, the valence band of the RuO_2/ITO sample is the combination of the valence bands of ITO and RuO_2. The valence band of ITO is only in the region from 3 to 10 eV. When

the valence band of RuO_2 overlaps the valence band of ITO, the peak of RuO_2 only in the region from 0.0 to 3.0 eV can be observed directly. Since the valence band maximum of the RuO_2 sample is at 0.0 eV [88], the valence band maximum of the RuO_2/ITO sample can be used as energy reference. The valence band maximum is determined by the cross section of the linear extrapolation of the valence band leading edge to the background line. All valence band spectra show that the valence band maximum is at the Fermi level. There is no shift for XPS spectra.

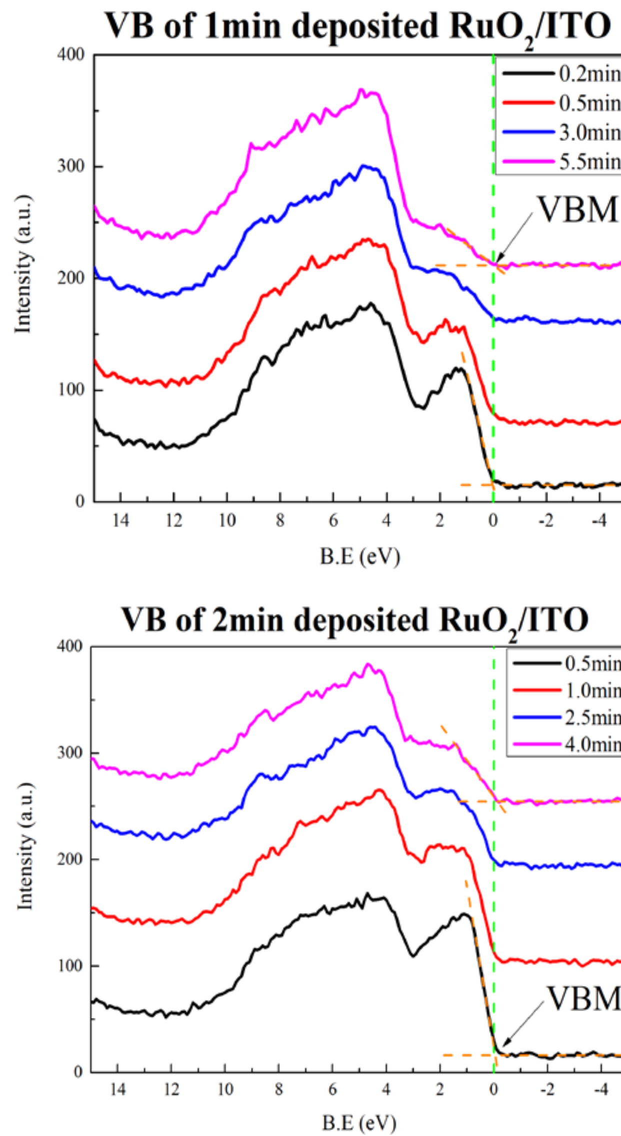

Figure 5.3 Valence band XPS spectra of RuO_2/ITO samples treated by various sputter time. Samples are pre-treated by 30 minutes UV-ozone radiation.

Since the peak between 0.0 and 3.0 eV only belongs to the deposited RuO_2, the intensity of this peak represents the amount of the deposited RuO_2. Because the intensities of the peaks decrease with increased sputter time, it is obvious that the Ar^+ sputtering removes RuO_2 as a function of increased sputter time.

5.3.3 Core-Level Peak Shift Caused by RuO_2 Deposition

Energy calibration is done by measuring the valence band of the RuO_2/ITO sample. One can conclude that the peak shift in Figure 5.2 is not caused by the surface charge. There must be other reasons leading to the peak shift. From Figure 5.3 we know that the Ar^+ sputtering removes part of deposited RuO_2 from surface of the RuO_2/ITO samples. It is reasonable to assume that the peak shift correlates with RuO_2 on the surface.

The In3d, O1s, Sn3d, and Ru3d core-level XPS spectra are collected from the 1-minute deposited and 2-minute deposited RuO_2/ITO samples. The samples are pre-treated by 30 minutes UV-ozone radiation. These core-level spectra are compared with the spectra of ITO which is also treated by 30 minutes UV-ozone radiation in Figure 5.4. The background of the spectra is removed by Shirley function.

The Ru3d peaks are displayed in Figure 5.4 (a). There is no peak shift between two spectra. The Ru3d peak of 2-minute deposited RuO_2/ITO sample has higher intensity which means thicker deposited RuO_2 layer. The In3d, Sn3d, and O1s peaks show the peak shift to lower binding energy side after RuO_2 deposition in Figure 5.4 (b), (c), and (d). The spectra of the 2-minute deposited sample show the longer shift distances than the spectra of the 1-minute deposited sample.

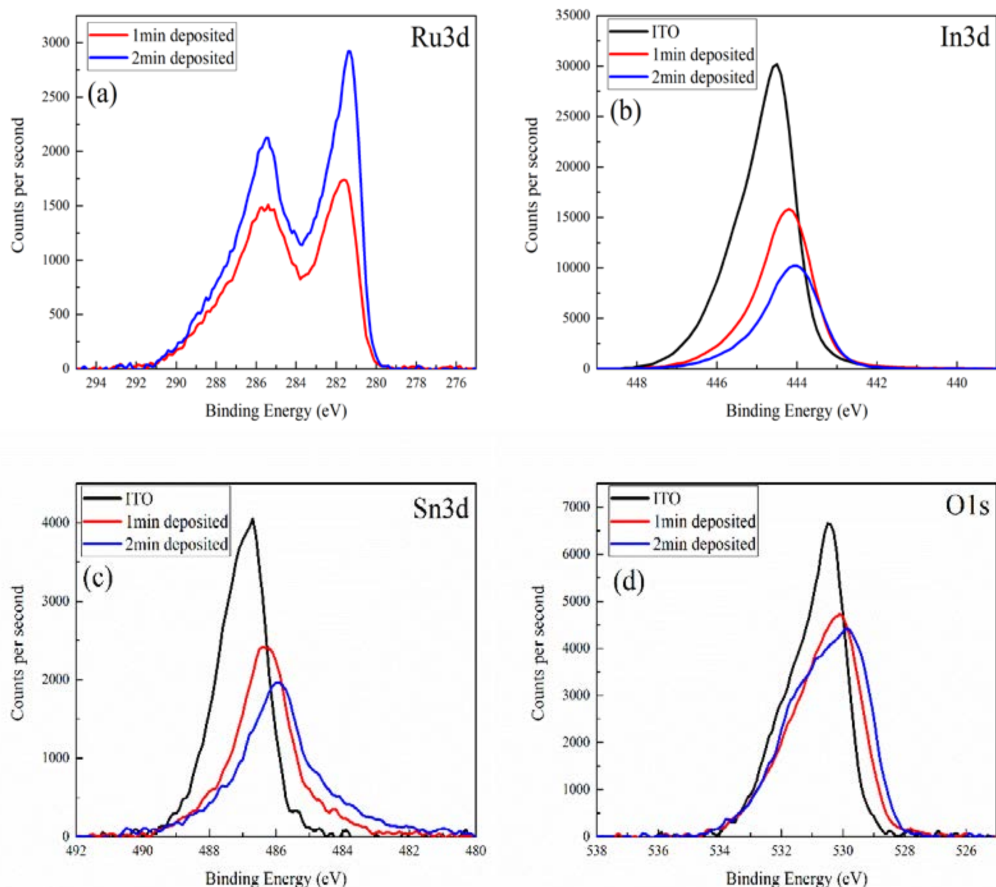

Figure 5.4 Core-level XPS spectra of ITO, 1-minute deposited RuO_2/ITO, and 2-minute deposited RuO_2/ITO, three samples received 30 minutes UV-ozone radiation.

The details of peak fitting on In3d and Sn3d peaks are already elucidated in Chapter 4. Here the same method of peak fitting is applied on the In3d and Sn3d core-level spectra of the RuO_2/ITO samples. The peak fitting results are shown in Figure 5.5.

Figure 5.5 (a) and (c) are the peak fitting results of the In3d peaks of the 1-minute deposited and 2-minute deposited RuO_2/ITO samples, respectively. Due to the simple components of In3d peaks, the In3d peak is used as the energy reference to justify the shift distance of Sn3d peaks. The screened $In3d_{5/2}$ peaks are at 444.33 eV and 444.14 eV in Figure 5.5 (a) and (c), respectively.

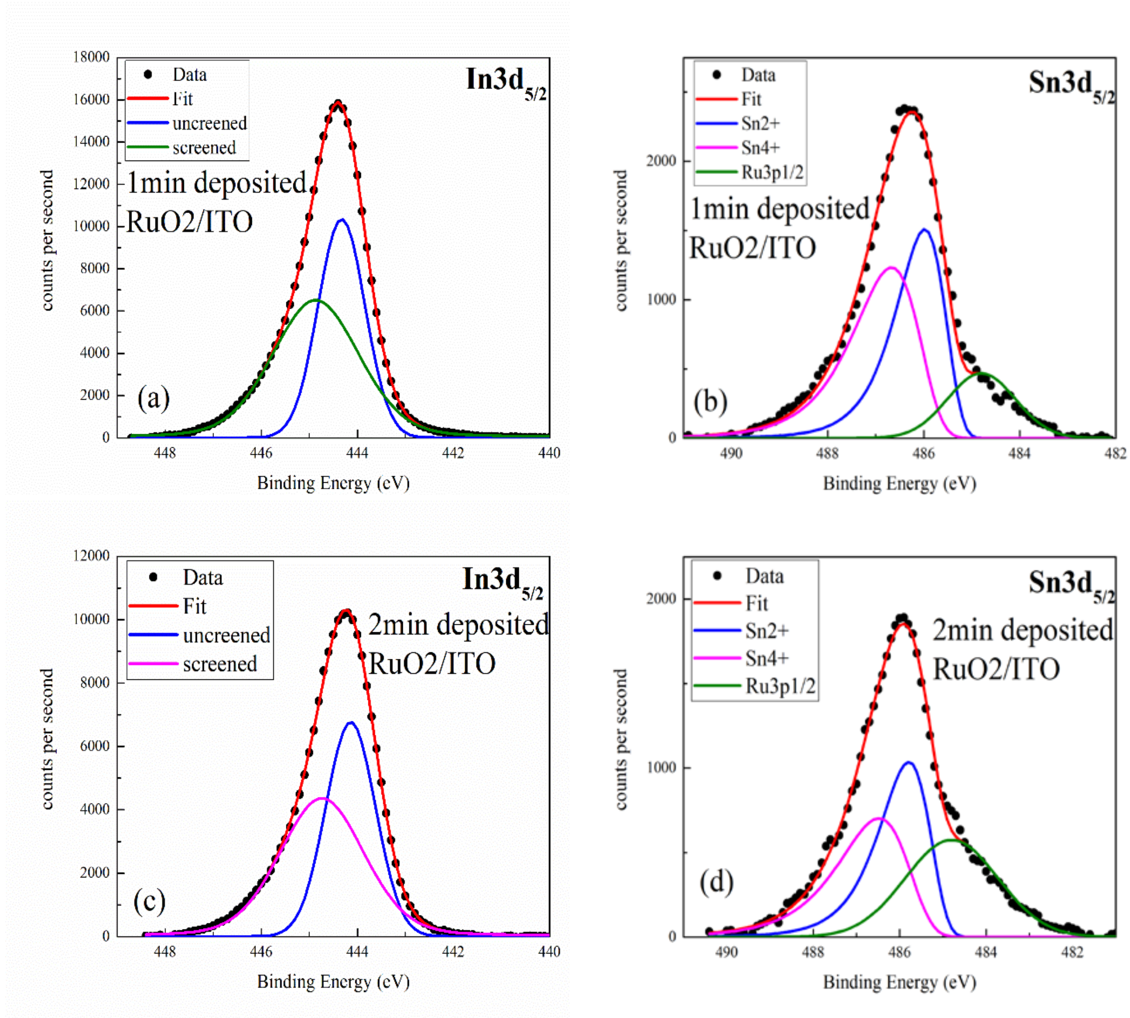

Figure 5.5 Peak fitting on $In3d_{5/2}$ and $Sn3d_{5/2}$ peaks

In the peak fitting process of Sn3d peaks, the energy distance between the screened $In3d_{5/2}$ peak to $Sn3d_{5/2}$ peak of Sn^{4+} must be a constant. The energy distance between two of three components Sn^{4+}, Sn^{2+}, and Sn^{0} also keeps a constant. These energy distances are obtained from the peak fitting results of In3d and Sn3d peaks of the ITO samples. The peak fitting results of the Sn3d spectra of the 1-minute deposited and 2-minute deposited RuO_2/ITO samples are displayed in Figure 5.5 (b) and (d), respectively. If carefully checking the line-shape of Sn3d peaks in Figure 5.4 (c), one will discover the differences among the Sn3d peaks from three samples. The $Sn3d_{5/2}$ peak of RuO_2/ITO sample has a tail at lower binding energy side which doesn't appear in

Sn3d peak of ITO. The intensity of the tail has higher intensity for the 2-minute deposited RuO_2/ITO sample. This tail is the $Ru3p_{1/2}$ peak according to the binding energy [65][89][90]. The $Sn3d_{5/2}$ peak of the RuO_2/ITO sample is fitted by three peaks which are different from the three peaks in $Sn3d_{5/2}$ peak of the ITO sample. The peaks of Sn^{4+} and Sn^{2+} are retained. The peak of Sn^0 is removed, and the peak of $Ru3p_{1/2}$ is added. The $Sn3d_{5/2}$ peak of Sn^0 overlaps the $Ru3p_{1/2}$ peak. According to the peak fitting results in Chapter 4, the intensity of the $Sn3d_{5/2}$ peak of Sn^0 is always low. The relative peak area is only about 4%. In this case, the $Sn3d_{5/2}$ peak of Sn^0 is omitted to reduce the parameters in the peak fitting process. The $Ru3p_{1/2}$ peak is created by Gaussian function. The peak fitting result shows that binding energy of $Ru3p_{1/2}$ peak is 484.80 eV. The value of the binding energy is justified by $Ru3p_{3/2}$ peak. The Handbook of X-ray Photoelectron Spectroscopy provides a rough value of the energy distance between $Ru3p_{3/2}$ and $Ru3p_{1/2}$: 22 eV [65]. For the RuO_2/ITO sample, the $Ru3p_{3/2}$ peak doesn't overlap any other peaks. The $Ru3p_{3/2}$ peak is collected at the same time, but is not shown here. The measured binding energy of $Ru3p_{3/2}$ is 462.9 eV. The energy distance from 462.9 eV to 484.80 eV is 21.9 eV. Thus, the binding energy of $Ru3p_{1/2}$ provided by peak fitting is reliable.

The peak fitting results show the components of Sn^{2+} and Sn^{4+} in the ITO samples and the RuO_2/ITO samples. The intensity ratio of Sn^{2+}/Sn^{4+} increases significantly after RuO_2 deposition. The ratios of Sn^{2+}/Sn^{4+} for 1-minute deposited and 2-minute deposited RuO_2/ITO sample are 90.7% and 100.7%, respectively. These values are much larger than the ratio of UV-ozone treated ITO which is 26.0%. There are two hypothetical explanations for the high ratios. The first explanation is that the deposited RuO_2 layer screens the signal electrons from the bulk of ITO. In Chapter 4, we already conclude that Sn^{2+} ions are only on the surface of ITO. In the bulk of ITO, the Sn ions exist as Sn^{4+}. That deposited RuO_2 and surface contaminant screen part

of signal electrons from Sn^{4+} in the bulk leads to the decreased intensity of the Sn3d peak of Sn^{4+}. Consequently, the ratio of Sn^{2+}/Sn^{4+} increases. The second explanation is the reduction of the surface Sn^{4+} ions caused by RuO_2 deposition. The deposited Ru atoms may land on the ITO substrate and take oxygen from Sn^{4+} ions in the Sn-rich surface instead of binding with oxygen from atmosphere. The oxidation state of Sn^{4+} is reduced to Sn^{2+}. In this case, the RuO_2 deposition produces high level of Sn^{2+} on the surface of the ITO substrate. The increased concentration of Sn^{2+} leads to the high ratio of Sn^{2+}/Sn^{4+}. In sum, the high ratio of Sn^{2+}/Sn^{4+} may result from decreased concentration of Sn^{4+} or increased concentration of Sn^{2+}. So far, one cannot figure out which explanation is correct. This question will be discussed further in the following content.

5.3.4 Peak Shift Caused by Ar^+ Sputtering

The peak shift of Ru3d after Ar^+ sputtering is already displayed in Figure 5.2. The In3d, Sn3d, O1s, and Ru3d spectra of the RuO_2/ITO with different sputter time are collected to investigate the correlation between the peak shift and the Ar+ sputtering. The kinetic energy of Ar^+ sputtering is 1 keV. The core-level XPS spectra of 1-minute deposited sample with different sputter time is shown in Figure 5.6, and the spectra of 2-minute deposited sample with different sputter time is shown in Figure 5.7. The In3d, Sn3d, and O1s peaks shift to higher binding energy side as a function of increased sputter time in Figure 5.6 and Figure 5.7. The explanation for the peak shift of In3d, Sn3d, and O1s in Figure 5.4 can be used to explain the shift of these three peaks in Figure 5.6 and Figure 5.7. In Figure 5.4, the In3d, Sn3d, and O1s peak of the 2-minute deposited sample shift longer distance to lower binding energy side because of the thicker RuO_2 layer.

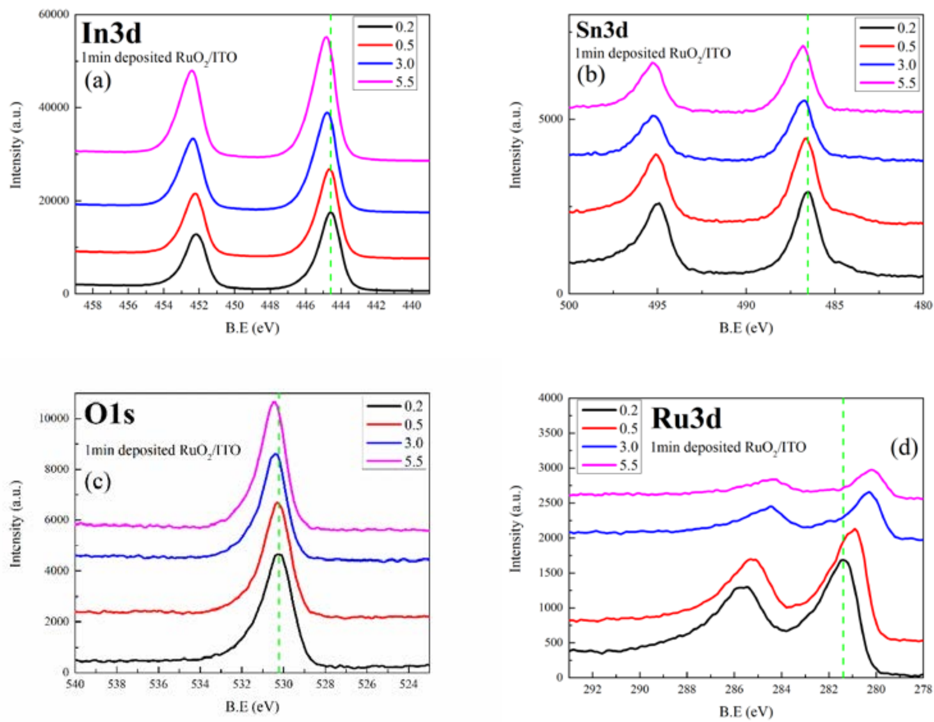

Figure 5.6 Core-level spectra of 1-minute deposited RuO_2/ITO received various sputter time.

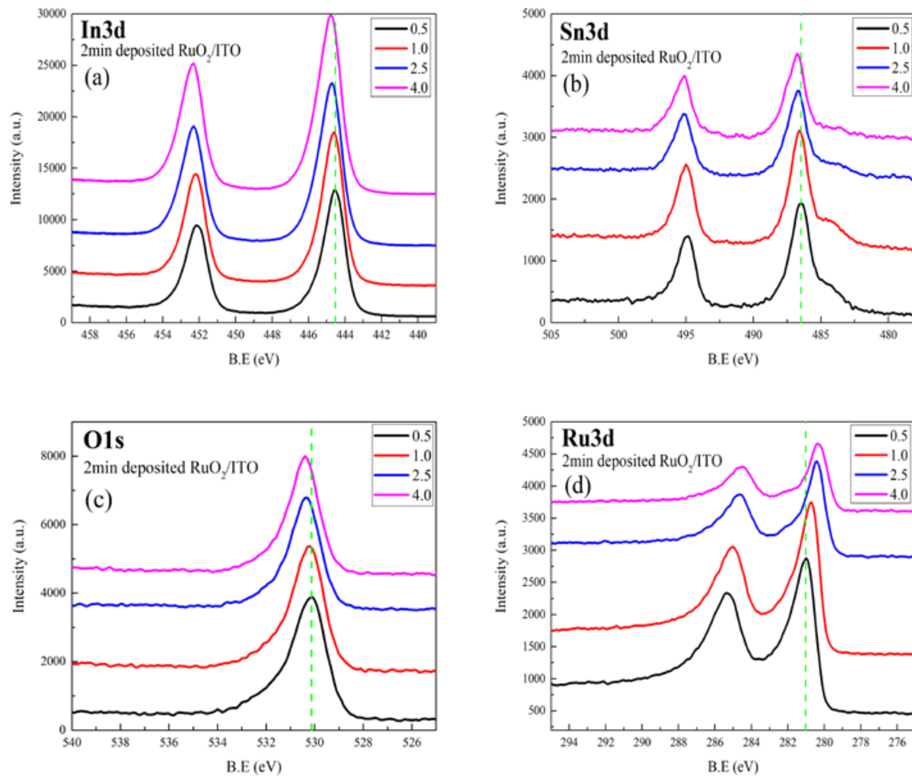

Figure 5.7 Core-level spectra of 2-minute deposited RuO_2/ITO received various sputter time.

In Figures 5.6 and 5.7, the Ar^+ sputtering removes part of deposited RuO_2 from the surface of the samples. The amount of removed RuO_2 depends on the sputter time. Longer sputter time means more removed RuO_2. The change of the level of the deposited RuO_2 is reflected in the change of the intensities of In3d peaks. Indium is only in the bulk of ITO. When surface RuO_2 is removed, the intensity of In3d will increase. In Figures 5.6 (a) and 5.7 (a), the intensities of In3d peaks increase with increased sputter time. The In3d peak with higher intensity shifts longer distance to higher binding energy side. The Sn3d (Figures 5.6 (b) and 5.7 (b)) and O1s (Figures 5.6 (c) and 5.7 (c)) peaks also shift with the In3d peaks. The shift direction and distances of Sn3d and O1s peaks keep identical with that of the respective In3d peaks. The indium, tin, and main oxygen are all from the ITO substrate. The same shift direction and distance strongly indicate that the shift is due to the band bending at RuO_2/ITO interface [62].

The Ru3d peak in Figure 5.4 doesn't shift. However, the Ru3d peaks shift to lower binding energy side after Ar^+ sputtering in Figures 5.6 and 5.7. It is obvious that the shift correlates with the Ar^+ sputtering.

5.3.5 Effect of Ar^+ Sputtering on Surface Sn Ions

5.3.5.1 Intensity of Sn3d Change with Ar^+ Sputtering

Indium and tin are both from the ITO substrate. When the top RuO_2 is removed, the intensities of In3d and Sn3d should both increase. However, in Figures 5.6 and 5.7, the Sn3d peaks show the decreased intensities after the top RuO_2 is gradually removed by Ar^+ sputtering. The intensity of a peak is defined as the peak area of the peak without background. The background of the peak is removed by the Shirley function. In Figure 5.6, from 0.2 to 5.5 minutes of sputtering, the peak area of $In3d_{5/2}$ peak increases from 27555 to 45497. Because

$Sn3d_{5/2}$ peak overlaps $Ru3p_{1/2}$ peak, the intensity of $Sn3d_{3/2}$ peak is measured to investigate the intensity change of Sn. From 0.2 to 0.5 minutes of sputtering, the intensity of $Sn3d_{3/2}$ peak increases from 3975 to 4200. The increase of the intensity indicates that surface contaminant is further removed after 0.5 minutes sputtering. From 0.5 to 5.5 minutes of sputtering, the intensity of $Sn3d_{3/2}$ peak decreases to 2568. For the 2-minute deposited RuO_2/ITO sample, the same trend of the change of intensities is found in Figure 5.7. From 0.5 to 4.0 minutes of sputtering, the intensity of $In3d_{5/2}$ peak increases from 19616 to 29823 while the intensity of $Sn3d_{3/2}$ peak decreases from 2124 to 1701. The decreased intensity of the $Sn3d_{3/2}$ peak of the RuO_2/ITO samples as a function of increased sputter time indicates that Sn is removed with RuO_2 by Ar^+ sputtering simultaneously. In this case, the Sn and Ru must be both in the top surface region of the RuO_2/ITO sample. The hypothetical structure of the RuO_2/ITO sample is the mixture of RuO_2 and the Sn-rich surface on the surface of the bulk ITO.

The intensities of $Sn3d_{3/2}$ peaks in Figures 5.6 and 5.7 are compared with the intensities of $Sn3d_{3/2}$ peaks of the ITO samples to provide more information about the surface structure of the RuO_2/ITO samples. Because the RuO_2/ITO XPS data are collected more than one year later than ITO XPS data, the standard intensity varies for the XPS data. To make the data comparable, the intensity ratio $Sn3d_{3/2}/In3d_{5/2}$ is used instead of the peak area of $Sn3d_{3/2}$ peak. The intensity ratio $Sn3d_{3/2}/In3d_{5/2}$ of ITO with 30 minutes UV-ozone radiation is 10.46%. After 2 keV Ar^+ sputtering for some certain minutes on ITO samples, the ratio stays at 5% to 6%, e.g., the intensity ratios for 1.5-minute sputtered and 2.0-minute sputtered ITO samples are 5.79% and 5.76%. These ratios can be considered as the ratio of the bulk ITO because the Sn-rich surface is already removed by Ar^+ sputtering. The intensity ratios $Sn3d_{3/2}/In3d_{5/2}$ of 1-minute deposited RuO_2/ITO sample versus sputter time is plotted in Figure 5.8 (a).

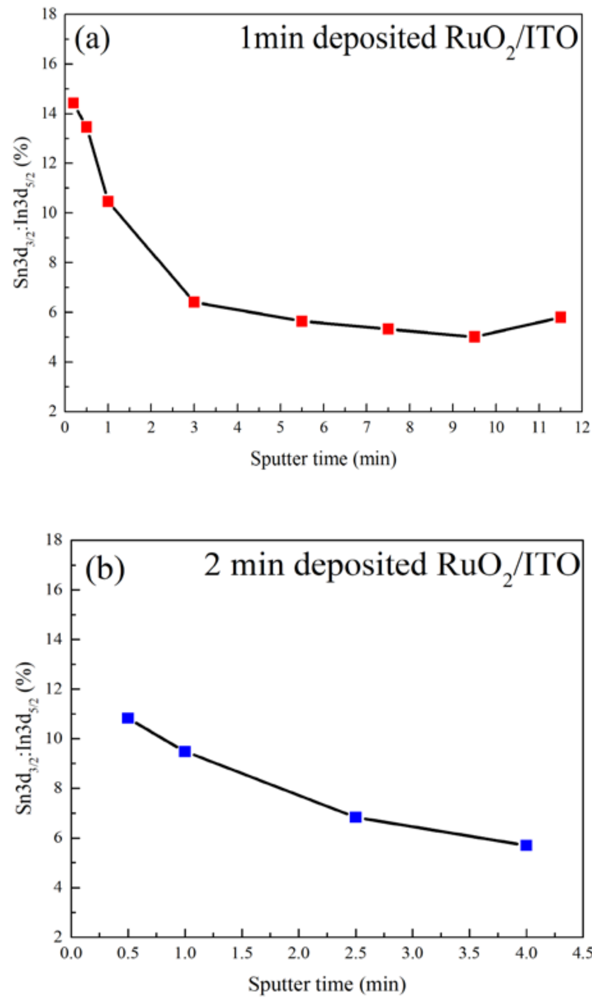

Figure 5.8 Ratio of $Sn3d_{3/2}$ to $In3d_{5/2}$ changes as a function of increased sputter time.

The kinetic energy of Ar^+ sputtering is 1 keV. The intensity ratios at 0.2 and 0.5 minutes is much higher than 10.46% which is the intensity ratio of ITO with 30 minutes UV-ozone radiation. The high intensity ratio results from the decreased intensity of $In3d_{5/2}$. The deposited RuO_2 screens the signal electrons from the bulk indium ions. Although the signal electrons from the bulk Sn ions also can be screened, the concentration of Sn in bulk is lower than the concentration on the Sn-rich surface. In this case, the intensity ratio becomes higher for the RuO_2/ITO sample. After 3.0 minutes sputtering, the intensity ratio $Sn3d_{3/2}/In3d_{5/2}$ decreases and fluctuates between 5% and 6%. For example, the intensity ratios for the 1-minute deposited

RuO_2/ITO sample with 5.5, 7.5, 9.5, and 11.5 minutes sputtering are 5.52%, 5.41%, 5.43%, and 5.82%, respectively. These ratios are close to the ratio of the bulk ITO. The intensity ratios of the 2-minute deposited RuO_2/ITO sample versus sputter time is plotted in Figure 5.8 (b). The kinetic energy of the Ar^+ sputtering is 1 keV. After 4.0 minutes sputtering, the intensity ratio of $Sn3d_{3/2}/In3d_{5/2}$ for 2-minute deposited RuO_2/ITO sample also drops to 5.70%. If paying attention on the Ru3d spectra in Figure 5.6 (d) and Figure 5.7 (d), one will find that Ru content is still detectable for XPS when 5.5 minutes sputtering is applied on the 1-min deposited sample and 4.0 minutes sputtering on the 2-minute deposited sample. The remaining Ru3d peaks proves that the removed Sn is on the top of the remaining RuO_2. It provides another evidence for the hypothetical structure: the mixture of RuO_2 and the Sn-rich surface on the surface of ITO.

Accordint to the Hume-Rothery rules, SnO_2 and RuO_2 can form unlimited solid solution. The RuO_2-SnO2 system satisfys all the substitutional solid solution rules of the Hume-Rothery rules [91]. The Sn and Ru has the same valency in the solution. The Ru^{4+} and Sn^{4+} have the similar atomic radius and electronegativities. The radius of Ru^{4+} is 0.69 Å, and the radius of Sn^{4+} is 0.71 Å [91]. The electronegativities of Ru and Sn are 1.9 and 1.73, respectively. However, some studies pointed out that the stable solid solution only exists at the specific Sn/Ru ratios and phase separation was observed in the Ru-Sn-O ternary oxide system [91][92][93]. In this study, the change of intensities of Sn3d peaks only indicates the mixture of RuO_2 and the Sn-rich surface. The crystal structure of the mixture is unknown. Thus, the mixture on the surface is named as the Ru-Sn-O ternary oxide system.

5.3.5.2 Component Change of Sn3d Peaks after Ar^+ Sputtering

The peak fitting result in Figure 5.5 reveals the high Sn^{2+}/Sn^{4+} ratio for the UV-ozone

treated RuO_2/ITO samples. Two possible reasons which lead to the high Sn^{2+}/Sn^{4+} ratio are promoted. The Sn^{2+}/Sn^{4+} ratio of the RuO_2/ITO samples with different sputter time are plotted to provide more clues about the reason of the high Sn^{2+}/Sn^{4+} ratio. The peak fitting process is done on the Sn3d spectra shown in Figure 5.6 and Figure 5.7. The intensity ratio of Sn^{2+}/Sn^{4+} versus sputter time is plotted in Figure 5.9.

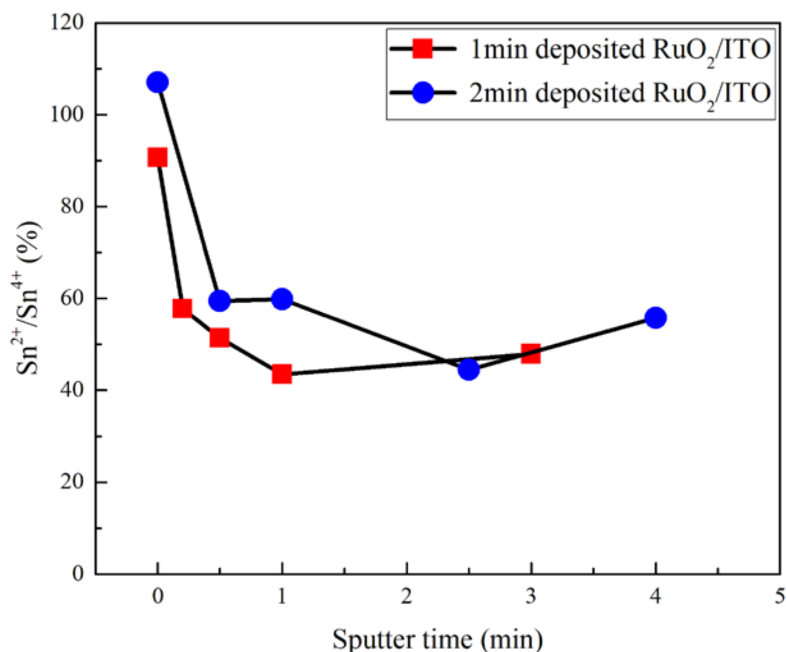

Figure 5.9 Intensity ratio of Sn^{2+}/Sn^{4+} changes as a function of sputter time.

Before Ar^+ sputtering, the intensity ratio of Sn^{2+}/Sn^{4+} for 1-minute deposited and 2-minute deposited samples are 90.7% and 100.7%, respectively. Figure 5.4 (d) shows that the Ru3d peaks of the two RuO_2/ITO samples have the similar line-shape. The amount of deposited RuO_2 can be approximated by the height of the $Ru3d_{5/2}$ peaks. The heights of the $Ru3d_{5/2}$ peaks for 1-minute deposited and 2-minute deposited samples are 1741 and 2930, respectively. The height for the 2-minute deposited sample is 1.7 times of the height for the 1-minute deposited samples. If the high ratio of Sn/In in Figure 5.8 is only caused by the screening of deposited

RuO_2, the ratio of Sn^{2+}/Sn^{4+} for the 2-minute deposited sample should be much larger than the ratio for the 1-minute deposited sample. Actually, the ratios of Sn^{2+}/Sn^{4+} for the two samples are very close. Thus, the high ratio of Sn^{2+}/Sn^{4+} is not mainly caused by the screening of RuO_2.

When the two RuO_2/ITO samples are exposed in Ar^+ sputtering for a short time, for example, 0.5 minutes, the ratios of Sn^{2+}/Sn^{4+} for the both samples drop rapidly in Figure 5.9. After longer sputter time (from 0.5 to 4.0 minutes), the ratios for the two samples fluctuate between 40% and 60%. From Figure 5.8 one can find that the ratios of Sn/In gradually decrease from 0.5 to 4.0 minutes of sputtering. It proves again that the screening of RuO_2 is not the main reason for the high ratio of Sn/In. The possible main reason for the high ratio of Sn/In is the reduction of Sn^{4+} caused by RuO_2 deposition. In Figure 5.8 (a), the intensity ratio of Sn/In drops from 14.43% to 13.46% from 0 to 0.2 minutes sputtering. The change of the ratios indicates that only a little amount of Sn content is removed by Ar^+ sputtering. In Figure 5.9, the intensity ratio of Sn^{2+}/Sn^{4+} reduces from 90.7% to 57.73% from 0 to 0.2 minutes sputtering. The reduced ratio indicates that more Sn^{2+} ions are removed than the Sn^{4+} by Ar^+ sputtering. As a result, one can conclude that 0.2 minutes Ar^+ sputtering removes only a little part of Sn content, in which the percentage of Sn^{2+} is more than Sn^{4+}. It seems that the Sn^{2+} ions accumulate in the top layers of the RuO_2/ITO sample. The peak fitting is also done on the Sn3d spectrum of ITO with 30 minutes UV-ozone radiation. The intensity ratio of Sn^{2+}/Sn^{4+} is 26.0%. The ratio increases after the RuO_2 deposition, but the increase is not proportional to the amount of the deposited RuO_2. Thus, the high ratio of Sn^{2+}/Sn^{4+} is due to the increased amount of Sn^{2+}. The increased Sn^{2+} ions are produced by the RuO_2 deposition. During the RuO_2 deposition process, the Ru atoms from target, oxygen atoms from atmosphere, and the Sn-rich surface form the Ru-Sn-O ternary oxide system. A part of Ru atoms take oxygen ions from Sn-O bonds to reduce the oxidation state of

Sn^{4+} to +2. The Sn^{2+} ions accumulate on the top layers of the Ru-Sn-O ternary oxide. In this case, when the Ar^+ sputtering is applied for a short time. The surface Sn^{2+} is removed first and leads to the rapid decrease of the ratio of Sn^{2+}/Sn^{4+}.

5.3.6 Reduction of Ru^{4+} by Ar^+ Sputtering

The Ru3d spectra in Figure 5.2, Figure 5.6, and Figure 5.7 show the peak shift which correlates with the Ar^+ sputtering. All peaks shift to lower binding energy side after Ar^+ sputtering. Due to the complex conditions of the Ru-Sn-O ternary oxide system, a parallel experiment is done to facilitate the analysis of Ru3d spectra.

A reference sample, the thick RuO_2 film, is introduced in the parallel experiment. The RuO_2 film is deposited on a SiO_2 substrate. The thickness of the RuO_2 film is 50 nanometers. The RuO_2/SiO_2 sample is irradiated by UV-ozone treatment for 30 minutes before introduced into the XPS analysis chamber. The Ar^+ sputtering is employed in the XPS measurement. The kinetic energy of the Ar^+ sputtering applied on the RuO_2/SiO_2 sample is 2 keV.

5.3.6.1 Change of Ru3d and O1s Core-Level Spectra of RuO_2/SiO_2 after Ar^+ Sputtering

The Ru3d and O1s core-level spectra of the RuO_2/SiO_2 sample with different surface treatments are collected and display in Figure 5.10. The RuO_2/SiO_2 sample is stored in air at room temperature. The sample without any surface treatments is labeled as “as-received” sample. The Ru3d spectra of the RuO_2/SiO_2 sample before and after UV-ozone radiation show no peak shift in Figure 5.10 (a). The two Ru3d spectra have different parts between 283 eV to 285 eV. In Figure 5.10 (b), if normalizing the two O1s peaks to the same height, one will find that the O1s spectra collected before and after UV-ozone radiation also have different parts between 530.5 eV

to 533.0 eV. The capability of carbon-based contaminant removal of UV-ozone radiation is already proved in Figure 5.1. Thus, the differences in Ru3d and O1s spectra must result from the removal of surface carbon-based contaminant.

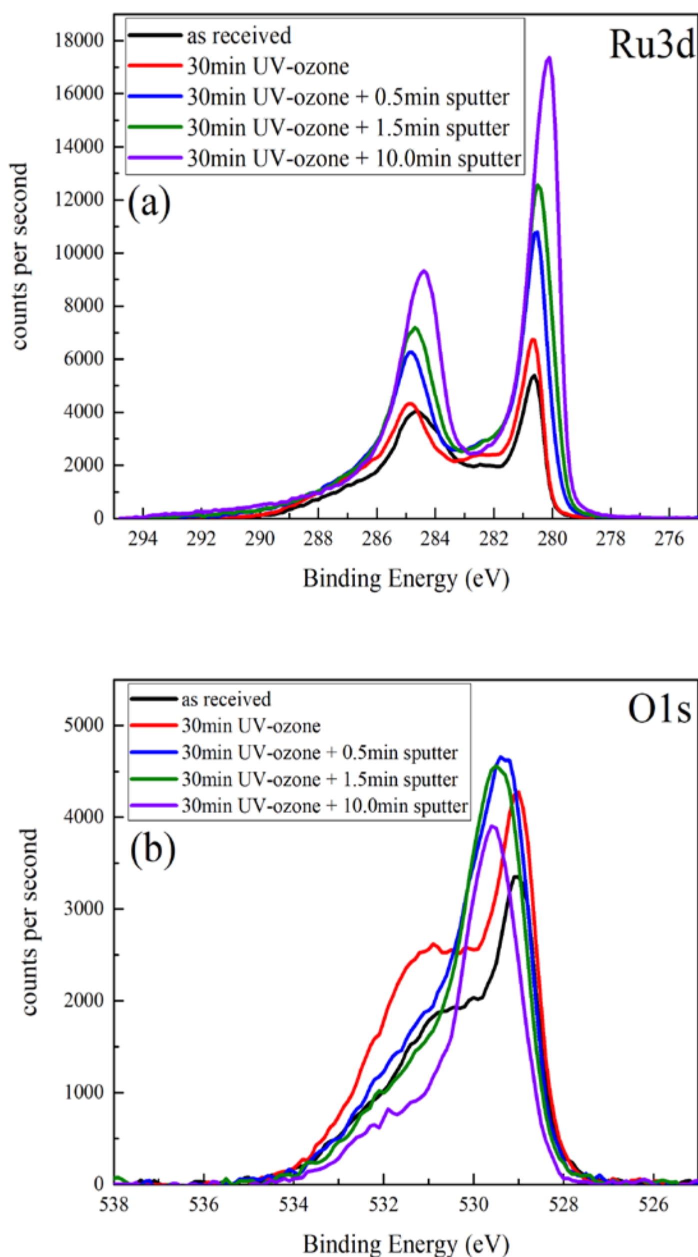

Figure 5.10 Ru3d and O1s core-level spectra of the RuO_2/SiO_2 sample with various surface treatments.

After Ar^+ sputtering, the intensities of Ru3d spectra continue increasing in Figure 5.10 (a). Simultaneously, the Ru3d spectra begins to shift to lower binding energy side as a function of increased sputter time. The change in O1s spectra is more complex after Ar^+ sputtering. The intensities of O1s spectra increase after 0.5 minutes Ar^+ sputtering. The intensity decreases after further sputtering. The line-shapes of O1s spectra also changes after sputtering. Before Ar^+ sputtering, the O1s spectra is like a main peak with a high-intensity satellite peak at higher binding energy side. After sputtering, the intensity of the satellite peak decreases greatly. The main peak broadens and shifts to higher binding energy side at 529.5 eV. The line-shape of the O1s spectrum with 10.0 minutes sputtering is similar as the O1s spectrum of the freshly deposited RuO_2 in reference [94]. Kim et al. claimed that the O1s peak had such highly asymmetrical line-shape, even the spectrum was collected from the intrinsic to clean and well-defined RuO_2 (110) sample [94]. The intensity of the satellite peak which was at 2.5 eV higher binding energy side would increase when the sample was stored in the XPS chamber for several hours. The RuO_2 sample would absorb water and oxygen contained compounds on the surface in such high vacuum. When the RuO_2 sample with adspecies was heated to 425˚C in oxygen atmosphere, the intensity of the satellite peak would return to the original height because the adspecies was removed. Kim et al. concluded that the satellite peak in the O1s spectrum belonged to the adsorbed contaminant on the surface of RuO_2 [94].

In this study, the intensities of the satellite peaks in O1s spectra decrease with increased sputter time because the surface contaminant is gradually removed by Ar^+ sputtering. After 10.0 minutes sputtering, intensities of the main peak and the satellite peak both deceases significantly. The decreased intensity of the satellite peak still mainly results from the removal of surface

contaminant. The decreased intensity of the main peak indicates the oxygen preferential sputtering effect of the Ar^+ sputtering.

5.3.6.2 Peak Fitting on Ru3d of RuO_2/SiO_2

The Ru3d spectrum has complicated components. The Ru3d spectrum is like two spin-orbital splitting peaks overlapping a thick background. Of cause, the bottom part of the spectrum is no the background. It contains important information about the chemical binding of Ru ions. In literatures, the part between the two spin-orbital splitting peaks and the part at higher binding energy side of the $Ru3d_{3/2}$ peak are considered as the satellite peaks of $Ru3d_{5/2}$ and $Ru3d_{3/2}$. Many studies claimed that the satellite peaks belong to surface RuO_3[95][96][97]. Because the satellite peak is at higher binding energy side of the main peak, and the O1s peak also shows a satellite peak at higher binding energy side, many studies concluded that the satellite peaks were from the Ru ions with higher oxidation state +6. However, RuO_3 is volatile in solid phase. The RuO_3 on RuO_2 surface is questioned by other studies [94][98][99][100][101]. Kim et al. studied the molecular beam epitaxial prepared RuO_2 by using XPS and X-ray photoelectron diffraction (XPD) [94]. The reflection high-energy electron diffraction (Rheed) and the low-energy electron diffraction (LEED) were employed to confirm the well-defined rutile structure in the surface region of prepared RuO_2 sample. No structure of RuO_3 was found. The analysis of XPD proved the origination of the satellite peaks in Ru3d spectra. Kim et al. concluded that the signal electrons of the satellite peaks in Ru3d was only from the cation sites in the rutile lattice, and the satellite peaks resulted from the final-state screening effect [94].

The mechanism of final-state screening effect is already depicted in Chapter 4. There is an alternate theory, plasma excitation, to explain the double peaks in the 3d state core-level

spectra such as In3d and Sn3d spectra. It is also depicted in Chapter 4. For Ru3d spectra, the plasmon excitation is more preferable in literatures [98][99]. The Ru3d surface core-level shift was calculated by using density-function theory [98]. In the calculation, the final-state screening effect is included. The calculation results showed that the energy distance between the screened and unscreened peak was less than 0.2 eV [98]. H. Over et al. combined the calculated data from density functional theory calculation and the experimental data collected by high resolution core-level spectroscopy with resolution 80 meV [99]. They concluded that the satellite peak in Ru3d resulted from the plasmon excitation because the energy distance between the satellite peak and the $Ru3d_{5/2}$ peak is close to the electron energy loss. As a result, the plasmon excitation is preferred in this study to analysis the Ru3d spectra.

The Ru^{4+} ions in the RuO_2 sample have different coordination numbers. The Ru^{4+} ion in the bulk bonds with six oxygen ions to form rutile structure. Ru^{4+} ion on the surface usually bond with five oxygen ions and is named coordinatively unsaturated Ru (cus-Ru) [98][99][100]. The binding energies of the bulk Ru^{4+} and cus-Ru were calculated by using density functional theory [98][99][100]. The calculation result demonstrated that cus-Ru had lower binding energy than the bulk Ru^{4+} did, and the energy difference was about 0.3 eV [98][99][100]. The cus-Ru plays an important role in the chemical activity of the RuO_2 because it can strongly absorb ligands and oxygen [98]. When the cus-Ru absorbs an oxygen atom, the cus-Ru with the absorbed oxygen is labelled cus-Ru+O. The binding energy of the cus-Ru+O become about 1.0 eV higher than that of the bulk Ru^{4+} [99][100][101]. The cus-Ru ions don’t only absorb oxygen atoms, but also oxygen contents. For example, when cus-Ru ions absorb CO molecules, the binding energy of $Ru3d_{5/2}$ will shift 1.2 eV to higher binding energy side [101].

The peak fitting process in this study includes the components of carbon, Ru metal, cus-

Ru, bulk Ru^{4+}, and cus-Ru+O. The RuO_2 sample is exposed in air. The cus-Ru may absorb various oxygen contents on the surface. Hence, the cus-Ru+O represents not only the cus-Ru ions which absorb oxygen atoms, but also the cus-Ru ions which absorb other oxygen contents. The cus-Ru, the bulk Ru^{4+}, and cus-Ru+O components have plasmon peaks at 1.8 eV higher binding energy side, respectively. Christou et al. mentioned the Gaussian-Lorentzian characters of the main peak and the plasmon peak in the plasmon excitation model [102]. The plasmon peak had more Lorentzian character than the main peak because the plasmon lifetime was reflected by the width of the Lorentzian peak [50][102]. The C1s peak is also considered in the peak fitting process. The binding energy of C1s is set at 284.8 eV. In this study, the $Ru3d_{5/2}$ and $Ru3d_{3/2}$ main peaks and C1s peaks are created by Gaussian function. The plasmon peaks are created by Lorentzian function. The background of the raw Ru3d spectrum is removed by Shirley function.

The peak fitting result of the Ru3d spectra of the RuO_2/SiO_2 sample is shown in Figure 5.11. There are three components in the Ru3d spectrum of the sample with 30 minutes UV-ozone radiation: C1s, cus-Ru+O and bulk Ru^{4+}. The binding energy of the C1s is at 284.79 eV. The relative peak area of the C1s is only 6.00% of the total peak area. The total peak area is the sum of peak areas of all components. The relative peak area is the percentage of a specific component to the total peak area. The relative peak areas of cus-Ru+O and bulk Ru^{4+} are 29.3% and 64.7%, respectively. After 0.5 minutes sputtering, a new component, cus-Ru, appears at 280.50 eV. The relative peak area of cus-Ru is 13.2%. The C1s disappears. The relative peak area of cus-Ru+O and bulk Ru^{4+} reduced to 20.5% and 60.7%, respectively. After 10.0 min sputtering, the cus-Ru+O disappears, and Ru metal appears. The relative peak area of Ru metal is 14.4%. The relative peak area of cus-Ru increases to 42.0%. The relative peak area of the bulk Ru^{4+} decreases to 43.7%.

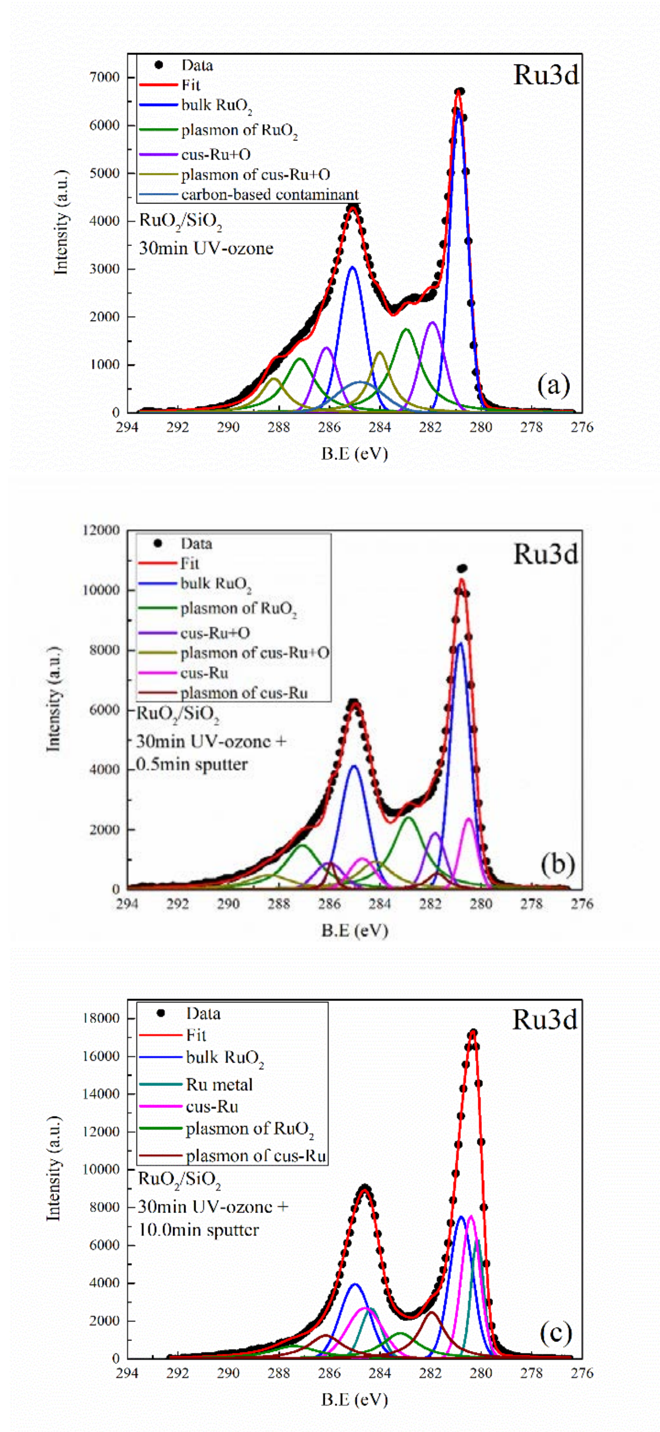

Figure 5.11 Peak fitting on Ru3d of RuO_2/SiO_2.

The peak fitting result demonstrates appearance of Ru metal and cus-Ru which are produced by Ar^+ sputtering. The produced Ru metal and cus-Ru lead to the peak shift of Ru3d of RuO_2. The RuO_2 exposed in air absorbs oxygen contents on the surface. The surface Ru ions

exist as cu-Ru+O. When Ar^+ sputtering is applied, the ad-species can be removed. The cus-Ru+O turns to cus-Ru. The Ar^+ sputtering also removes surface oxygen, cus-Ru, and cus-Ru+O ions and exposes the bulk Ru^{4+} on the surface. The bulk Ru^{4+} ion loses one oxygen ion and becomes cus-Ru. Thus, the cus-Ru peak appears after Ar^+ sputtering. After 10.0 minutes sputtering, the surface cus-Ru+O ions are removed and transferred into cus-Ru completely. Consequently, the cus-Ru+O peak disappears. Because of the oxygen preferential sputtering effect of the Ar^+ sputtering, the surface oxygen ions are more removed than cations. In this case, the cus-Ru can lose all bonded oxygen ions and transform to Ru^0.

The peak fitting result reveals the composition change of Ru3d spectra caused by Ar^+ sputtering. The composition change leads to the peak shift to lower binding energy side. The same peak fitting method is applied on the Ru3d spectra of the RuO_2/ITO samples.

5.3.6.3 Peak Fitting on Ru3d of RuO_2/ITO

The peak fitting is done on the Ru3d spectra of 1-minute and 2-minute deposited RuO_2/ITO samples. The relative peak area of each component is plotted as a function of sputter time in Figure 5.12.

Figure 5.12 (a) displays the component change of 1-minute deposited sample. The C1s peak represents the surface carbon-based contaminant. In the Ru3d spectrum of the sample with UV-ozone radiation, the intensity of the C1s is low. The relative peak area is only 7.5%. After Ar^+ sputtering, the intensity decreases rapidly. At 0.2 and 0.5 minutes sputtering, the relative peak areas of the C1s are 0.2% and 1.0%, respectively. The C1s peak disappears after further sputtering. The rapid decrease indicates that the remaining carbon-based contaminant is further removed by Ar^+ sputtering. The relative peak area of cus-Ru+O decreases with increased sputter

time because the ad-species and surface cus-Ru+O ions are removed by Ar^+ sputtering. The relative peak area of the bulk Ru^{4+} increases from 0 to 1.0 minute sputtering and decreases from 1.0 to 7.8 minutes sputtering. The increase is due to the removal of top layers. The further sputtering removes the bulk Ru^{4+} and transfer the bulk Ru^{4+} into cus-Ru simultaneously. Therefore, the relative peak area of the bulk Ru^{4+} decreases with increased sputter time. The peak of cus-Ru appears after 1.0 minutes sputtering.

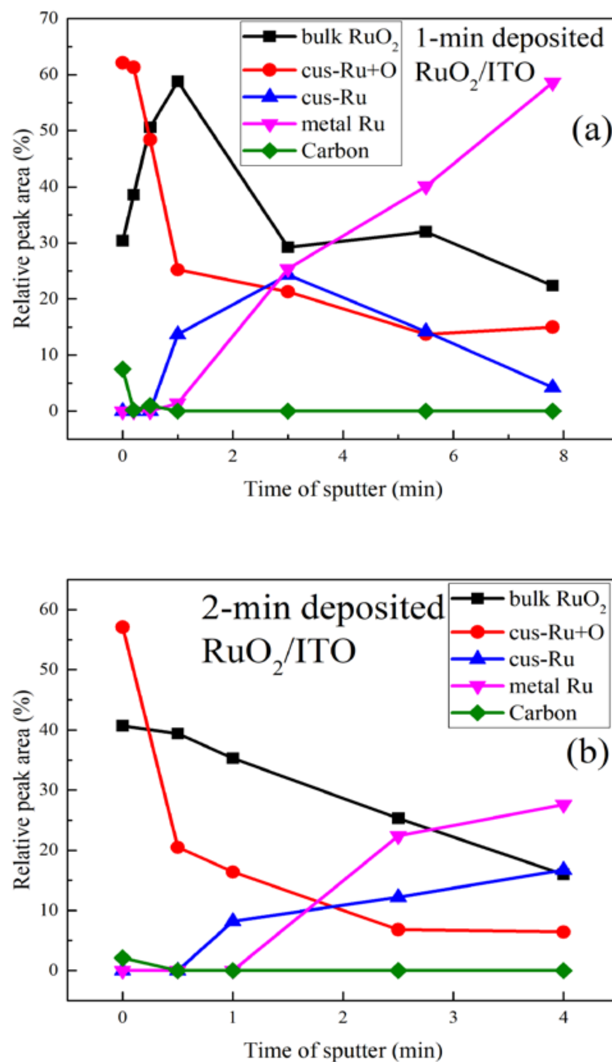

Figure 5.12 Peak fitting results of Ru3d of the RuO_2/ITO samples with various sputter time.

The intensity of cus-Ru peak increases with increased sputter time and reaches the maximum at 3.0 minutes sputtering. Then, the intensity decreases with increased sputter time. Like appearance of cus-Ru in the RuO_2/SiO_2 sample, the cus-Ru in RuO_2/ITO sample is also produced from surface cus-Ru+O and the bulk Ru^{4+} ions. The Ar^+ sputtering removes ad-species from cus-Ru+O ions and removes top layers of RuO_2/ITO to expose the bulk Ru^{4+} ions on the surface simultaneously. As a result, the cus-Ru peak appears and the intensity increases with increased sputter time. From 3.0 to 7.8 minutes sputtering, part of the cus-Ru ions on the top layers are removed by Ar^+ sputtering, and part of cus-Ru ions transform into Ru^0. The relative peak area of cus-Ru decreases because the amount of new produced cus-Ru is less than the amount of consumed cus-Ru. The peak of Ru^0 appears at 1.0 minute sputtering, and the relative peak area always increases with increased sputter time.

The component change of Ru3d spectra of the 2-minute deposited sample is displayed in Figure 5.12 (b). The relative peak areas of cus-Ru+O and the bulk Ru^{4+} decreases with increased sputter time, while the relative peak areas of cus-Ru and Ru^0 increases with increased sputter time. The C1s peak disappears after 0.5 minutes sputtering.

The peak fitting result of the Ru3d spectra demonstrates that Ar^+ sputtering produces Ru^0 and cus-Ru from cus-Ru+O and the bulk Ru^{4+}. The metal Ru and cus-Ru have lower binding energies than the bulk Ru^{4+} and cus-Ru+O. The peak shift of Ru3d spectra is due to the decreased amount of cus-Ru+O and the bulk Ru^{4+} and the increased amount of cus-Ru and Ru^0. A little peak shift in Figure 5.1 must be pressed. The Ru3d spectrum of the RuO_2/ITO sample shifts a little to higher binding energy side after UV-ozone radiation. However, the Ru3d spectrum of the RuO_2/SiO_2 sample doesn't shift after UV-ozone radiation in Figure 5.10. Thus, the shift is not caused by the surface contaminant removal. It must be due to the component

change. The shift in Figure 5.1 indicates that the UV-ozone radiation oxidizes the RuO_2/ITO sample. The oxidation can increase the relative peak area of cus-Ru+O so that the convoluted Ru3d peak shifts to higher binding energy side. The shift also indicates that the oxygen pressure in the RuO_2 deposition is too low to fully oxidize the deposited Ru atoms.

5.3.7 Evolution of Work Function

The work function of the RuO_2/ITO samples is calculated from the UPS spectra. The UPS spectra are displayed in Figure 5.13. The Fermi level is calibrated by the measured Fermi edge of the Ar^+ sputtering cleaned Au. Due to the metallic electrical conductivity of RuO_2, the Fermi edge is observed in the UPS spectra of 1-minute deposited and 2-minute deposited RuO_2/ITO samples. The VBM of all spectra is located at 0 eV. The peak between 0 to 3.0 eV belongs to RuO_2 and Sn^{2+}. It is obvious that the intensity of this peak decreases with sputter time. Thus, the peak of RuO_2 is in the dominant place between 0 to 3.0 eV. The work function equals the difference of the energy of the ultraviolet source and the width of the UPS spectrum. The width of the UPS spectrum is the energy distance between the Fermi edge and the secondary edge. The position of secondary edge is determined by the intersection of the linear extrapolation of the secondary edge and the base line. The work function versus sputter time is plotted in Figure 5.14. Figure 5.14 summaries the work function of 1-minute deposited and 2-minute deposited RuO_2/ITO samples. The work function of the ITO is also included for comparison. The kinetic energy of the Ar^+ sputtering is 1 keV in Figure 5.14.

The highest work function is from the 2-minute deposited RuO_2/ITO sample with 30 minutes UV-ozone radiation plus 1.0 minute Ar^+ sputtering. The work function increases from 4.81 eV to 4.98 eV when the Ar^+ sputtering is applied on the sample from 0.5 minutes to 1.0

minute. The increase of the work function is probably due to the removal of surface contaminant.

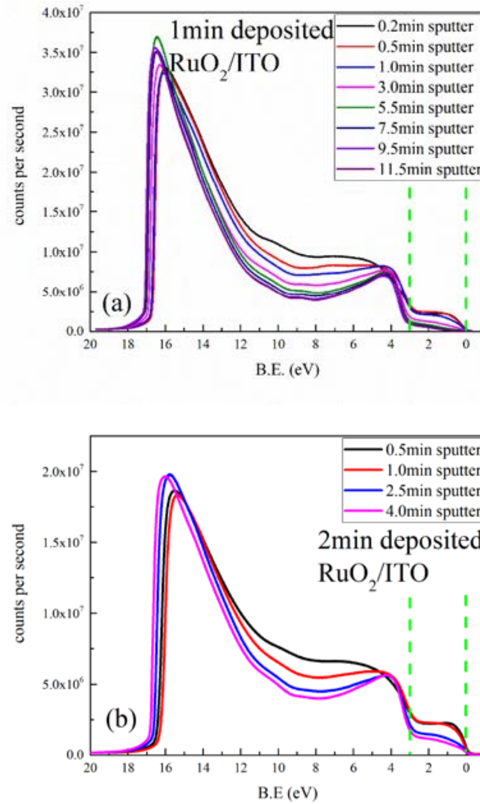

Figure 5.13 UPS spectra of the 1-minute deposited and 2-minute deposited RuO2/ITO samples, the two samples are pre-treated by 30 minutes UV-ozone radiation.

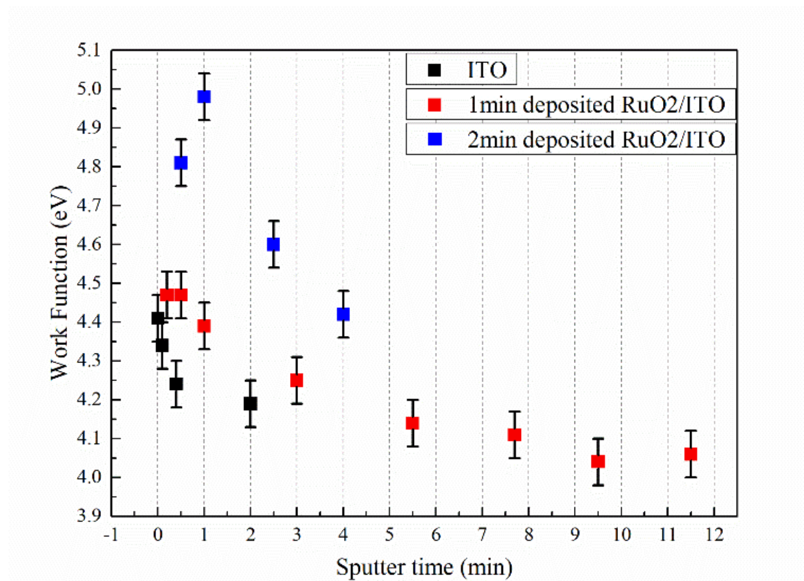

Figure 5.14 Work function of ITO, 1-min deposited and 2-min deposited RuO_2/ITO. All samples are pre-treated by 30 minutes UV-ozone radiation.

The decreased relative peak area of the cus-Ru+O in Figure 5.12 (b) and the change of line-shape of the UPS spectra in Figure 5.13 (b) can support this assumption.After 0.5 minutes sputtering, the C1s peak cannot be detected. The main contaminant is the absorbed oxygen contents. In Figure 5.12 (b), the decreased relative peak area of the cus-Ru+O indicates the decrease of absorbed oxygen content. In Figure 5.13 (b), the spectra of the 0.5 and 1.0 minute sputtered samples have plateaus in the range from 0 to 3.0 eV. This plateau mainly belongs to the RuO_2 valence band [88]. The intensity (peak area) of this plateau reflects the amount of remaining RuO_2 on the surface of sample. The two spectra show the almost the same intensity of the plateau. If there is no surface contaminant, the two full spectra should have the similar intensities. However, the two spectra have different line-shapes and intensities from 3.0 to 10.0 eV. The spectrum of 0.5 minutes sputtered sample has higher intensity in this region. If reviewing the UPS spectra of ITO before and after UV-ozone radiation in Chapter 4, one will find the similar high intensity of the UPS spectrum of the as-received ITO sample in the region 5.8 eV to 11.9 eV. Thus, the higher intensity in the region 5.8 to 11.9 eV in the spectrum of the 0.5 minutes sputtered sample is attributed to the surface contaminant. The XPS and UPS data depicts that the 1.0 minute sputtered sample has less surface contaminant than the 0.5 minutes sputtered sample. As a result, the increase of the work function results from the removal of surface contaminant.

From 1.0 minute to 4.0 minutes sputtering, the work function of the 2-minute deposited sample decreases to 4.42 eV. The main factor, which leads to the decrease of the work function, is the decreased amount of remaining Ru oxides. For the 4.0 minutes sputtered sample, the level of surface contaminant may be less than the 1.0 minute sputtered sample. However, less contaminant cannot compensate the loss of Ru oxides. The produced Ru metal may be another

factor which decreases the work function of the sample. The work function of Ru metal is only 4.7 eV [103], which is lower than that of the RuO_2. The sputtering also reduces the amount of surface Sn^{4+} and produces Sn^{2+}. It is another factor which decreases the work function. In Chapter 4 we already conclude that the produced Sn^{2+} from Sn^{4+} and the reduction of Sn^{4+} on the surface of ITO can decrease the work function of ITO. The ratio of Sn^{2+}/Sn^{4+} of the RuO_2/ITO samples displayed in Figure 5.9 demonstrates the high concentration of Sn^{2+} which is caused by RuO_2 deposition. The Ar^+ sputtering also reduces and removes the surface Sn^{4+} simultaneously. In sum, the amount of Ru oxides and surface Sn^{4+} control the work function of the RuO_2/ITO sample after 1.0 minute sputtering.

The highest work function of the 1-minute deposited RuO_2/ITO sample is only 4.47 eV. The UPS spectra of the sample with 0.2 and 0.5 minutes sputtering provide the same work function 4.47 eV. However, the two spectra have obviously different line-shapes. The line-shape of the spectrum of the 0.2 minutes sputtered sample is more like the line-shape of the spectrum of as-received ITO. Thus, the 0.2 minutes sputtered sample has more surface contaminant than the 0.5 minutes sputtered sample. The same work function obtained from the two different spectra indicates the limit influence of the contaminant on the work function of the RuO_2/ITO sample. When the surface contaminant is above a certain level, the work function of the RuO_2/ITO sample no longer decreases with increased level of surface contaminant. From 0.5 to 11.5 minutes sputtering, the work function of the RuO_2/ITO sample decreases from 4.47 eV to 4.04 eV. The decrease is apparently due to the removal of Ru oxides. However, the work function of RuO_2/ITO with 9.5 minutes sputter is lower than the work function of UV-ozone treated ITO. The removed surface Sn^{4+} apparently plays a role to lower the work function of the RuO_2/ITO sample. After 9.5 minutes sputtering, both deposited RuO_2 and the Sn-rich surface is

removed completely. The Ru3d spectrum of the 9.5 minutes sputtered sample is collected but not shown in this article. The Ru3d peak is not detectable. The work function of the ITO sample with heavy sputtering is measured for comparison. In the heavy sputter process, the kinetic energy of the Ar^+ sputtering is 2 keV, and the sputter time is 2.0 minutes. The measured work function of the ITO is 4.14 eV, which is close to the work function of the 9.5 minutes sputtered RuO_2/ITO sample. Thus, the low work function (4.04 eV) of the RuO_2/ITO sample with 9.5 minutes sputtering is due to the complete removal of deposited RuO_2 and the Sn-rich surface.

In sum, surface contaminant, amount of the deposited RuO_2, and Sn-rich surface which includes amount of Sn^{4+} and the Sn^{2+}/Sn^{4+} ratio are three factors which affect the work function of the RuO_2/ITO samples. Surface contaminant decreases the work function, while deposited RuO_2 and Sn-rich surface with high percentage of Sn^{4+} increase the work function. In this study, because the deposited Ru atoms are not fully oxidized by the oxygen from atmosphere, the surface Sn^{4+} ions are reduced by the RuO_2 deposition. If stronger oxidation atmosphere was applied in the RuO_2 deposition process to prevent the reduction, the work function of the RuO_2/ITO would be higher than 4.98 eV.

5.4 Conclusion

RuO_2 ultra-thin film is deposited on the UV-ozone treated ITO by the DC magnetron sputtering with different thicknesses. The deposited RuO_2 and the Sn-rich phase form a Ru-Sn-O ternary system on the surface of the RuO_2/ITO sample. The deposition process gives rise to the reduction reaction on the surface Sn^{4+}. The Ar^+ sputtering reduces Ru^{4+} to Ru^0 to cause the Ru3d XPS spectrum shifting to the lower binding energy side. The deposition of RuO_2 can increase the work function of ITO. The work function of the RuO_2/ITO is affected by four factors: the

contaminant, amount of the RuO_2 and the Sn-rich surface, and the Sn^{2+}/Sn^{4+} ratio in the Sn-rich surface. The contaminant decreases the work function, while the deposited RuO_2 and the Sn-rich surface with high percentage of Sn^{4+} increase the work function. The highest work function (4.98eV) is obtained from the RuO_2/ITO sample treated by 30 minutes UV ozone radiation plus 1.0 minute Ar^+ sputtering. This value can be higher if the influence from the surface contaminant and reduction of Sn^{4+} is eliminated.

CHAPTER 6

TUNING WORK FUNCTION OF INDIUM TIN OXIDE BY SE DEPOSITION AND XPS STUDY ON SE/ITO INTERFACE

6.1 Introduction

The importance of the high work function of ITO is already pressed in the previous chapters. We showed the limitation of UV-ozone radiation as an only-approach and the improved RuO_2 ultra-thin film deposition in improving the work function of ITO. The highest work function of UV-ozone treated ITO is 4.41 eV. The RuO_2 deposition improved the work function of ITO to 4.98 eV. However, the RuO_2 deposition also induced the reduction of the surfaced from Sn2+ to Sn^{4+}. The seemingly reaction between Sn and RuO2 is not desirable unless it still proves stable in contact with active layers in device applications.

The high work function of the RuO_2/ITO sample demonstrates the capability of the ultra-thin film deposition method in improving the work function of ITO. If the absorbed contaminant and the reduction reaction is prevented, the effect on work function of ITO may increase beyond 4.98 eV. Evaluation of another material other than RuO_2 but with higher work function is desirable. Selenium is a good option because of the high work function and low tendency to bond with oxygen atoms.

Selenium is a low-cost material and can be easily prepared by physical vapor deposition at low temperature. It is usually used for fabricating the cheap large-scale devices. The solid-state Se has trigonal, monoclinic, and amorphous forms in nature. The band gap of Se depends on its structure. The band gap of the crystal and amorphous Se is 1.8 and 2 eV, respectively [104][105]. Se has remarkable high work function 5.11 eV [106]. It was used for preparing the Se/ITO thin film solar cells in 1980s [107][108][109][110]. ITO is one of them. In the reported

Se/ITO thin film solar cells, a Tellurium film was inserted into the Se/ITO heterojunction to prevent the peeling and reduce the electrical resistivity of the Se film by increasing its crystallite size [107][108][109][110].

Because of the use of Te film, the Se film was not deposited on the ITO sample directly in literatures. There is no literature reporting on the chemical bonding at the Se/ITO interface and the effective work function of nanolayer coated ITO with Se.

In this study, the Se nanoscale ultra-thin films are deposited on the UV-ozone treated ITO substrates. No pealing is observed on these prepared Se/ITO samples. The work function of the Se/ITO samples is measured by in-situ UPS to prevent contamination from atmosphere. The work function change as a function of increased amount of deposited Se is evaluated. The chemical bonding at the Se/ITO interfaces is investigated by in-situ XPS and ARXPS.

6.2 Experimental

The Se is deposited on commercial available ITO/glass substrates via ion-beam sputtering deposition (IBS). The ITO/glass substrates are purchased from Luminescence Technology Corp with nominal sheet resistivity of 15Ω/□. 1 hour UV-ozone radiation is applied as pre-treatment before deposition. The UV-ozone radiation takes place in air. The distance from the UV-lamp to ITO surfaces is 10 centimeters. In the IBS process, the amount of deposited Se is controlled by the deposition time. The prepared Se/ITO samples are labelled by numbers from 1 to 8. The larger number means larger amount of deposited Se.

The in-situ XPS and UPS measurements are performed to investigate the surface chemistry and work function. In XPS measurements, the X-ray source is generated from the Al K alpha radiation (hυ=1486.6 eV). The XPS spectra are collected at 11.75 eV pass energy, 0.1

eV energy steps, and 45˚ TOA. Some of spectra are collected at different TOAs. These spectra will be specified in the discussion section. In UPS measurements, the ultraviolet source is the He I (hυ=21.22 eV). The pass energy and the energy step for acquisition of UPS spectra are 2.95 eV and 0.005 eV, respectively. A -9 Volt bias voltage is applied on the sample stage during the UPS spectra acquisition to increase the intensity of the secondary edge and separate the secondary edge of the sample from that of detector.

A parallel experiment is done to assist the analysis of Se/ITO samples. The Se is deposited on Si substrates and Si with native oxide (SiOx) substrates. The Se/Si and Se/SiOx samples are prepared and characterized via the same way of the Se/ITO samples.

6.3 Result and Discussion

6.3.1 Work Function Tuning by Se Ultra-Thin Film

The UPS spectra depict the band structures of the Se/ITO samples in Figure 6.1. The full spectra are plotted in Figure 6.1 (a). Part of valence bands near the Fermi edge is zoomed in in Figure 6.1 (b). The Figure 6.1 (c) displays the zoomed in secondary edges of the UPS spectra. The Se/ITO samples have different amount of deposited Se. The band structures change with the amount of deposited Se. In Figure 6.1 (a), the spectrum of ITO shows only one obvious peak which is located between 4.0 to 7.0 eV. After Se deposition, an extra peak in the region 1.0 to 4.0 eV is observed in the spectra of the sample 1, 2, and 3. Because no peak is shown in this region in the spectrum of ITO, the extra peak belongs to the valence band of Se. For the Se/ITO samples with more deposited Se on the surface, the line-shape of the peak between 4.0 to 7.0 eV changes. The line-shape shows two peaks instead of one peak in this region. The change of the valence bands of the Se/ITO samples can clearly be seen in Figure 6.1 (b).

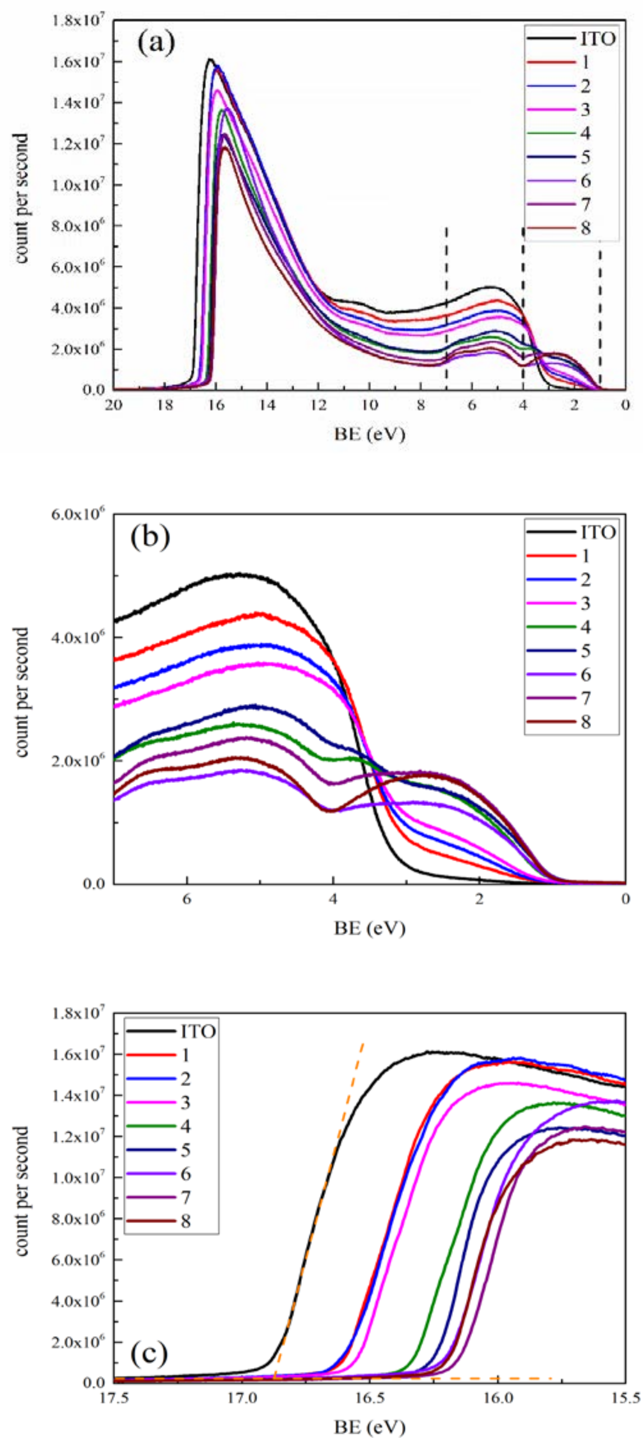

Figure 6.1 UPS spectra of the ITO and the Se/ITO samples

The intensity of the peak between 1.0 and 4.0 eV increases with increased amount of deposited

Se. The peak between 4.0 to 7.0 eV, which belongs to ITO, decreases with increased amount of deposited Se. Beginning from the sample 6, the peak in the region 4.0 to 7.0 eV is replaced by two peaks. The sample 8, which has the largest amount of deposited Se, shows the three-peak structure in the UPS spectrum. The three peaks have the similar intensities. The line-shape of this spectrum is the same as that of the spectrum of amorphous elemental Se [111]. The work function of the sample 8, obtained from the UPS spectrum, is 5.05 ± 0.06 eV which is close to that of the amorphous Se 5.11 eV [106]. The error ± 0.06 eV is already depicted in Chapter4. Thus, we can assume that the signal electrons from the ITO substrate is totally screened by the deposited Se in the sample 8.

The thickness of the deposited Se, if it is considered as a homogenous film, can be estimated by sampling depth of In3d spectrum. The sampling depth approximately equals three times of the inelastic mean free path. The software NISTSRD71 provides a value for the inelastic mean free path (IMFP) of the electrons with the kinetic energy 1042 eV in the grey selenium bulk which is 22.03 Å. Thus, the sampling depth is about 6.6 nm for the In3d spectrum. It means that the thickness of the deposited Se layer in the sample 8 is less than 6.6 nm.

The work function of the Se/ITO samples is calculated from the UPS spectra in Figure 6.1 (a). The Fermi level is calibrated by measuring the Fermi edge of sputtering cleaned Au. The position of the secondary edge is determined by the intersection of the secondary edge and the base line shown in Figure 6.1 (c). The calculated work function versus the ratio of Se/In is plotted in Figure 6.2. The ratio Se/In is the ratio of intensities of Se3d peaks and In3d$_{5/2}$ peaks. The intensity is calculated from the convoluted Se3d and In3d$_{5/2}$ peaks without background. The background is removed by Shirley function. In Figure 6.2, the sample 1, which has the lowest amount of deposited Se, has the work function 4.61 ± 0.06 eV. The work function increases with

increased amount of deposited Se. However, the work function stops increasing for the sample 6, 7, and 8. The work function of the sample 6, 7, and 8 is 5.04 ± 0.06, 5.06 ± 0.06, and 5.05 ± 0.06 eV, which is close to the work function of Se. It indicates that there is a cap for the work function of the Se/ITO samples. The work function of Se/ITO cannot beyond the work function of Se. In sum, the deposited Se ultra-thin film can enhance the work function of ITO, and the work function increases with increased amount of deposited Se and stops increasing at 5.05 ± 0.06 eV.

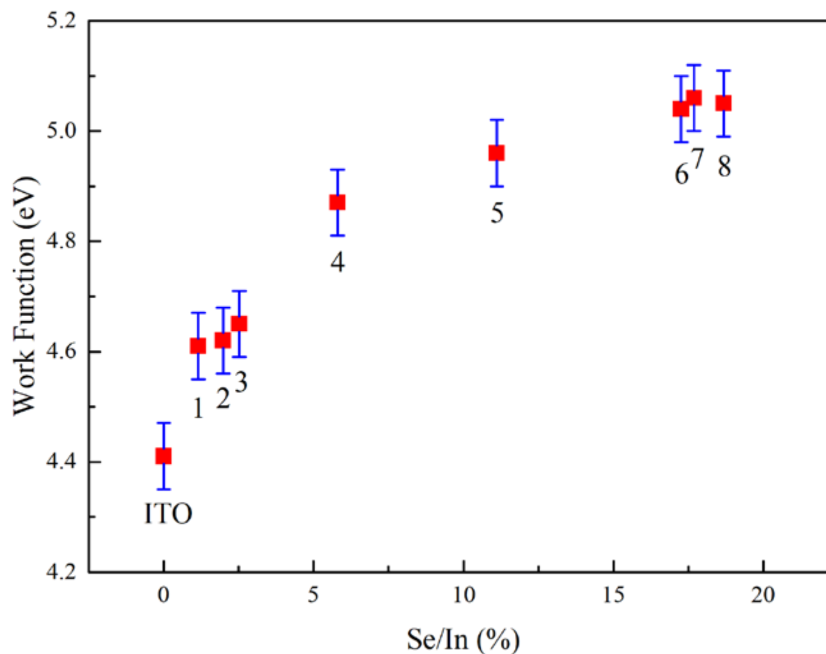

Figure 6.2 Work function versus intensity ratio of Se/In

6.3.2 Reduction of Sn^{4+} at Se/ITO Interface

6.3.2.1 Change of In3d, Sn3d, and O1 Spectra after Se Deposition

The ITO substrates are only treated by UV-ozone radiation before Se deposition. The Sn-rich surface is retained. In Chapter 4 we already mentioned that the high surface chemical activity of ITO is probably due to the Sn-rich surface. The Sn-rich surface may react with

deposited Se atoms at the Se/ITO interface. Thus, it is essential to investigate the chemical bonding at the Se/ITO interface.

If chemical bonding between Se and the Sn-rich surface is formed at the interface, it may be reflected in the Sn3d core-level XPS spectrum. The Sn3d spectra of the ITO substrate and the Se/ITO samples are collected to investigate the chemical bonding at the Se/ITO interface. When the peak shift happens on XPS data, it is essential to find a reliable energy reference to calibrate the XPS spectra. Because Se is not a metallic-like material, there is no Fermi edge in the valence band spectrum. Two extra core-level peaks, $InM_4N_{45}N_{45}$ and In3d, are collected to provide energy references. $InM_4N_{45}N_{45}$ is an Auger peak of indium. This peak will shift only if the surface charge occurs. The indium is in the bulk of the ITO substrate and will not involve the formation of the chemical bonding at the interface. Thus, the In3d is expected to have little change after Se deposition. In this case, it is appropriate to use In3d as the energy reference. The Sn-rich surface contains oxygen ions. Thus, O1s core-level spectra are also collected to provide more information about the interface.

The InMNN, $In3d_{5/2}$, $Sn3d_{5/2}$, and O1s spectra of the ITO substrate and the sample 1 are compared in Figure 6.3. Because the sample 1 has deposited Se on the surface, the core-level peaks and the Auger peak have lower intensities. To facilitate the comparison, the heights of the peaks from the sample 1 are normalized. The normalized InMNN spectra are displayed in Figure 6.3 (a). The InMNN spectrum of the sample 1 is superposed well on the InMNN spectrum of the ITO substrate. The InMNN spectra demonstrates that there is no surface charge. The $In3d_{5/2}$, $Sn3d_{5/2}$, and O1s spectra are displayed in Figure 6.3 (b), Figure 6.3 (c), and Figure 6.3 (d). The background of each peak is removed by Shirley function. In Figure 6.3 (b), the $In3d_{5/2}$ peaks are normalized to the same height. The height of the $In3d_{5/2}$ peak of the sample 1 is enlarged 1.12

time. The $Sn3d_{5/2}$ and O1s peaks of the sample 1 are also enlarged 1.12 time. In this case, the effect of the deposited Se which causes the reduced intensities of In3d, Sn3d, and O1s peaks is eliminated. The heights of peaks can reflect the concentration change correctly.

The two $In3d_{5/2}$ peaks have very similar line-shapes in Figure 6.3 (b). The little difference results from the final-state screening effect. The peak fitting results of $In3d_{5/2}$ peaks are displayed in Figure 6.4. The details of the peak fitting is already described in Chapter 4. The $In3d_{5/2}$ screened peaks of the two samples are at 444.76 eV. The $In3d_{5/2}$ peaks also proves the absence of the surface charge.

The $Sn3d_{5/2}$ peaks are displayed in Figure 6.3 (c). For the $Sn3d_{5/2}$ peak of the sample 1, the left leading-edge shifts 0.2 eV to lower binding energy side, and the right leading-edge shifts only 0.1 eV to lower binding energy side. Thus, the peak width shrinks, and the entire peak shifts to lower binding energy side. The shrink and the peak shift indicate the reduction of Sn^{4+}. The peak fitting is done on the $Sn3d_{5/2}$ peaks, and the results are displayed in Figure 6.5. For the $Sn3d_{5/2}$ peak of ITO, the relative peak areas of Sn^{4+} and Sn^{2+} are 76.9% and 20.0%, respectively. For the sample 1, the relative peak area of Sn^{4+} decreases to 67.2%, while the relative peak area of Sn^{2+} increases to 28.2%.

The O1s spectra are shown in fig. 6.3 (d). The part of O1s peak of the sample 1 in the region 531.3 to 534.0 eV has reduced intensity. According to the analysis in Chapter 4, it is known that this region belongs to the Sn-rich surface and oxygen-carbon based surface contaminants. In the Se deposition process, the remained surface contaminant is still on the surface of the substrate. Thus, the reduced intensity indicates the formation of the chemical bonding at the Se/ITO interface. The peak fitting results of O1s peaks are displayed in Figure 6.6. For the ITO substrate, the relative peak areas of the Sn-rich surface plus carbonate-like

contaminant and the hydroxyl-like contaminant are 28.1% and 8.4%, respectively. For the sample 1, the relative peak areas of the two peaks are 24.6% and 4.00%, respectively.

In sum, after Se deposition, the Sn3d and O1s spectra reflect the change of chemical bonding at Se/ITO interface.

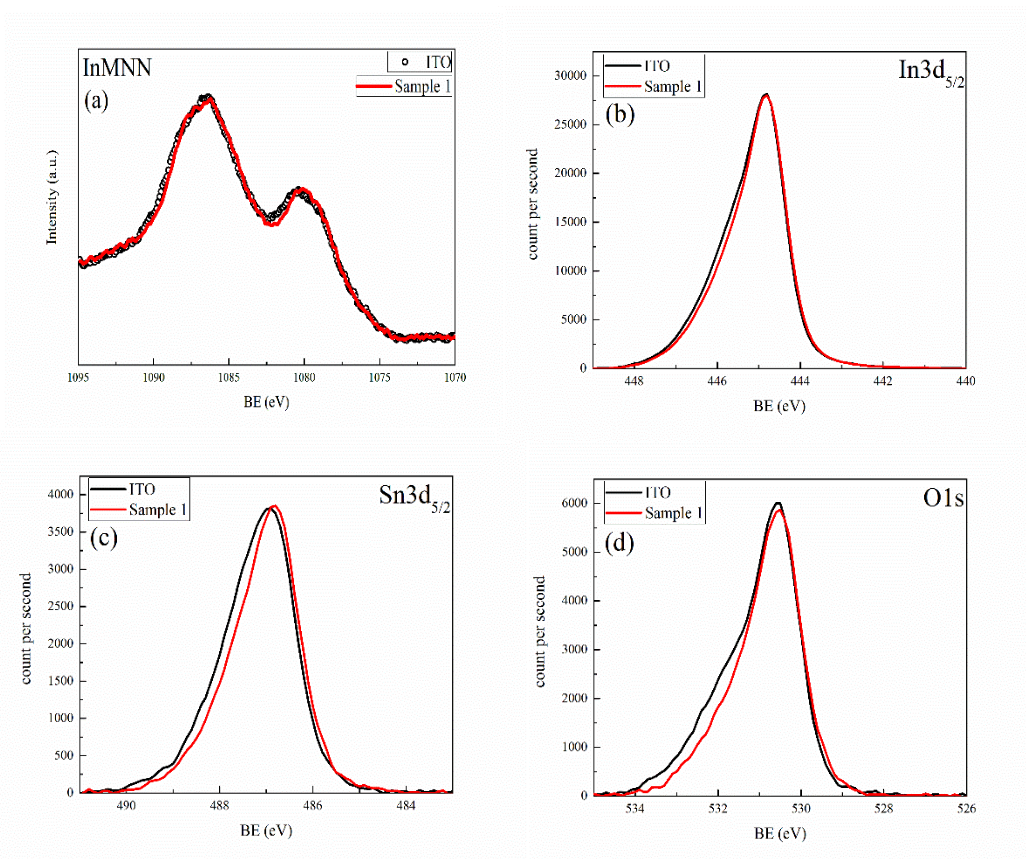

Figure 6.3 Comparison of core-level spectra of the ITO and the sample 1.

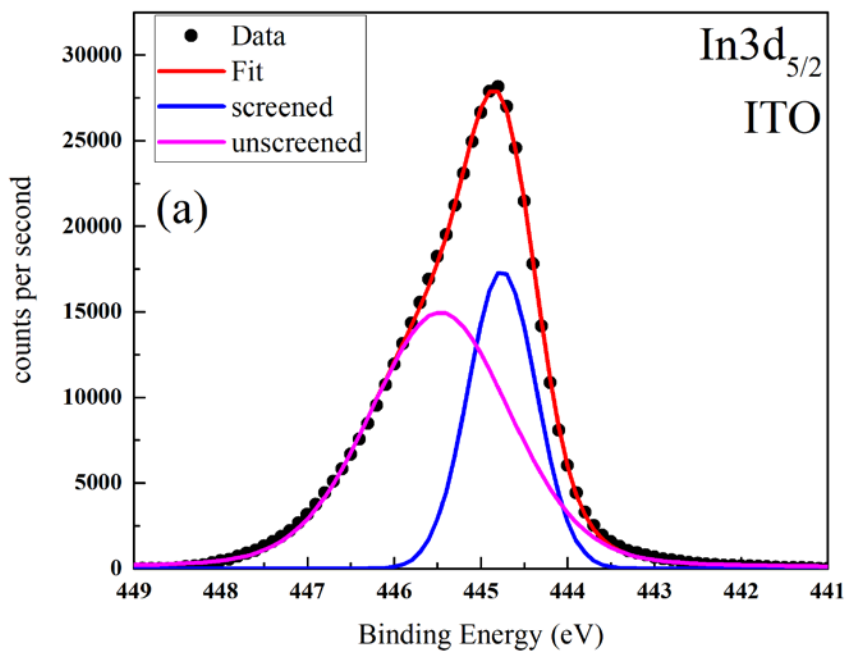

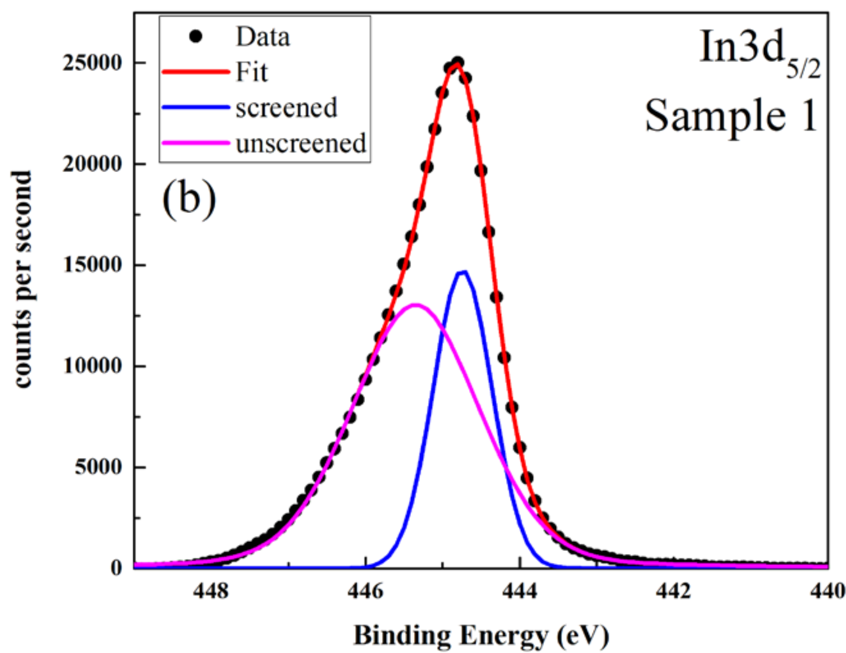

Figure 6.4 Peak fitting on In3d$_{5/2}$ peaks.

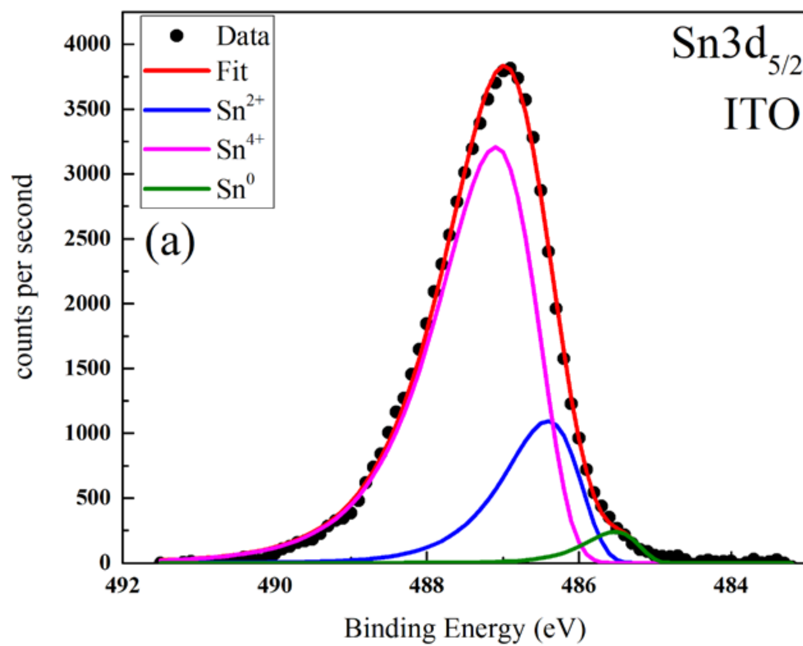

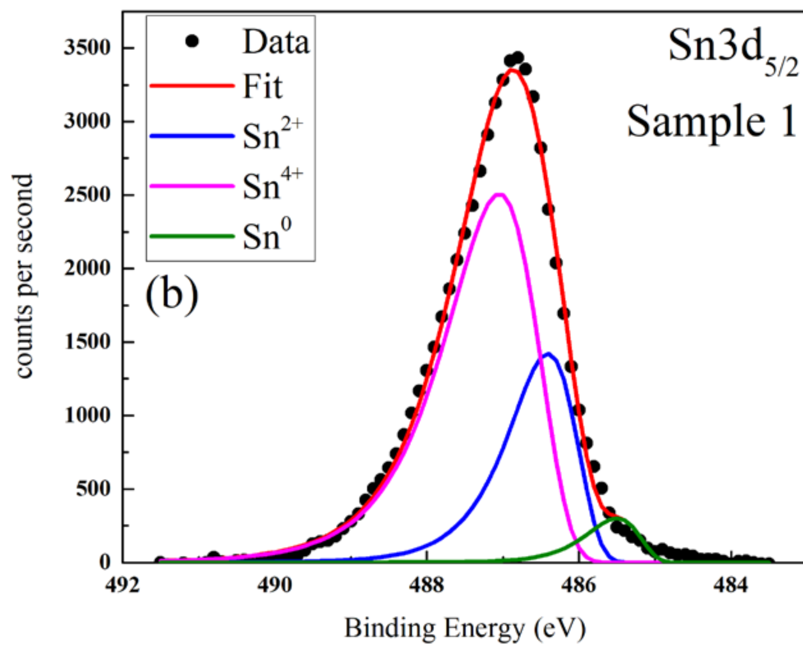

Figure 6.5 Peak fitting on $Sn3d_{5/2}$ peaks.

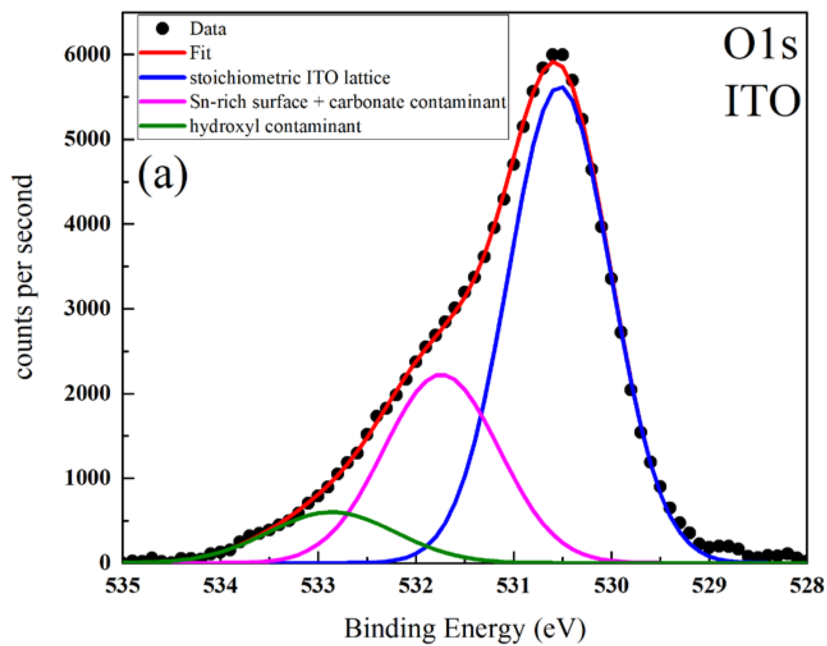

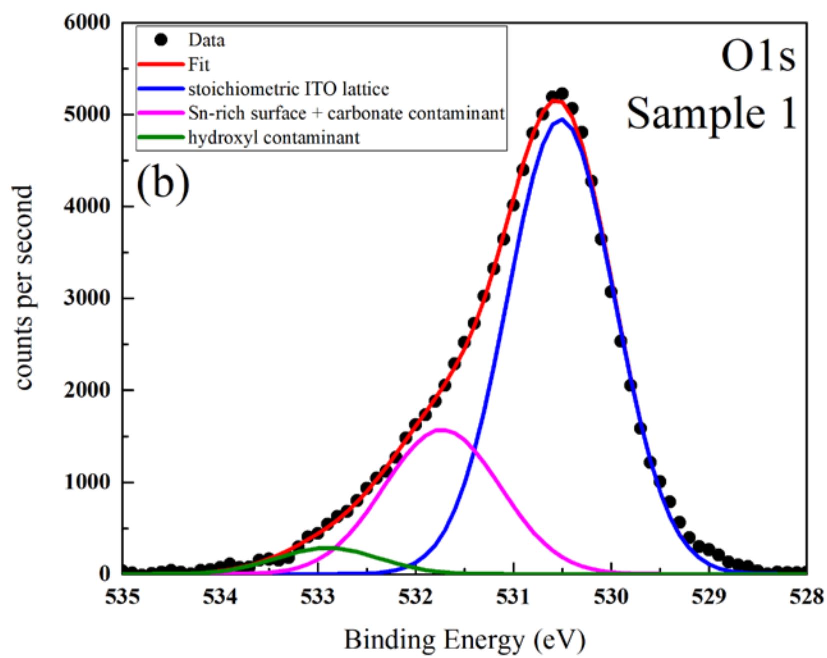

Figure 6.6 Peak fitting on O1s peaks.

6.3.2.2 Change of In3d, Sn3d, and O1s Spectra with Different Amount of Deposited Se

In this study, according to the sampling depth of XPS, only low amount of Se is deposited on the ITO substrate. The reactions at the Se/ITO interface may be not saturated when amount of Se is low. The formation of the chemical bonding may correlate with the amount of deposited Se until the formation is saturated. Thus, the XPS spectra of the Se/ITO samples with different amount of deposited Se are collected. The spectra of the selected samples are displayed in Figure 6.7. The sample 1 has the lowest amount of Se and the lowest work function. The sample 4 has the moderate work function and the amount of Se. The sample 6 has the almost highest work function. Actually, the sample 6, the sample 7, and the sample 8 have the identical In3d, Sn3d, and O1s spectra in the line-shapes and the peak positions. Thus, the spectra of the sample 1, the sample 4, and the sample 6 can represent the change in the core-level spectra of samples with different amount of Se. To facilitate comparison, the heights of the spectra of the sample 4 and sample 6 are normalized. These spectra are shown in Figure 6.7. The background of core-level spectra is removed by Shirley function.

The InMNN spectra are still used as the energy reference. Figure 6.7 (a) demonstrates the absence of surface charge. The normalized $In3d_{5/2}$ peaks are displayed in Figure 6.7 (b). The peaks shift to lower binding energy side with increased amount of Se. The normalized $Sn3d_{5/2}$ peaks in Figure 6.7 (c) and the normalized O1s peaks in Figure 6.7 (d) also show the same trend of shift. To investigate the compositional change, the same peak fitting methods used in Figure 6.4, Figure 6.5, and Figure 6.6 are applied on In3d, Sn3d, and O1s spectra of all Se/ITO samples.

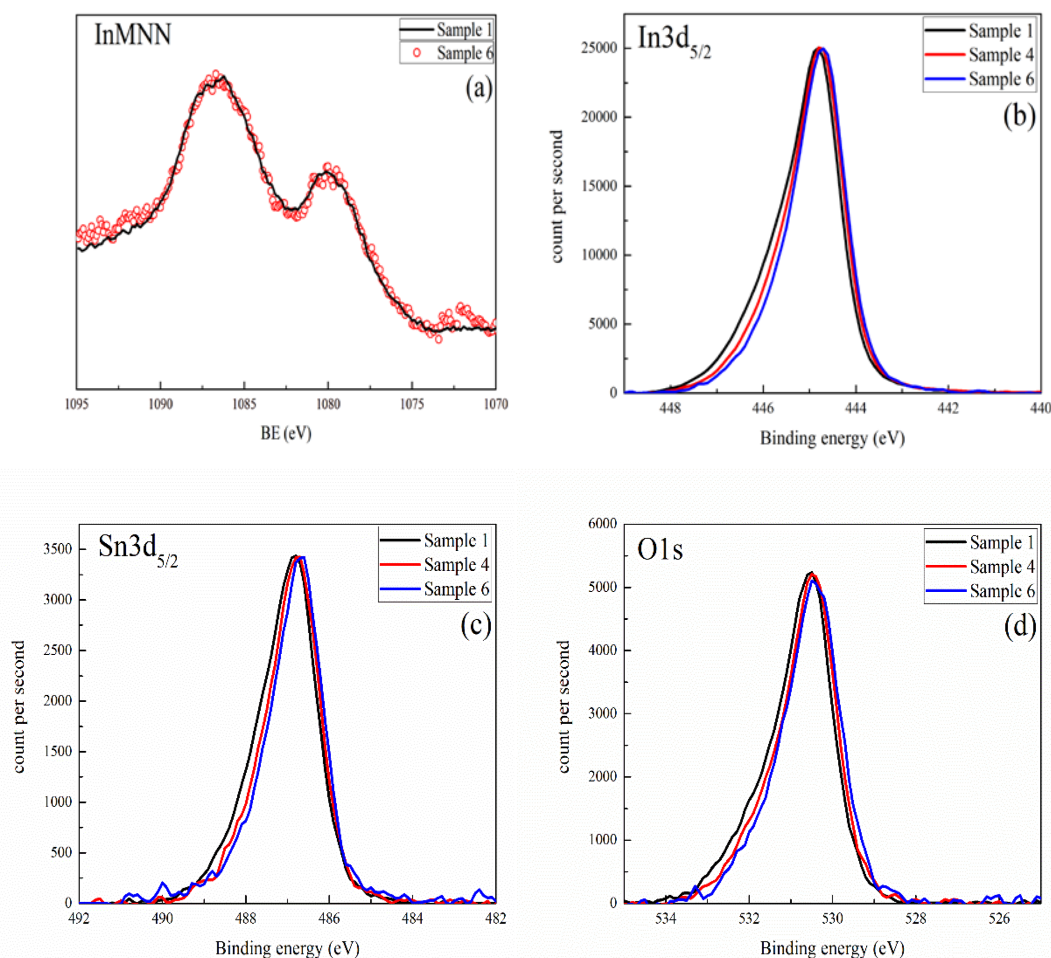

Figure 6.7 Comparison of core-level peaks of the Se/ITO samples.

The peak fitting is done on the $In3d_{5/2}$ spectra first. Because the In3d, Sn3d, and O1s peaks all shift to lower binding energy side with increased amount of deposited Se, the In3d peaks will be used as the energy reference to calibrate the respective Sn3d and O1s peaks. The binding energy of the screened $In3d_{5/2}$ peak versus peak area ratio of Se/In is plotted in Figure 6.8 (a). The Figure 6.8 (a) shows the binding energy of the screened $In3d_{5/2}$ peak shifts from 444.74 eV to 444.63 eV.

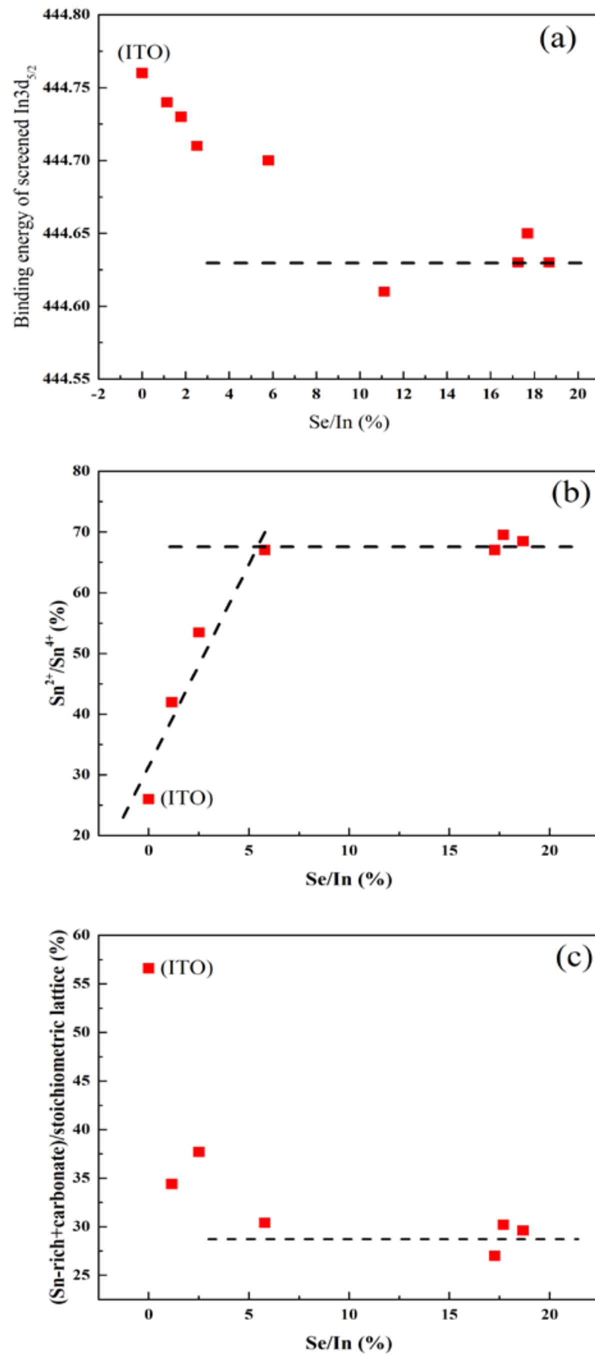

Figure 6.8 (a) Binding energy of screened $In3d_{5/2}$ peaks versus intensity ratio of Se/In. (b) intensity ratio of Sn^{2+}/Sn^{4+} versus intensity ratio of Se/In. (c) intensity ratio of the Sn-rich surface plus carbonate contaminant to the stoichiometric ITO lattice versus the peak area ratio of Se/In.

In the $Sn3d_{5/2}$ peak fitting process, the B.E. difference (energy levels) between the $Sn3d_{5/2}$ peak and $In3d_{5/2}$ peak must keep a constant. The peak fitting results provide the relative peak

areas of Sn^{2+} and Sn^{4+}. The peak area ratio of Sn^{2+}/Sn^{4+} versus peak area ratio of Se/In is plotted in Figure 6.8 (b). The peak area ratio of Sn^{2+}/Sn^{4+} for the ITO substrate is 26.0%. The ratio increases with increased amount of deposited Se. When the ratio reaches about 68%, it will stop increasing.

The peak fitting is also done on the O1s spectra. The energy distance between O1s peak and $In3d_{5/2}$ peak keeps a constant. The peak area ratio of the Sn-rich surface plus carbonate contaminant to the stoichiometric ITO lattice versus the peak area ratio of Se/In is plotted in Figure 6.8 (c). The ratio for the ITO substrate is 56.6%. After Se deposition, the ratio begins to decrease. When the ratio reaches about 30%, the decrease stops.

It seems that the increases in the Sn^{2+}/Sn^{4+} ratio in Figure 6.8 (b) and the decrease of Sn-rich in Figure 6.8 (c) both stops at the same point at which the peak area ratio of Se/In belongs to the sample 4. This inflexion point indicates that the formation of the chemical bonding at Se/ITO interface becomes saturated when the peak area ratio of Se/In reaches 5.80%.

6.3.3 Chemical Bonding of Se at Se/ITO Interface

6.3.3.1 Se3d Spectra of the Se/ITO Samples

The Se3d spectra of the eight Se/ITO samples are collected and displayed in Figure 6.9. The sample 1 has the least amount of deposited Se. The Se3d peak of the sample 1 has very low intensity and low statistics. However, it is still detectable according to the calculated limit of detection. Because of the low statistics, it is difficult to determine the position of this peak. The rest Se3d peaks have better statistics. The line-shapes of the Se3d peaks change with the amount of deposited Se in Figure 6.9. When the amount of the deposited Se is high, the Se3d peak shows two well separated peaks. When the amount of Se is low, the separation is not obvious. If

watching the highest point of the Se3d peaks, one will find that the Se3d peaks shift from 55.34 eV to 55.05 eV from the sample 2 to the sample 8. The compositional change in Sn3d spectra and O1s spectra indicates the reaction happening among Se, Sn, and O. Thus, the different line-shapes and peak shift in Figure 6.9 probably result from the compositional change of the Se3d spectra.

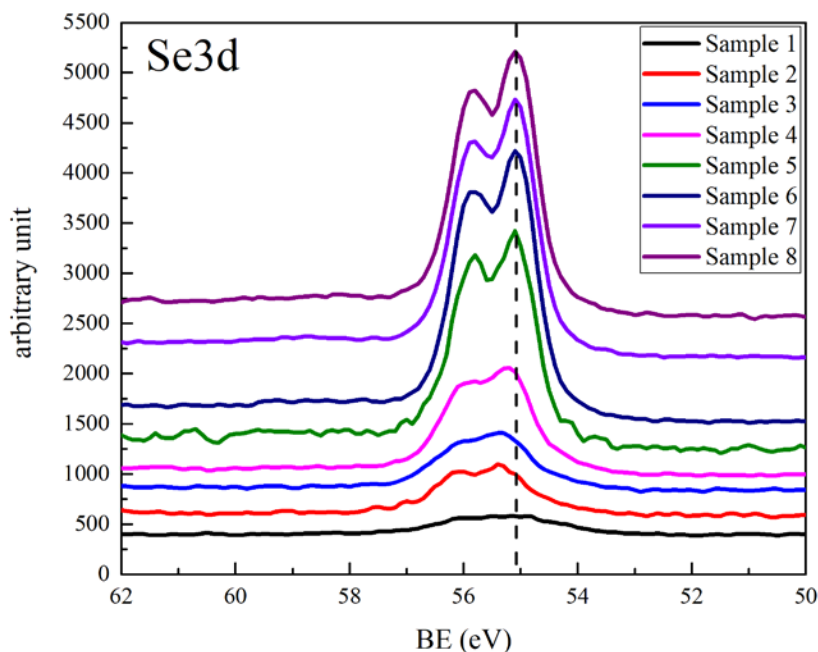

Figure 6.9 Se3d spectra of the Se/ITO samples.

To examine the composition of the Se3d spectra of the Se/ITO samples, the Se3d spectrum of the sample 8 is compared with the Se3d spectrum of elemental Se. The spectra are compared in Figure 6.10 (a). The two spectra are normalized to the same height to facilitate the comparison. The Se3d spectrum of the elemental Se shows two separated peaks. It is obvious that these two peaks are the spin-orbital splitting peaks of Se3d of Se^0. The peak at lower binding energy side is the $Se3d_{5/2}$ peak. In Figure 6.10 (a), the $Se3d_{5/2}$ peaks of the two samples are normalized to the same height. However, the $Se3d_{3/2}$ peaks exhibit the different heights.

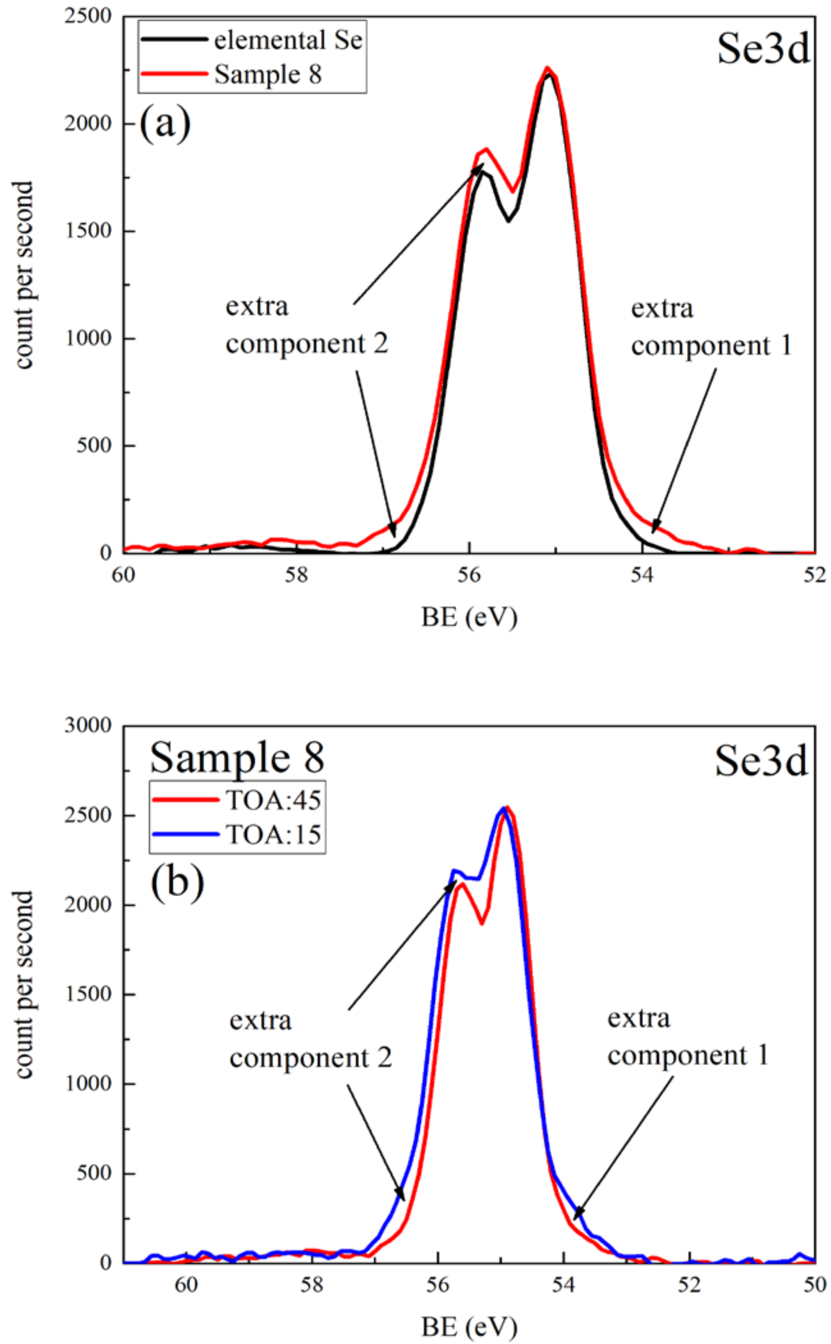

Figure 6.10 Comparison of Se3d spectra: (a) comparison between elemental Se and the sample 8; (b) comparison between the spectra collected at different TOAs.

The Se3d$_{3/2}$ peak of the sample 8 is higher. Moreover, the convoluted Se3d peak of the sample 8 displays extra components at the bottom of two leading edges. These extra components

demonstrate that the Se3d peak contains more than Se^0 component. The multiple components of the Se3d peak of the sample 8 are also confirmed by the Se3d spectrum of the sample 8 acquired at 15˚ TOA. If a XPS spectrum is collected at a low TOA, the spectrum is more surface sensitive. The two Se3d spectra of the sample 8 are compared in Figure 6.10 (b). The heights of the two spectra are normalized. The spin-orbital splitting peaks are not well separated in the Se3d spectrum at 15˚ TOA. The convoluted Se3d at 15˚ TOA also exhibits extra components at the bottom of two leading edges. Thus, we can confirm that the Se3d peak of the Se/ITO sample contains more than one component. According to the energy positions of the three components, we can assume that the three components are Se^0, Se with negative oxidation state, and Se with positive oxidation state. The Se content with negative oxidation state is at the lower binding energy side of the Se^0 component and is labeled as extra component 1 in Figure 6.10. The Se content with positive oxidation state is at the higher binding energy side of the Se^0 component and is labeled as extra component 2 in Figure 6.10.

6.3.3.2 Parallel Experiment to Investigate the Chemical Bonding of Se in Se/ITO

So far, we only know that the Se3d spectrum of the Se/ITO sample has multiple components. To figure out the exact components in the Se3d spectra, a parallel experiment is carried out. The Se ultra-thin films are deposited on Si substrates with and without native oxide via the same deposition method. The prepared samples are characterized by in-situ XPS. The Si substrate without native oxide is cleaned by Ar^+ sputtering to remove the native oxide and surface contaminant in vacuum before deposition. This substrate is denoted as Si. For the Si substrate with native oxide, the sputtering only removes carbon contaminant completely by mild Ar^+ sputtering. The level of the surface contaminant is monitored by measuring C1s core-level

XPS spectrum. This substrate is denoted as SiOx in this experiment.

In the XPS measurement, Si2p and Se3d core level spectra are collected from the Se/Si and Se/SiOx samples simultaneously. The Si2p peaks are used as energy references for energy calibration. The Se3d spectra of the Se/Si and Se/SiOx samples are displayed in Figure 6.11. For the Se3d spectra of the Se/Si samples, although the two spectra have the different line-shapes, peak shift is not happened. Comparing the Se3d spectra of the Se/Si samples with the Se3d spectrum of the Se/SiOx sample, one can observe that the Se3d spectrum of the Se/SiOx sample shifts to higher binding energy side. The Se3d spectra of the Se/Si and Se/SiOx samples partially overlaps. The non-overlapping part in the Se3d peak of Se/Si is at the lower binding energy side, while the non-overlapping part in the Se3d peak of Se/SiOx is at the higher binding energy side. The oxidation state of selenium can be -2, +2, +4, and +6. According to the position of the overlapping part, that part is the Se^0 component. For the Se/Si sample, the non-overlapping part should belong to the Se content with negative oxidation state. It means that the non-overlapping part belongs to Se^{2-}. Si is the only element in the substrate. Silicon and selenium can form Silicon Selenide. It is possible that the Silicon Selenide is form at Se/Si interface when the Se ultra-thin film is deposited on the Si substrate. The exact oxidation state of Si cannot be directly determined by the Si2p spectra. Thus, the formed Silicon Selenide can be Silicon diselenide or Silicon mono-selenide. In the Se/SiOx sample, the surface of the substrate is covered by native Silicon oxide layer. The non-overlapping part is at higher binding energy side of Se^0 component. It must correlate with the oxygen on the surface of the substrate. It is possible to form bonding between Se and oxygen ions at the Se/SiOx interface. The Se atoms cannot be strongly oxidized by SiOx. The oxidation state of selenium may be only +2.

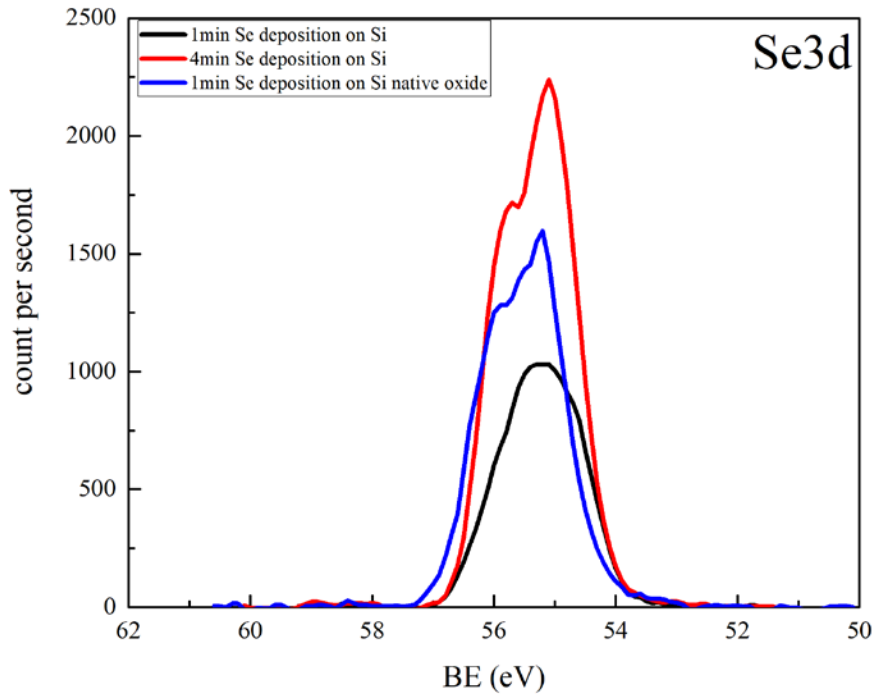

Figure 6.11 Se3d spectra of the Se/Si and Se/SiOx samples.

6.3.3.3 Peak Fitting on Se3d of Se/ITO

The Se3d spectra from Se/Si and Se/SiOx demonstrate the existence of the Se^0, Se^{2-}, and Se^{2+} components. The same components are possibly found in the Se/ITO samples. In Figure 6.10, extra components are found on both higher and lower binding energy sides. The Sn-rich surface of ITO contains Sn^{4+}, Sn^{2+}, and Sn^0 [60]. The surface provides conditions to form SeO and SnSe. It is reasonable to assume that the extra components in Figure 6.10 belong to Se^{2-} and Se^{2+}. The components of the Se3d peak is investigated by the peak fitting.

Peak fitting on Se3d of the sample 8 (TOA=45˚) is shown in Figure 6.12 (a). The spectrum is fitted by three doublets which represent Se^{2-}, Se^0, and Se^{2+}. Each doublet represents a pair of spin-orbital splitting peaks: $Se3d_{5/2}$ and $Se3d_{3/2}$. The two peaks have a constant energy

separation which is 0.84 eV and intensity ratio of $Se3d_{3/2}$ to $Se3d_{5/2}$ which is 0.76. The intensity ratio is obtained from the peak fitting on Se3d spectrum of elemental selenium.

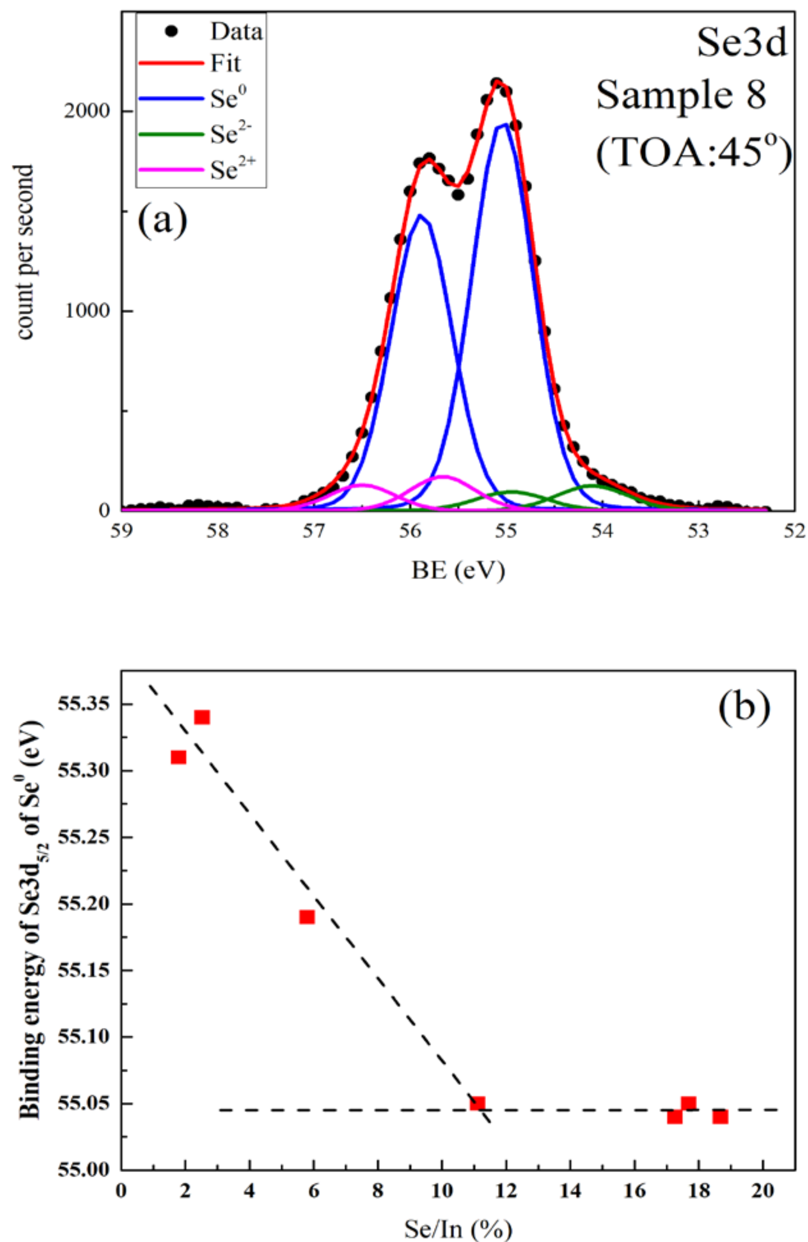

Figure 6.12 Peak fitting results of Se3d spectra of the Se/ITO samples.

The peak fitting result shows the binding energy of $Se3d_{5/2}$ for Se^0, Se^{2-}, and Se^{2+} are 55.04 eV, 54.11 eV, and 55.66 eV, respectively. The peak fitting result of Sn3d shows the metal

Sn is on the surface of ITO substrate in Chapter 4. Sn and Se can react to form SnSe according to the enthalpy of reaction [112]:

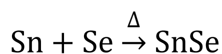

$$\mathrm{Sn} + \mathrm{Se} \xrightarrow{\Delta} \mathrm{SnSe}$$

$$\Delta H^{0}_{298} = -88.7\ \mathrm{kJ} \cdot \mathrm{mol}^{-1} \qquad \text{Equation 6.1}$$

The binding energies of $Se3d_{5/2}$ for SnSe reported in literature are 53.70 eV [113] and 55.00 eV [114]. 54.11 eV is a reasonable value for the binding energy of Se^{2-} in this experiment. The binding energy of $Se3d_{5/2}$ for SeO_2 is in the region from 58.8 to 59.9 eV in the NIST X-ray Photoelectron Spectroscopy database. In this experiment, the binding energy for the peak at higher binding energy side of Se^0 peak is only 55.66 eV. Thus, SeO_2 cannot exist in this experiment. The possible oxidation state of Se for that component is +2. In the Se/ITO interface region, selenium ions can bond with oxygen ions or share the oxygen ions with tin ions. The effective oxidation state of the Se ion can be even less than for +2. In this study, the exact positive oxidation state of Se cannot be clarified. This component is just named Se^{2+}.

In Figure 6.9, the peak shift of Se3d spectra is already mentioned. The peak fitting provides the binding energy of $Se3d_{5/2}$ peak of Se^0 in each Se spectrum. Due to the low statistics of the Se3d spectrum of the sample 1, the peak fitting is not done on that spectrum. The binding energy versus the intensity ratio of Se/In is plotted in Figure 6.10 (b). From the sample 2 to the sample 5, the plot shows the binding energy of $Se3d_{5/2}$ shifts from 55.34 eV to 55.04 eV. From the sample 5 to sample 8, the binding energy stay a constant. The season caused the peak shift is unknown yet. There are two possibilities. One is the size of the sample. The other is the band bending.

The deposited Se may not form a homogenous thin film. It may form clusters on the substrate when the amount is small. If the size of the Se clusters is only several nanometers, the

peak shift to higher binding energy side will happen on the Se3d spectrum [115][116].

The binding energy of screened $In3d_{5/2}$ peak versus the intensity ratio of Se/In is plotted in Figure 6.8 (a). The peak shift of $In3d_{5/2}$ has the same trend as that of $Se3d_{5/2}$. The binding energy of $In3d_{5/2}$ shifts to lower binding energy side with increased amount of deposited Se. Then, the peak shift stops when the amount of deposited Se reaches a certain level. We conclude that the peak shift of $In3d_{5/2}$ results from the band bending at the interface. The peak shift of Se3d spectra could also result from the band bending at the Se/ITO interface. The work function of elemental Se is 5.1 eV [106]. The band gap of elemental Se is 2.2 eV [117]. The energy difference between the Fermi edge and the valence band maximum is 0.85 to 0.98 eV. This value is obtained from the valence band XPS spectrum and the UPS spectrum. The measured work function of the ITO substrate is 4.41 eV. The measured energy distance between the valence band maximum and the Fermi edge is 3.00 eV. If drawing a band alignment diagram, one will find the valence band of elemental Se bends downward at the Se/ITO interface. The energy difference between the valence band maximum of Se and ITO is 2.02 to 2.15 eV. The direction of the binding energy shift of Se3d is coherent with the band bending direction. However, the magnitude of the peak shifting distance is much smaller than energy difference between the two valence bands. It may be attributed to the complicated chemical bonding at the Se/ITO interface. At the interface, Se, Sn, and O form components which may have influence on the band bend at Se/ITO interface. The formed components may provide new electron states to decrease the magnitude of the peak shift. In this study, the origin of the binding energy shift on Se3d spectra cannot be simply concluded. More experiment is needed to figure out the mechanism.

6.4 Conclusion

Selenium is deposited on ITO substrates. The work function increases with increased thickness of Se film until it reaches 5.05 ± 0.06 eV. The XPS analysis reveals the chemical binding among Se, Sn, and Oxygen. Se bonds with oxygen to reduce Sn^{4+} to Sn^{2+}. Se also bonds with Sn to form Se-Sn binding. However, this reactivity doesn't extend beyond few Se monolayers at the interface. At beginning of Se deposition, the reaction keeps happening with increased amount of deposited Se. This reaction will be saturated soon. Then the further deposited Se is in form of Se^0. Se seems to be chemical stable on ITO surface.

CHAPTER 7

CONCLUSION OF DISSERTATION

In this dissertation, the first study focused on investigating the Ar^+ sputtering induced surface chemistry change of ITO samples. The correlation between the evolution of surface chemistry of Sn-rich surface of ITO and work function is determined. The second study focused on the evaluation of enhancing the work function of ITO via RuO_2 and Se nanoscale thin film coatings. The interplay between deposited films thicknesses, their reactivity with Sn-rich ITO surface and work function are elucidated.

The Sn-rich surface of ITO is confirmed by AR-XPS. A combination of UV-ozone radiation and Ar^+ sputtering removes most of surface carbon-based contaminants as well as a part of segregated Sn content on the surface of ITO. The XPS and UPS measurements showed that the Ar^+ sputtering leads to thinning of the Sn at the Sn-rich ITO surface and reduction of Sn oxidation state that are both detrimental to the work function of ITO. The Sn^{4+} ion is reduced to Sn^{2+} in the Sn-rich ITO surface. This is the result of oxygen preferential sputtering. The preferential sputtering is more prominent for oxygen followed by Sn. The indium in ITO doesn't seem to be affected in any significant way. The highest effective work function of UV-ozone treated (cleaned) ITO was measured to be 4.41 eV. When Exposed further to Ar^+ sputtering, the work function shows a decrease as a function of sputtering time. Comprehensive XPS and UPS data analysis demonstrated for the first time that the decrease of the work function of the Ar^+ irradiated ITO is the result of decreased amount of Sn in the Sn-rich surface of ITO relative to indium as well as the reduction of Sn^{4+} to Sn^{2+} due to oxygen preferential sputtering. To assure the highest work function of ITO, in addition to the well-known removal of hydrocarbon based contaminants, one would have to find a better surface cleaning method that would keep the

surface of ITO rich in Sn with and oxidation state of Sn^{4+}. The work function of ITO is successfully enhanced by RuO_2 and Se nanoscale thin film coating.

In the second studies, it was demonstrated that both the RuO_2 and se nanoscale thin film coatings enhanced the work function of ITO from 4.41 eV to 4.98 eV and 5.05 eV respectively.

The interplay between RuO_2 coverage, its stability/reactivity with the Sn-rich surface of ITO and its work function is investigated by XPS and UPS. XPS data showed that the RuO_2 deposition reduces the oxidation state of Sn from +4 to +2 in Sn-rich ITO surface. The deposited RuO_2 and the Sn-rich surface forms a Ru-Sn-O ternary oxide system on the surface of ITO.

For the Se coverage studies, UPS showed a work function of Se/ITO as high as 5.05 eV for an optimal Se coverage. That's a significant increase from the 4.41 eV of the UV-ozone only treated ITO and is good enough for optimal device applications. The increase plateaus when the work function of Se/ITO reaches 5.05 eV. XPS shows that Se reacts with the Sn-rich surface of ITO at Se/ITO interface: Se presents both positive and negative oxidation states, and Se also reduces the oxidation state of Sn from +4 to +2. However, this reactivity doesn't extend beyond few Se monolayers at the interface. Se seems to be chemical stable on ITO surface.

A combination of RuO_2/Se nanoscale coating of optimally cleaned ITO would be a good alternative for device applications that would provide work function tuning in addition to their potential ability to act as interface stabilizers and a barrier to reaction and inter-diffusion at ITO/active layers interfaces responsible for long term stability of devices and especially organic solar cells and organic light emitting diodes.

REFERENCES

[1] G. G. Untila, T. N. Kost, a. B. Chebotareva, and M. a. Timofeyev, "Effect of the tin content on the composition and optical and electrical properties of ITO films deposited onto silicon and glass by ultrasonic spray pyrolysis," *Semiconductors*, vol. 46, no. 7, pp. 962–968, Jul. 2012.

[2] G. Frank and H. Kostlin, "Electrical properties and defect model of tin-doped indium oxide layers," *Appl. Phys. A Solids Surfaces*, vol. 27, no. 4, pp. 197–206, Apr. 1982.

[3] M. V. Hohmann, A. Wachau, and A. Klein, "In situ Hall effect and conductivity measurements of ITO thin films," *Solid State Ionics*, vol. 262, pp. 636–639, 2014.

[4] G. Zhu, L. Zhi, H. Yang, H. Xu, and A. Yu, "Effect of Target Density on Microstructural, Electrical, and Optical Properties of Indium Tin Oxide Thin Films," *J. Electron. Mater.*, vol. 41, no. 9, pp. 2376–2379, Jun. 2012.

[5] L. N. Bai, Y. P. Wei, J. S. Lian, and Q. Jiang, "Stability of indium–tin-oxide and its optical properties: A first-principles study," *J. Phys. Chem. Solids*, vol. 74, no. 3, pp. 446–451, Mar. 2013.

[6] S. So, W. Choi, and C. Cheng, "Surface preparation and characterization of indium tin oxide substrates for organic electroluminescent devices," *Appl. Phys. A …*, vol. 450, pp. 447–450, 1999.

[7] I. Hamberg and C. G. Granqvist, "Evaporated Sn-doped In2O3 films: Basic optical properties and applications to energy-efficient windows," *J. Appl. Phys.*, vol. 60, no. 11, p. R123, 1986.

[8] R. F. Minibaev, a. a. Bagatur'yants, D. I. Bazhanov, a. a. Knizhnik, and M. V. Alfimov, "First-principles investigation of the electron work function for the (001) surface of indium oxide In2O3 and indium tin oxide (ITO) as a function of the surface oxidation level," *Nanotechnologies Russ.*, vol. 5, no. 3–4, pp. 185–190, May 2010.

[9] J. H. W. De Wit, G. Van Unen, and M. Lahey, "Electron concentration and mobility in In2O3," *J. Phys. Chem. Solids*, vol. 38, no. 8, pp. 819–824, 1977.

[10] P. Parent, H. Dexpert, and G. Tourillon, "Structural Study of Tin-Doped Indium Oxide Thin Films Using X-Ray Absorption Spectroscopy and X-Ray Diffraction," vol. 139, no. 1, pp. 276–281, 1992.

[11] M. N. Tripathi, K. Shida, R. Sahara, H. Mizuseki, and Y. Kawazoe, "First-principles analysis of structural and opto-electronic properties of indium tin oxide," *J. Appl. Phys.*, vol. 111, no. 10, p. 103110, 2012.

[12] N. Nadaud, N. Lequeux, and M. Nanot, "Structural Studies of Tin-Doped Indium Oxide (ITO) and In 4 Sn 3 O 12," *J. Solid State Chem.*, vol. 148, no. 135, pp. 140–148, 1998.

[13] G. B. González, T. O. Mason, J. P. Quintana, O. Warschkow, D. E. Ellis, J. H. Hwang, J. P. Hodges, and J. D. Jorgensen, “Defect structure studies of bulk and nano-indium-tin oxide,” *J. Appl. Phys.*, vol. 96, no. 7, pp. 3912–3920, 2004.

[14] N. Yamada, Y. Shigesato, I. Yasui, H. Li, Y. Ujihira, and K. Nomura, “Estimation of Chemical States and Carrier Density of Sn-doped In2O3 (ITO) by M{ö}ssbauer Spectrometry,” *Hyperfine Interact.*, vol. 112, no. 1, pp. 213–216, 1998.

[15] N. Yamada, I. Yasui, Y. Shigesato, H. Li, Y. Ujihira, and K. Nomura, “Doping Mechanisms of Sn in In 2 O 3 Powder Studied Using 119 Sn Mössbauer Spectroscopy and X-Ray Diffraction,” *Jpn. J. Appl. Phys.*, vol. 38, no. Part 1, No. 5A, pp. 2856–2862, May 1999.

[16] H. Köstlin, R. Jost, and W. Lems, “Optical and electrical properties of doped In2O3 films,” *Phys. Status Solidi*, vol. 29, no. 1, pp. 87–93, May 1975.

[17] O. Warschkow, D. E. Ellis, G. B. Gonzalez, and T. O. Mason, “Defect cluster aggregation and nonreducibility in tin-doped indium oxide,” *J. Am. Ceram. Soc.*, vol. 86, pp. 1707–1711, 2003.

[18] H. Enoki and J. E. und H. Suto, “The Intermediate Compound in the {In_2O_3--SnO_2} System,” *J. Mater. Sci.*, vol. 26, no. 29, pp. 4110–4115, 1991.

[19] G. Falk, “Sintering of Transparent Conductive Oxides: From Oxide Ceramic Powders to Advanced Optoelectronic Materials,” *Sinter. Ceram. - New Emerg. Tech.*, pp. 587–610, 2009.

[20] G. Frank, H. Köstlin, and A. Rabenau, “X-ray and optical measurements in the In2O3□SnO2 system,” *Phys. Status Solidi*, vol. 52, no. 1, pp. 231–238, Mar. 1979.

[21] J. C. C. Fan and J. B. Goodenough, “X-ray photoemission spectroscopy studies of Sn-doped indium-oxide films,” *J. Appl. Phys.*, vol. 48, no. 8, p. 3524, 1977.

[22] W. Song, S. K. So, and L. Cao, “Angular-dependent photoemission studies of indium tin oxide surfaces,” *Appl. Phys. A Mater. Sci. Process.*, vol. 72, no. 3, pp. 361–365, Mar. 2001.

[23] C. C. Wu, C. I. Wu, J. C. Sturm, and A. Kahn, “Surface modification of indium tin oxide by plasma treatment: An effective method to improve the efficiency, brightness, and reliability of organic light emitting devices,” *Appl. Phys. Lett.*, vol. 70, no. March, p. 1348, 1997.

[24] J. Kim, P. Ho, and D. Thomas, “X-ray photoelectron spectroscopy of surface-treated indium-tin oxide thin films,” *Chem. Phys. …*, 1999.

[25] Y. Park, V. Choong, Y. Gao, B. R. Hsieh, and C. W. Tang, “Work function of indium tin oxide transparent conductor measured by photoelectron spectroscopy,” *Appl. Phys. Lett.*, vol. 68, no. 19, p. 2699, 1996.

[26] R. G. Gordon, “Criteria for Choosing Transparent Conductors,” *MRS Bull.*, vol. 25, no. 8, pp. 52–57, 2000.

[27] A. Klein, C. Körber, A. Wachau, F. Säuberlich, Y. Gassenbauer, S. P. Harvey, D. E. Proffit, and T. O. Mason, “Transparent Conducting Oxides for Photovoltaics: Manipulation of Fermi Level, Work Function and Energy Band Alignment,” *Materials (Basel).*, vol. 3, no. 11, pp. 4892–4914, Nov. 2010.

[28] J. a Chaney, S. E. Koh, C. S. Dulcey, and P. E. Pehrsson, “Surface chemistry of carbon removal from indium tin oxide by base and plasma treatment, with implications on hydroxyl termination,” *Appl. Surf. Sci.*, vol. 218, no. 1–4, pp. 259–267, Sep. 2003.

[29] R. Schlaf, H. Murata, and Z. . Kafafi, “Work function measurements on indium tin oxide films,” *J. Electron Spectros. Relat. Phenomena*, vol. 120, no. 1–3, pp. 149–154, Oct. 2001.

[30] K. Sugiyama, H. Ishii, Y. Ouchi, and K. Seki, “Dependence of indium–tin–oxide work function on surface cleaning method as studied by ultraviolet and x-ray photoemission spectroscopies,” *J. Appl. Phys.*, vol. 87, no. 1, p. 295, 2000.

[31] V. M. Bermudez, A. D. Berry, H. Kim, and A. Piqué, “Functionalization of indium tin oxide.,” *Langmuir*, vol. 22, no. 26, pp. 11113–25, Dec. 2006.

[32] J. a Chaney and P. E. Pehrsson, “Work function changes and surface chemistry of oxygen, hydrogen, and carbon on indium tin oxide,” *Appl. Surf. Sci.*, vol. 180, no. 3–4, pp. 214–226, Aug. 2001.

[33] H. Y. Yu, X. D. Feng, D. Grozea, Z. H. Lu, R. N. S. Sodhi, a-M. Hor, and H. Aziz, “Surface electronic structure of plasma-treated indium tin oxides,” *Appl. Phys. Lett.*, vol. 78, no. 17, p. 2595, 2001.

[34] J.-K. Kim, “Cleaning and Functionalization of Polymer Surfaces and Nanoscale Carbon Fillers by UV/Ozone Treatment: A Review,” *J. Compos. Mater.*, vol. 43, no. 14, pp. 1537–1564, Jun. 2009.

[35] S. Y. Kim, “Effect of ultraviolet–ozone treatment of indium–tin–oxide on electrical properties of organic light emitting diodes,” *J. Appl. Phys.*, vol. 95, no. 5, p. 2560, 2004.

[36] L. F. MacManus, M. J. Walzak, and N. S. McIntyre, “Study of ultraviolet light and ozone surface modification of polypropylene,” *J. Polym. Sci. Part A Polym. Chem.*, vol. 37, no. 14, pp. 2489–2501, Jul. 1999.

[37] B.-S. Kim, D.-E. Kim, Y.-K. Jang, N.-S. Lee, O.-K. Kwon, and Y.-S. Kwon, “UV-Ozone Surface Treatment of Indium-Tin-Oxide in Organic Light Emitting Diodes,” *J. Korean Phys. Soc.*, vol. 50, no. 6, p. 1858, Jun. 2007.

[38] R. a Baragiola, “Sputtering: survey of observations and derived principles.,” *Philos. Trans. A. Math. Phys. Eng. Sci.*, vol. 362, no. 1814, pp. 29–53, 2004.

[39] V. I. Zaporozchenko and M. G. Stepanovat, "Preferential Sputtering in Binary Targets.pdf," vol. 49, no. 2, pp. 155–196, 1995.

[40] P. . Kelly and R. . Arnell, "Magnetron sputtering: a review of recent developments and applications," *Vacuum*, vol. 56, no. 3, pp. 159–172, Mar. 2000.

[41] K. Sarakinos, J. Alami, and S. Konstantinidis, "High power pulsed magnetron sputtering: A review on scientific and engineering state of the art," *Surf. Coatings Technol.*, vol. 204, no. 11, pp. 1661–1684, Feb. 2010.

[42] G. Bräuer, B. Szyszka, M. Vergöhl, and R. Bandorf, "Magnetron sputtering – Milestones of 30 years," *Vacuum*, vol. 84, no. 12, pp. 1354–1359, Jun. 2010.

[43] D. Briggs and J. T. Grant, *Surface Analysis by Auger and X-Ray Photoelectron Spectroscopy*. SurfaceSpectra, 2003.

[44] G. Ertl and J. Küppers, *Low Energy Electrons and Surface Chemistry*. VCH Verlag Ges., 1985.

[45] E. Centurioni and D. Iencinella, "Role of front contact work function on amorphous silicon/crystalline silicon heterojunction solar cell performance," *IEEE Electron Device Lett.*, vol. 24, no. 3, pp. 177–179, Mar. 2003.

[46] I. Irfan, S. Graber, F. So, and Y. Gao, "Interplay of cleaning and de-doping in oxygen plasma treated high work function indium tin oxide (ITO)," *Org. Electron.*, vol. 13, no. 10, pp. 2028–2034, Oct. 2012.

[47] K. L. Purvis, G. Lu, J. Schwartz, and S. L. Bernasek, "Surface Characterization and Modification of Indium Tin Oxide in Ultrahigh Vacuum," *J. Am. Chem. Soc.*, vol. 122, no. 8, pp. 1808–1809, 2000.

[48] J. C. C. Fan and J. B. Goodenough, "X-ray photoemission spectroscopy studies of Sn-doped indium-oxide films," *J. Appl. Phys.*, vol. 48, no. 8, p. 3524, 1977.

[49] Y. Shigesato, S. Takaki, and T. Haranou, "Crystallinity and electrical properties of tin-doped indium oxide films deposited by DC magnetron sputtering," *Appl. Surf. Sci.*, vol. 49, pp. 269–275, 1991.

[50] C. Körber, V. Krishnakumar, a. Klein, G. Panaccione, P. Torelli, a. Walsh, J. L. F. Da Silva, S.-H. Wei, R. G. Egdell, and D. J. Payne, "Electronic structure of In_{2}O_{3} and Sn-doped In_{2}O_{3} by hard x-ray photoemission spectroscopy," *Phys. Rev. B*, vol. 81, no. 16, p. 165207, Apr. 2010.

[51] P. S. Bagus, E. S. Ilton, and C. J. Nelin, "The interpretation of XPS spectra: Insights into materials properties," *Surf. Sci. Rep.*, vol. 68, no. 2, pp. 273–304, 2013.

[52] A. Kotani and Y. Toyozawa, "Photoelectron spectra of core electrons in metals with an incomplete shell," *J. Phys. Soc. Japan*, vol. 37, no. 4, 1974.

[53] M. Campagna, G. Wertheim, and H. Shanks, "Local Character of Many-Body Effects in X-Ray Photoemission from Transition-Metal Compounds: Na x WO 3," *Phys. Rev. Lett.*, vol. 34, no. 12, 1975.

[54] J. Chazalviel and M. Campagna, "Final-state effects in the x-ray photoelectron spectra of cubic sodium-tungsten bronzes," *Phys. Rev. B*, vol. 16, no. 2, 1977.

[55] G. Wertheim, "WHAT DOES CORE-ELECTRON SPECTROSCOPY TELL US ABOUT THE INITIAL STATE OF NaxW03 ?," *Chem. Phys. Lett.*, vol. 65, no. 2, pp. 377–379, 1979.

[56] R. G. Egdell, T. J. Walker, and G. Beamson, "The screening response of a dilute electron gas in core level photoemission from Sb-doped SnO2," *J. Electron Spectros. Relat. Phenomena*, vol. 128, no. 1, pp. 59–66, 2003.

[57] D. C. Langreth, "Theory of Plasmon Effects in High Energy Spectroscopy," *Nobel Symp.*, vol. 24, no. 2, pp. 210–222, 1973.

[58] M. Batzill and U. Diebold, "The surface and materials science of tin oxide," *Prog. Surf. Sci.*, vol. 79, no. 2–4, pp. 47–154, 2005.

[59] I. Manassidis, J. Goniakowski, L. N. Kantorovich, and M. J. Gillan, "The structure of the stoichiometric and reduced SnO2 (110) surface," *Surf. Sci.*, vol. 339, pp. 258–271, 1995.

[60] D. F. Cox, T. B. Fryberger, and S. Semancik, "Oxygen vacancies and defect electronic states on the SnO2 (110)-1X1 surface," *Phys. Rev. B*, vol. 38, no. 3, 1988.

[61] D. F. Cox, T. B. Fryberger, and S. Semancik, "SURFACE RECONSTRUCTION OF OXYGEN DEFICIENT SnO2(110)," vol. 224, pp. 121–142, 1989.

[62] Y. Gassenbauer, R. Schafranek, A. Klein, and S. Zafeiratos, "Surface states, surface potentials, and segregation at surfaces of tin-doped In 2 O 3," pp. 1–11, 2006.

[63] K. Rachut, C. Körber, J. Brötz, and A. Klein, "Growth and surface properties of epitaxial SnO 2," *Phys. Status Solidi*, vol. 8, no. 9, p. n/a-n/a, 2014.

[64] G. Gaggiotti, A. Galdikas, S. Kačiulis, G. Mattogno, and A. Šetkus, "Surface chemistry of tin oxide based gas sensors," *J. Appl. Phys.*, vol. 76, no. 8, p. 4467, 1994.

[65] J. F. Moulder, W. F. Stickle, P. E. Sobol, and K. D. Bomben, "Handbook of X-ray Photoelectron Spectroscopy," p. 261, 1992.

[66] M. Fondell, M. Gorgoi, M. Boman, and a. Lindblad, "An HAXPES study of Sn, SnS, SnO and SnO2," *J. Electron Spectros. Relat. Phenomena*, vol. 195, pp. 195–199, 2014.

[67] M. Brumbach, P. A. Veneman, F. S. Matrikar, T. Schulmeyer, A. Simmonds, W. Xia, P. Lee, and N. R. Armstrong, "Surface composition and electrical and electrochemical

properties of freshly deposited and acid-etched indium tin oxide electrodes," *Langmuir*, vol. 23, no. 22, pp. 11089–11099, 2007.

[68] A. W. C. Lin, N. R. Armstrong, and T. Kuwana, "X-ray photoelectron/Auger electron spectroscopic studies of tin and indium metal foils and oxides," *Anal. Chem.*, vol. 49, pp. 1228–1235, 1977.

[69] M. M. Beerbom, B. Lägel, a. J. Cascio, B. V. Doran, and R. Schlaf, "Direct comparison of photoemission spectroscopy and in situ Kelvin probe work function measurements on indium tin oxide films," *J. Electron Spectros. Relat. Phenomena*, vol. 152, no. 1–2, pp. 12–17, Jun. 2006.

[70] C. Kim, B. Lee, H. J. Yang, H. M. Lee, J. G. Lee, and H. Shin, "Effects of Surface Treatment on Work Function of ITO (Indium Tin Oxide) Films," vol. 47, no. November, pp. 417–421, 2005.

[71] O. M. Løvvik, S. Diplas, a. Romanyuk, and a. Ulyashin, "Initial stages of ITO/Si interface formation: In situ x-ray photoelectron spectroscopy measurements upon magnetron sputtering and atomistic modelling using density functional theory," *J. Appl. Phys.*, vol. 115, no. 8, p. 83705, 2014.

[72] M. Steiner, S. P. Philipps, M. Hermle, A. W. Bett, and F. Dimroth, "Validated front contact grid simulation for GaAs solar cells under concentrated sunlight," *Prog. Photovoltaics Res. Appl.*, vol. 19, no. 1, pp. 73–83, Jan. 2011.

[73] I. Hancox, P. Sullivan, K. V. Chauhan, N. Beaumont, L. A. Rochford, R. A. Hatton, and T. S. Jones, "The effect of a MoOx hole-extracting layer on the performance of organic photovoltaic cells based on small molecule planar heterojunctions," *Org. Electron.*, vol. 11, no. 12, pp. 2019–2025, 2010.

[74] J. C. Scott, J. H. Kaufman, P. J. Brock, R. DiPietro, J. Salem, and J. A. Goitia, "Degradation and failure of MEH-PPV light-emitting diodes," *J. Appl. Phys.*, vol. 79, no. 5, p. 2745, 1996.

[75] Y. Li, C. Liu, S. Tong, L. Pan, L. Pu, T. Minari, K. Tsukagoshi, and Y. Shi, "Metal-diffusion-induced ITO nanoparticles at the organic/ITO interface," *J. Phys. D. Appl. Phys.*, vol. 45, no. 16, p. 165104, Apr. 2012.

[76] K. M. Glassford and J. R. Chelikowsky, "Electronic and structural properties of RuO 2," *Phys. Rev. B*, vol. 47, no. 4, pp. 1732–1741, Jan. 1993.

[77] Y. K. Vayunandana Reddy and D. Mergel, "Structural and electrical properties of RuO2 thin films prepared by rf-magnetron sputtering and annealing at different temperatures," *J. Mater. Sci. Mater. Electron.*, vol. 17, no. 12, pp. 1029–1034, 2006.

[78] W. D. Ryden, A. W. Lawson, and C. C. Sartain, "Electrical Transport Properties of Ir O 2 and Ru O 2," *Phys. Rev. B*, vol. 1, no. 4, pp. 1494–1500, Feb. 1970.

[79] D.-J. Yun, H. Ra, S. B. Jo, W. Maeng, S. Lee, S. Park, J.-W. Jang, K. Cho, and S.-W. Rhee, "Effects of postannealing process on the properties of RuO2 films and their performance as electrodes in organic thin film transistors or solar cells.," *ACS Appl. Mater. Interfaces*, vol. 4, no. 9, pp. 4588–94, Sep. 2012.

[80] D.-J. Yun, S. Lee, K. Yong, and S.-W. Rhee, "In situ ultraviolet photoemission spectroscopy measurement of the pentacene-RuO[sub 2]/Ti contact energy structure," *Appl. Phys. Lett.*, vol. 97, no. 7, p. 73303, 2010.

[81] Y. T. Kim, W. Lee, and S. K. Kwak, "Comparison of high temperature thermal stabilities of Ru and RuO 2 Schottky contacts to GaAs," *Appl. Phys. Lett.*, vol. 67, no. August 1995, pp. 807–810, 1995.

[82] K. Sakiyama, S. Onishi, K. Ishihara, K. Orita, T. Kajiyama, N. Hosoda, and T. Hara, "Deposition and properties of reactively sputtered ruthenium dioxide films," *J. Electrochem. Soc.*, vol. 140, no. 3, pp. 834–839, 1993.

[83] E. Kolawa, F. C. T. So, W. Flick, X.-A. Zhao, E. .-S. Pan, and M.-A. Nicolet, "Reactive sputtering of RuO2 films," *Thin Solid Films*, vol. 173, no. 2, pp. 217–224, Jun. 1989.

[84] L. Krusin-Elbaum, M. Wittmer, and D. S. Yee, "Characterization of reactively sputtered ruthenium dioxide for very large scale integrated metallization," *Appl. Phys. Lett.*, vol. 50, no. 26, pp. 1879–1881, 1987.

[85] C. W. Nieh, E. Kolawa, F. C. T. So, and M.-A. Nicolet, "Microstructure of RuO2 layer as diffusion barrier between Al and Si substrate," *Mater. Lett.*, vol. 6, no. 5–6, pp. 177–180, Mar. 1988.

[86] P. C. Liao, S. Y. Mar, W. S. Ho, Y. S. Huang, and K. K. Tiong, "Characterization of RuO2 thin films deposited on Si by metal-organic chemical vapor deposition," *Thin Solid Films*, vol. 287, no. 1–2, pp. 74–79, 1996.

[87] M. L. Green, M. E. Gross, L. E. Papa, K. J. Schnoes, and D. Brasen, "Chemical Vapor Deposition of Ruthenium and Ruthenium Dioxide Films," *J. Electrochem. Soc.*, vol. 132, no. 11, pp. 2677–2685, 1985.

[88] J. R. and C. T.-N. and J. J. P. and R. C. and J. J. V. and Y. Gobillon, "Electronic Structure of Rutile Oxides TiO 2 , RuO 2 and IrO 2 Studied by X-ray Photoelectron Spectroscopy," *Phys. Scr.*, vol. 16, no. 5–6, p. 351, 1977.

[89] K. Qadir, S. H. Joo, B. S. Mun, D. R. Butcher, J. R. Renzas, F. Aksoy, Z. Liu, G. a Somorjai, and J. Y. Park, "Intrinsic relation between catalytic activity of CO oxidation on Ru nanoparticles and Ru oxides uncovered with ambient pressure XPS.," *Nano Lett.*, vol. 12, no. 11, pp. 5761–8, Nov. 2012.

[90] M. A. Ernst and W. G. Sloof, "Unraveling the oxidation of Ru using XPS," *Surf. Interface Anal.*, vol. 40, no. 3–4, pp. 334–337, Mar. 2008.

[91] X. Wang, F. Deng, Z. Tang, B. Wu, D. Tang, and W. Lin, “The nature of phase separation in a Ru–Sn–O ternary oxide electrocatalyst,” *Phys. Chem. Chem. Phys.*, vol. 15, no. 11, p. 3977, 2013.

[92] J. Y. Lim, G. Rahman, S. Y. Chae, K.-Y. Lee, C.-S. Kim, and O.-S. Joo, “Highly stable RuO 2 /SnO 2 nanocomposites as anode electrocatalysts in a PEM water electrolysis cell,” *Int. J. Energy Res.*, vol. 38, no. 7, pp. 875–883, Jun. 2014.

[93] B. Dawoud, E. Amer, and D. Gross, “Experimental investigation of an adsorptive thermal energy storage,” *Int. J. energy Res.*, vol. 31, no. August 2007, pp. 135–147, 2007.

[94] Y. J. Kim, Y. Gao, and S. a. Chambers, “Core-level X-ray photoelectron spectra and X-ray photoelectron diffraction of RuO2(110) grown by molecular beam epitaxy on TiO2(110),” *Appl. Surf. Sci.*, vol. 120, pp. 250–260, 1997.

[95] F. H. ATANASOSKA, L., O’GRADY, W. E., ATANASOSKI, R. T., & POLLAK, “THE SURFACE STRUCTURE OF RuO,: A LEED, AUGER AND XI’S STUDY OF THE (110) AND (100) FACES * Lj. ATANASOSKA,” *Surf. Sci.*, vol. 202, pp. 142–166, 1988.

[96] S. Bhaskar, P. S. Dobal, S. B. Majumder, and R. S. Katiyar, “X-ray photoelectron spectroscopy and micro-Raman analysis of conductive RuO[sub 2] thin films,” *J. Appl. Phys.*, vol. 89, no. 5, p. 2987, 2001.

[97] W. E. O’Grady, L. Atanasoka, F. H. Pollak, and H. L. Park, “SINGLE CRYSTAL RuO2 (110): SURFACE STRUCTURE,” *J. Electroanal. Chem*, vol. 178, pp. 61–68, 1984.

[98] K. Reuter and M. Scheffler, “Surface core-level shifts at an oxygen-rich Ru surface: O/Ru(0001) vs. RuO2(110),” *Surf. Sci.*, vol. 490, no. 1–2, pp. 20–28, 2001.

[99] H. Over, A. P. Seitsonen, E. Lundgren, M. Smedh, and J. N. Andersen, “On the origin of the Ru-3d5/2 satellite feature from RuO2(110),” *Surf. Sci.*, vol. 504, pp. L196–L200, Apr. 2002.

[100] H. Over, a P. Seitsonen, E. Lundgren, M. Wiklund, and J. N. Andersen, “Spectroscopic characterization of catalytically active surface sites of a metallic oxide,” *Chem. Phys. Lett.*, vol. 342, no. July, pp. 467–472, 2001.

[101] H. Madhavaram, “Oxidation Reactions over RuO2: A Comparative Study of the Reactivity of the (110) Single Crystal and Polycrystalline Surfaces,” *J. Catal.*, vol. 202, no. 2, pp. 296–307, 2001.

[102] V. Christou, M. Etchells, O. Renault, P. J. Dobson, O. V. Salata, G. Beamson, and R. G. Egdell, “High resolution x-ray photoemission study of plasma oxidation of indium–tin–oxide thin film surfaces,” *J. Appl. Phys.*, vol. 88, no. 9, p. 5180, 2000.

[103] R. Bouwman and W. M. H. Sachtler, “Photoelectric determination of the work function of Ru-films as a function of sintering temperature (78°K–925°K),” vol. 24, 1971.

[104] D.-C. Nguyen, S. Tanaka, H. Nishino, K. Manabe, and S. Ito, “3-D solar cells by electrochemical-deposited Se layer as extremely-thin absorber and hole conducting layer on nanocrystalline TiO2 electrode.,” *Nanoscale Res. Lett.*, vol. 8, no. 1, p. 8, 2013.

[105] R. S. Abed, H. S. Sabaa, and M. A. Muhsien, “Effect of deposition angle on optical properties of Selenium thin films,” vol. 2, no. 5, pp. 189–192, 2013.

[106] P. Mukherjee, S. Konar, and B. C. Gupta, “Structural and electrical properties of selenium nanotubes,” *Phys. Lett. A*, vol. 380, no. 1–2, pp. 238–241, 2016.

[107] N. G. Patel, B. H. Lashkari, C. J. Panchal, and K. K. Makhija, “Improvement of efficiency of ITO/Se thin film solar cells using tellurium stimulator,” *Cryst. Res. Technol.*, vol. 29, no. 6, pp. 859–864, 1994.

[108] H. Search, C. Journals, A. Contact, M. Iopscience, and I. P. Address, “Efficient ITO / Se Heterojunction Solar Cells,” vol. 587.

[109] T. Nakada and A. Kunioka, “Electrical characteristics in indium thin oxide (ITO)/selenium heterojunction,” *Electron. Commun. Japan (Part II Electron.*, vol. 68, no. 3, pp. 12–18, Mar. 1985.

[110] A. Kunioka and T. Nakada, “High-Efficiency Selenium Photovoltaic Solar Cells,” *Jpn. J. Appl. Phys.*, vol. 21, no. S2, p. 73, Jan. 1982.

[111] N. J. Shevchick, J. Tejeda, M. Cardona, and D. W. Langer, “Valence band density of states of amorphous and trigonal selenium determined by X-ray and U.V. photoemission,” *Solid State Commun.*, vol. 12, no. 12, pp. 1285–1288, 1973.

[112] M. ACHIMOVICOVA, A. RECNIK, N. DANEU, K. L. DA SILVA, and J. HARVANOVA, “Study of Tin Selenide Mechanochemical Synthesis,” in *11th International Multidisciplinary Scientific GeoConference SGEM2011*, 2011, vol. 2, no. 1, pp. 745–752.

[113] U. Weser, G. Sokolowski, and W. Pilz, “Reaction of selenite with biochemically active thiols: An X-ray photoelectron spectroscopic study,” *J. Electron Spectros. Relat. Phenomena*, vol. 10, no. 4, pp. 429–439, 1977.

[114] R. B. Shalvoy, G. B. Fisher, and P. J. Stiles, “Bond ionicity and structural stability of some average-valence-five materials studied by x-ray photoemission,” *Phys. Rev. B*, vol. 15, no. 4, pp. 1680–1697, Feb. 1977.

[115] S. Bera, S. Dhara, S. Velmurugan, and a. K. Tyagi, “Analysis on Binding Energy and Auger Parameter for Estimating Size and Stoichiometry of ZnO Nanorods,” *Int. J. Spectrosc.*, vol. 2012, pp. 1–4, 2012.

[116] S. Peters, S. Peredkov, M. Neeb, W. Eberhardt, and M. Al-Hada, “Size-dependent XPS spectra of small supported Au-clusters,” *Surf. Sci.*, vol. 608, pp. 129–134, 2013.

[117] S. Y. and A. S. Tran Tri Nang, Masahiro Okuda, Tatsuhiko Matsushita, “Photovoltaic Effect of GexSe1-x–Se–SnO2 Heterostructure,” *Jpn. J. Appl. Phys.*, vol. 15, 1976.